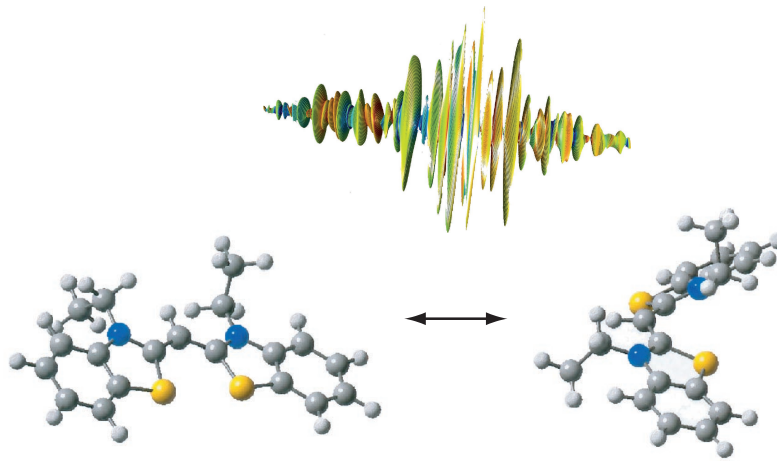


Femtosecond Quantum Control and Adaptive Polarization Pulse Shaping



Dissertation zur Erlangung des
naturwissenschaftlichen Doktorgrades
der Bayerischen Julius-Maximilians-Universität
Würzburg

vorgelegt von
Gerhard Krampert
aus Erlangen

Würzburg 2004

Eingereicht am: 16. August 2004
bei der Fakultät für Physik und Astronomie

1. Gutachter: Prof. Dr. G. Gerber
2. Gutachter: Prof. Dr. C. Spielmann
der Dissertation

1. Prüfer: Prof. Dr. G. Gerber
2. Prüfer: Prof. Dr. C. Spielmann
3. Prüfer: Prof. Dr. G. Reents
im Promotionskolloquium

Tag des Promotionskolloquium: 9. September 2004

List of Publications

Parts of this work have been published in the following references:

N.H. Damrauer, C. Dietl, G. Krampert, S.H. Lee, K.H. Jung, and G. Gerber,
Control of bond-selective photochemistry in CH₂BrCl using adaptive femtosecond pulse shaping,
Eur. Phys. J. D **20**, 71–76 (2002).

T. Brixner, G. Krampert, P. Niklaus, and G. Gerber,
Generation and characterization of polarization-shaped femtosecond laser pulses,
Appl. Phys. B **74** [Suppl.], S133–S144 (2002).

T. Brixner, N. H. Damrauer, G. Krampert, P. Niklaus, and G. Gerber,
Adaptive femtosecond quantum control in the liquid phase,
In D. R. Miller, M. M. Murnane, N. F. Scherer and A. M. Weiner (Eds.), *Ultra-fast Phenomena XIII*,
Volume 71 of *Springer Series in Chemical Physics*, pp.481–483, Springer, Berlin (2001).

T. Brixner, N.H. Damrauer, G. Krampert, P. Niklaus, and G. Gerber,
Femtosecond learning control of quantum dynamics in gases and liquids: technology and applications,
J. Mod. Optic **50**, 539–560 (2003).

T. Brixner, N. H. Damrauer, G. Krampert, P. Niklaus, and G. Gerber,
Adaptive shaping of femtosecond polarization profiles,
J. Opt. Soc. Am. B **20**, 878–881 (2003).

T. Brixner, G. Krampert, P. Niklaus, and G. Gerber,
Optimal control of molecular femtochemistry,
In D. R. Miller, M. M. Murnane, N. F. Scherer and A. M. Weiner (Eds.), *Proceedings of the XVth International Conference on Laser Spectroscopy*,
pp.85–95, World Scientific, (2003).

T. Brixner, C. Dietl, G. Krampert, P. Niklaus, E. Papastathopoulos, T. Pfeifer, R. Selle, G. Vogt, D. Walter, C. Winterfeldt and G. Gerber,
Adaptive femtosecond quantum control,
In F. Krausz, G. Korn, P. Corkum and I. A. Walmsley (Eds.), *Ultrafast Optics IV*,
Volume 95 of *Springer Series in Optical Sciences*, pp.119–128, Springer, Berlin
(2004).

T. Brixner, G. Krampert, T. Pfeifer, R. Selle and G. Gerber,
M. Wollenhaupt, O. Graefe, C. Horn, D. Liese, and T. Baumert,
Quantum control by ultrafast polarization shaping,
Phys. Rev. Lett **92**[20], 208301-1–208301-4 (2004).

G. Vogt, G. Krampert, P. Niklaus, and G. Gerber,
Optimal Control of Photoisomerisation,
Nature, submitted (2004).

G. Krampert, G. Vogt, P. Niklaus, F. Santoro and G. Gerber,
Photoisomerisation of NK88: Dynamics and Control,
In preparation.

T. Brixner, G. Krampert, T. Pfeifer, R. Selle and G. Gerber,
M. Wollenhaupt, O. Graefe, C. Horn, D. Liese, and T. Baumert,
Adaptive polarization control of molecular dynamics,
In T. Kobayashi, T. Okada, T. Kobayashi, K. A. Nelson and S. DeSilvestri (Eds.),
Ultrafast Phenomena XIV,
Volume XX of *Springer Series in Chemical Physics*, in press, Springer, Berlin
(2005).

G. Krampert, P. Niklaus, G. Vogt, and G. Gerber,
Teaching lasers to twist molecules,
In T. Kobayashi, T. Okada, T. Kobayashi, K. A. Nelson and S. DeSilvestri (Eds.),
Ultrafast Phenomena XIV,
Volume XX of *Springer Series in Chemical Physics*, in press, Springer, Berlin
(2005).

Further publications beyond the scope of this work:

L.T. Nieman, G. Krampert, and R.E. Martinez,
*An apertureless near-field scanning optical microscope and its application to
surface-enhanced Raman spectroscopy and multiphoton fluorescence imaging*,
Rev. Sci. Instrum. **72**(3), 1691–1699 (2001).

Contents

List of Publications	iii
1 Introduction	1
2 Theoretical Concepts	5
2.1 Quantum Control	5
2.1.1 Introduction	5
2.1.2 Optimal Control	7
2.1.3 Control of Chirality	11
2.2 Polarization-sensitive Processes	14
2.2.1 Introduction	14
2.2.2 Polarization-Sensitivity in Isotropic Ensembles	16
3 Experimental Implementation	19
3.1 Femtosecond Laser Pulses	19
3.1.1 Generation of Femtosecond Laser Pulses	20
3.1.2 Mathematical Description	22
3.2 Femtosecond Pulse Shaping	25
3.2.1 Phase-only Pulse Shaping	25
3.2.2 Frequency-Doubling of Shaped Laser Pulses	28
3.3 Laser Pulse Characterization	33
3.3.1 FROG and XFROG	33
3.3.2 Spectral Interferometry	37
3.3.3 Joint Time-Frequency Representation	40
4 Ultrafast Polarization Shaping	43
4.1 Generation and Characterization	43
4.1.1 Polarization Pulse Shaper Setup	44
4.1.2 Mathematical Description and Experimental Characterization	47
4.2 Polarization-Modulation	51
4.2.1 Polarization-Modulation by Subsequent Optical Elements	51
4.2.2 Compensation Schemes for Phase Distortion	52
4.3 Jones-Matrix Calculus	54

4.4	Adaptive Polarization Shaping	57
4.4.1	Linear Polarization as Target	58
4.4.2	Compensation for Dispersion and Polarization Distortion	61
4.5	Conclusion	63
5	Ultrafast Polarization Quantum Control	65
5.1	Introduction	65
5.2	Polarization-Sensitive Dynamics in the K_2 -System	66
5.3	Quantum Control of K_2	72
5.4	Conclusion	75
6	Optimal Control of Photoisomerization	77
6.1	Introduction	77
6.2	Photoisomerization Dynamics of NK88	80
6.3	Quantum Control of NK88	83
6.3.1	Polarization-Shaping Scheme for NK88	83
6.3.2	Optimal Control of NK88	85
6.4	Conclusion	88
7	Summary and Outlook	89
8	Zusammenfassung und Ausblick	91
A	Control of Bond-Selective Photochemistry in CH_2ClBr	95
A.1	Bond-Selective Photochemistry in Haloalkanes	95
A.2	Optimal Control of CH_2ClBr	96
A.3	Conclusion	105
	Bibliography	107
	Acknowledgements	127
	Curriculum Vitae	129

1 Introduction

“I call our world Flatland, not because we call it so, but to make its nature clearer to you, my happy readers, who are privileged to live in Space.”

Edwin A. Abbott [1], 1884

In his novel *Flatland*, published under the pseudonym A. Square, Edwin A. Abbott describes from the perspective of a square the manner and the problems of perceiving dimensions. He gives a very comic account of the journey of the square to the inhabitants of Pointland (zero dimensions) and Lineland (one dimensions) and the way in which they are satisfied with their universes. Although the square tries to explain to those lower dimensional beings the nature of two dimensions and is somewhat amused about their inability to understand the limitations of their view, the square itself is enraged, when he is visited by a sphere and forced to accept the existence of another dimension.

Though published at the end of the 19th century, the novel has lost nothing of its relevance in the 21st century. The possibilities that further dimensions bring about are still hard to anticipate. Some striking parallels can be drawn from this novel to the field of femtosecond laser pulse shaping and quantum control, which is the subject of this thesis. Until recently femtosecond laser pulse shaping has relied on shaped pulses which are linearly polarized and do not change their polarization state during their duration. That means the electric field of these laser pulses oscillates only in one plane. In a sense shaped laser pulses have been inhabitants of Flatland. Through the technique of femtosecond polarization pulse shaping the possibilities of a new dimension are opened up for quantum control. The electric field of polarization-shaped femtosecond laser pulses oscillates truly in three dimensions.

These “three-dimensional” shaped laser pulses are of particular interest for the field of quantum control. In this scheme one makes use of the coherent properties of laser light to influence the quantum-mechanical dynamics of systems on the microscopic level. For example this has been applied to control photochemical reactions, quantum optics (optimization of high harmonic generation), atomic (Rydberg electron wave packet sculpting) and molecular physics (selective photoexcitation), biochemistry (energy transfer in light harvesting complexes) and solid-state physics (coherent photocurrent control). In all these examples only

the scalar properties of the laser light were used and the vectorial character of the electric field ignored. It is immediately apparent, given that the controlled quantum systems are three dimensional and exhibit 3D dynamics, going from “flat” to “3D” laser pulses would open up many new perspectives in the control of coherent light–matter interaction.

However, the Hamiltonian of most quantum systems is so complicated that the calculation of the shape of the controlling laser field is a very challenging task and often not feasible for more complex systems. Thus the suggestion to use the quantum system itself to find the optimal laser field for a set control objective was a major breakthrough. In their seminal work “Teaching lasers to control molecules” [2] Judson and Rabitz proposed letting the molecule itself solve its Schrödinger Equation under the presence of the tailored laser field and using the experimental observables in a learning loop to iteratively find the best adapted laser field for the control task. If now not only the scalar properties of the light–matter interaction but also the vectorial ones are addressed, this approach should prove particularly helpful. As a result of this “closed loop” approach no a–priori knowledge about the potential energy surfaces and transition selection rules is necessary in order to reach the user set control objective using an optimally shaped laser pulse.

The timescale on which the laser pulses needs to be shaped is of course tied to the timescale of the quantum-mechanical motion. For chemical reactions the natural timescale is on the order of a few tens of femtoseconds up to several picoseconds. With the progress in ultrafast laser technology in the last 20 years it is now routinely possible to monitor chemical reactions in real time. But from the observation of the making and breaking of chemical bonds it is only one further step to the control of chemical reactions on the microscopic level. The key ingredient here is femtosecond pulse shaping technology to tailor the laser pulse on an ultrafast time scale. The combination of femtosecond pulse shaping and adaptive quantum control has been called adaptive femtosecond quantum control. This field could profit significantly from the shaping of the polarization state of femtosecond laser pulses. To what extent the control could be enhanced going from “flat” to “3D” shaped pulses, has still to be investigated.

But also the 3D dynamics of quantum systems is not fully investigated yet. The question remains, whether the large scale, coherent motion of complex molecular groups in a photoisomerization reaction is controllable using shaped femtosecond laser pulses. This work will address those two questions with several experiments. It is organized as follows.

After this introduction, the theoretical concepts used in quantum control are detailed. Special emphasis is laid on two theoretical suggestions to use polarization–shaped laser pulses in order to purify a racemate of chiral molecules. In the following section some more general schemes how to exploit polarization–sensitive processes in molecules are briefly sketched. In Chapter 3 the experimental implementation of these concepts is described. Also, a mathematical

description and some experimental characterization methods of shaped femtosecond pulses are given. The generation and characterization of polarization-shaped femtosecond laser pulses is shown in Chapter 4. The combination of polarization-shaped laser pulses and closed-loop learning control is tested in optical demonstration experiments. The technique of adaptive polarization shaping is then applied to a model quantum system in Chapter 5. The polarization dependence of multiphoton ionization of the potassium dimer system K_2 is first investigated in a pump-probe experiment and then exploited in a quantum control experiment using polarization as an active agent.

In Chapter 6 the *cis-trans* photoisomerization reaction of 3,3'-diethyl-2,2'-thiacyanine iodide (NK88) is investigated in the liquid phase using transient absorption spectroscopy. First the isomerization dynamics are studied with unshaped laser pulses. The experiment moves then from simple observation to active control over the *cis-trans* photoisomerization reaction employing the method of adaptive femtosecond quantum control. The successful optimization proves the feasibility of using shaped laser pulses to control the modification of the molecular geometry. Finally this work is summarized in Chapter 7 and an outlook on possible applications of polarization-shaped laser pulses as well as on extending the wavelength range, in which polarization shaping is possible, is given. The appendix describes an adaptive femtosecond control experiment on bond-selective photochemistry in CH_2BrCl . It addresses the possibility of quantum control in the presence of strong non-adiabatic coupling between two reaction channels.

2 Theoretical Concepts

This thesis deals with the subject of adaptive control of quantum-mechanical systems on a microscopic scale. Special emphasis is laid on the control of chemical reactions, in particular addressing and exploiting the full three-dimensional, spatio-temporal properties of quantum wavefunctions. In this chapter, the theoretical concepts used in quantum control are briefly introduced from a historical point of view (Section 2.1.1). In Section 2.1.2 the use of adaptively shaped femtosecond laser pulses in the control of chemical reactions will be specifically stressed. In the following some theoretical suggestions are presented on how this field might profit from the manipulation of the polarization state of the laser pulse on a femtosecond time scale (Section 2.1.3). The chapter concludes with a brief summary of polarization-sensitive processes in molecules in general (Section 2.2).

2.1 Quantum Control

2.1.1 Introduction

Ever since the invention of the laser it has been an implicit dream to use its properties to control quantum systems, in particular molecules undergoing chemical reactions. One of the first ideas was to use the spectrally narrow laser radiation to selectively excite the vibrational mode of one particular chemical bond and to deposit enough quanta of energy in it, so that it would eventually dissociate [3, 4]. Yet, it turned out that in most molecules the energy would redistribute to other vibrational modes on a very short time scale. This process, called intramolecular vibrational energy redistribution (IVR) [5–7], would limit the selectivity to the extent that in many molecules predominantly the weakest bond would break, although a different, stronger bond was originally selectively excited. In essence the laser excitation would act as a simple increase in temperature. However, IVR is not a decoherent process. And what is more, if the intramolecular coupling terms are taken into account, the quantum-mechanical evolution of the energy flow can be controlled by interference effects between multiple excitation pathways. Rather than using the spectral narrowness one can exploit the coherent properties of laser radiation to achieve selectivity.

Historically, there have been three different schemes, which make use of the coherent properties of lasers. Although each of them stresses different aspects

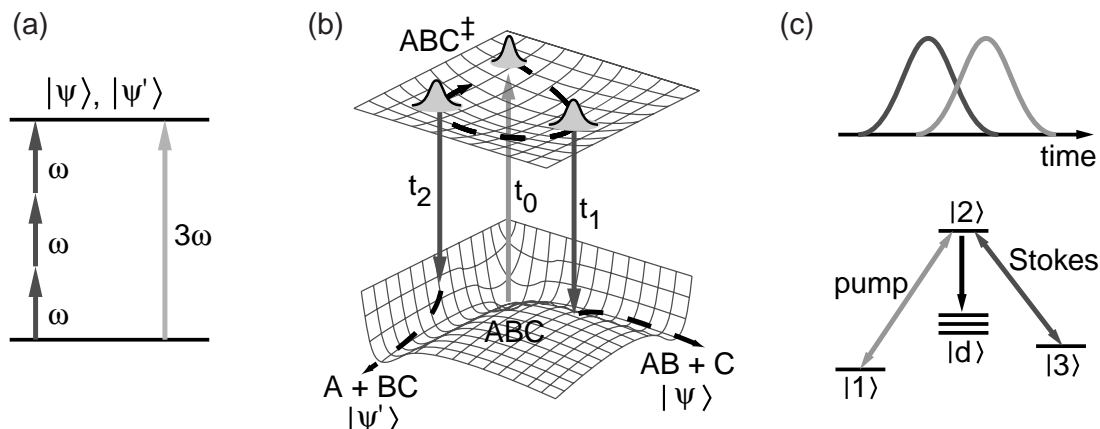


Figure 2.1: Quantum Control Schemes. The Brumer–Shapiro phase control (a) creates interference by coupling the initial and final state via a one-photon and three-photon transition. By varying the relative phase between the ω and 3ω radiation, selectivity can be achieved. The Tannor–Kosloff–Rice pump–dump scheme (b) is more easily understood in the time domain. It uses the coherent wave–packet evolution after a short excitation laser pulse to dump the wave packet after suitable time delay preferentially into one exit channel. The STIRAP technique (c) by Bergmann and coworkers transfers the population from initial state $|1\rangle$ to final state $|3\rangle$ via intermediate state $|2\rangle$ with a counter-intuitive sequence of nanosecond laser pulses. Thereby the transient population in state $|2\rangle$ remains zero, thus avoiding losses to dissipative levels $|d\rangle$.

of the coherent laser–matter interaction, they all rely on quantum-mechanical interference effects [8, 9] in order to control chemical reactions. The working principle of these schemes is sketched in Fig. 2.1. The first scheme was proposed by Brumer and Shapiro [10, 11]. It stresses the interference effects in the frequency domain. In their approach the ground state is coupled to degenerate final states $|\Psi\rangle$, $|\Psi'\rangle$ via a one-photon and a three-photon transition. If the relative phase between the ω and 3ω radiation is tuned, constructive and destructive interference in the population of final states $|\Psi\rangle$ and $|\Psi'\rangle$ can occur on condition that there exists a phase lag between the two excitation pathways. The source of this phase lag is non-trivial and one has to rely on numerical calculations to predict it. Nonetheless, this scheme has been experimentally verified on atoms [12] and small molecules [13, 14].

The second scheme, pump–dump control, is easier to explain in the time domain than in the frequency domain. It was first proposed by Tannor, Kosloff and Rice [15, 16]. A short (femtosecond) pump laser pulse is used to create a wave packet on the excited electronic state energy surface of the molecule. If during the free temporal evolution the wave packet is centered at some later time over the desired exit channel, the wave packet is dumped with a second short laser pulse to the ground state. But in general, the wave packet tends to spread

and to develop a very complex amplitude distribution. It then has very little Franck–Condon overlap for a transition to desired regions on the ground state potential energy surface and is thus limiting the effectiveness of this method. Besides, for this scheme to work, the wave packet on the excited energy surface has to reach the desired nuclear configuration to dissociate the selected bond. This technique has been experimentally demonstrated in the photo-dissociation of small molecules [17–19].

The third scheme, known as stimulated raman adiabatic passage (STIRAP), has been proposed and experimentally demonstrated by Bergmann and coworkers [20, 21]. In this technique, nanosecond lasers are used to control λ -type systems. The temporally overlapping pump laser, coupling state $|1\rangle$ and $|2\rangle$, and stokes laser, coupling $|2\rangle$ and $|3\rangle$, are applied in a counter-intuitive way, i.e. the stokes laser first. If one uses this scheme, 100% transfer of population can be achieved while the transient population in state $|2\rangle$ remains zero at all times. So the dissipative loss channels $|d\rangle$ associated with state $|2\rangle$ can be avoided. The whole scheme can be understood in the dressed state picture. For this purpose an extensive review of the STIRAP technique is given in Ref. [22].

While all these schemes look rather different at first glance, they all just stress different aspects of the same more general effect of quantum-mechanical interference in the time or frequency domain [23]. A more general scheme, which makes use of all aspects of coherent light–matter interaction, i.e. in this sense optimal use, will be presented in the next section.

2.1.2 Optimal Control

Optimal control uses arbitrary temporal and spectral evolution of the control field in order to achieve the set task. Since the time scale on which many chemical reactions happen is the femtosecond to picosecond range, shaped femtosecond pulses are often used to experimentally realize such an optimal control scheme. Instead of preparing a wave packet and letting it evolve freely until it is dumped by a second laser pulse like in the Tannor–Kosloff–Rice scheme, the wave packet is constantly manipulated by the different components of the shaped laser pulse. A very intuitive picture of optimal control is to shape the laser pulse in order to provide the right frequencies at the correct Franck–Condon time windows to transfer the wave packet to different potential energy surfaces, where its evolution is more favourable for the set control goal. Yet optimal control cannot only be seen as an extension of the Tannor–Kosloff–Rice scheme but also as a more general implementation of the Brumer–Shapiro technique. Instead of the quantum-mechanical interference between two pathways from the ground state to degenerate excited states coupled by two frequencies ω and 3ω , optimal control can be understood as the interference between all pathways that can be accessed by the many different frequencies of the shaped ultrashort laser pulse. A very convincing example for this interpretation of optimal control is the control of the

two-photon excitation of Cs with shaped laser pulses [24]. There, only the phase between any two frequencies whose sum of photon energies match the two-photon transition matters.

These two schemes only use one parameter to control the chemical reaction. In contrast to this, in optimal control many parameters characterizing the spectral and temporal properties of the optimal laser pulse have to be found. The theoretical solution approach using optimal control theory (OCT) on this many-parameter quantum control problem has been developed by Rabitz and coworkers [25, 26] as well as Kosloff and coworkers [27]. The principle of OCT is briefly outlined in the following. One chooses the target wave function Ψ_T at a final time t_f and tries to maximize the overlap of $|\langle \Psi_T | \Psi(t_f) \rangle|^2$ under the constraint that the Schrödinger Equation is satisfied. Since the Schrödinger Equation contains the interaction term $\vec{\mu} \cdot \vec{E}(t)$ with $\vec{E}(t)$ being the control field, the overlap is a functional of the electric field $\vec{E}(t)$. The problem to maximize this functional while satisfying the Schrödinger equation is solved by using a Lagrange multiplier technique. Further constraints like finite pulse energy or an upper limit on the fastest temporal features in the control field, i.e. constraining the spectral bandwidth, can be imposed by defining further “cost functionals”. The task to maximize the sum of all these functionals is performed using a variational approach and solving the resulting coupled nonlinear differential equations numerically in a self-consistent iterative calculation scheme.

However, the computational effort is quite substantial and OCT requires precise knowledge of the molecular Hamiltonian. At present, the molecular Hamiltonian can only be calculated ab initio for small systems containing up to three or four atoms. Besides, the accuracy of such calculated or measured potential energy surfaces is often not sufficient for larger or more complicated molecules. Therefore, the approach is often limited to small systems. Furthermore, simplification of the molecular Hamiltonian is necessary. For example, part of the Hamiltonian is treated quantum-mechanically exact and the rest as coupling to background states. Jakubetz and coworkers [28] have shown that even for the small molecule HCN the calculated optimal control field is not stable with respect to variations in the couplings to these background states. That means small variations in the strength of these couplings do not negate the existence of a viable control field, but they may change the shape of the optimal field significantly. The use of these reduced basis sets therefore may be a restriction on the experimental implementation of theoretically predicted optimal control fields.

Another problem is the experimental realization of the control field at the position of the experiment. Due to experimental limitations in the shaping process or the pulse shape modifications, e.g. through material dispersion, along the beam path from the pulse shaper to the experiment, this approach might not be feasible.

Judson and Rabitz proposed a solution to these problems in their seminal work “Teaching lasers to control molecules” [2]. Their approach involves closing

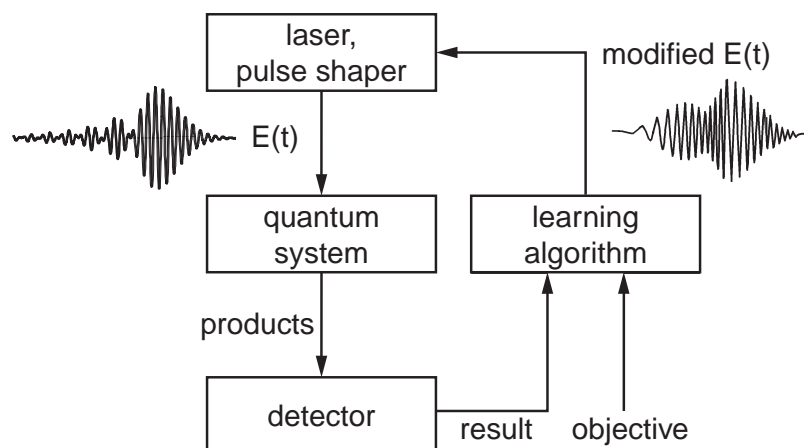


Figure 2.2: Adaptive Quantum Control. The quantum system is excited by shaped femtosecond laser pulses provided by the combination of a femtosecond laser system and a pulse shaper. The outcome of the initiated photophysical or photochemical process is detected and the information about the photoproducts is fed to a learning algorithm. This algorithm iteratively improves the pulse shape depending on the experimental measurements and a user set control objective.

the loop and letting the molecule itself guide the search for the optimal control field under the fundamental (satisfying the Schrödinger Equation) and experimental (possible pulse shapes) restrictions present. This scheme is depicted in Fig. 2.2. The quantum system is excited by shaped femtosecond laser pulses provided by the combination of a femtosecond laser system and a pulse shaper. The outcome of the initiated photophysical or photochemical process is detected and the information about the photo products is fed into a learning algorithm. This algorithm iteratively improves the pulse shape depending on the experimental measurements and a control objective set by the experimenter. For the optimization algorithm, which basically belongs to the class of global search algorithms, simulated annealing [29] and evolutionary algorithms (EA) [30, 31] have been used. In this work only EA have been employed and therefore the following discussion is limited to this type of optimization algorithms. The working principle of such an algorithm is sketched in Fig. 2.3. EA try to mimic the biological process of evolution. They start with a number of random individuals, in this case randomly shaped laser pulses. Depending on the experimental results obtained with these laser pulses, they assign the individuals a certain fitness value. From this group of individuals, called by analogy to biology a generation, the fittest are selected for the next generation. This next generation is constructed from the fittest individuals of the previous generation by cloning, mutation and crossover. By iteration of this procedure eventually an optimum is found for the user defined control task. EA are sometimes differentiated in evolution strategies (ES) and genetic algorithms (GA), but the distinctions are fluent and often

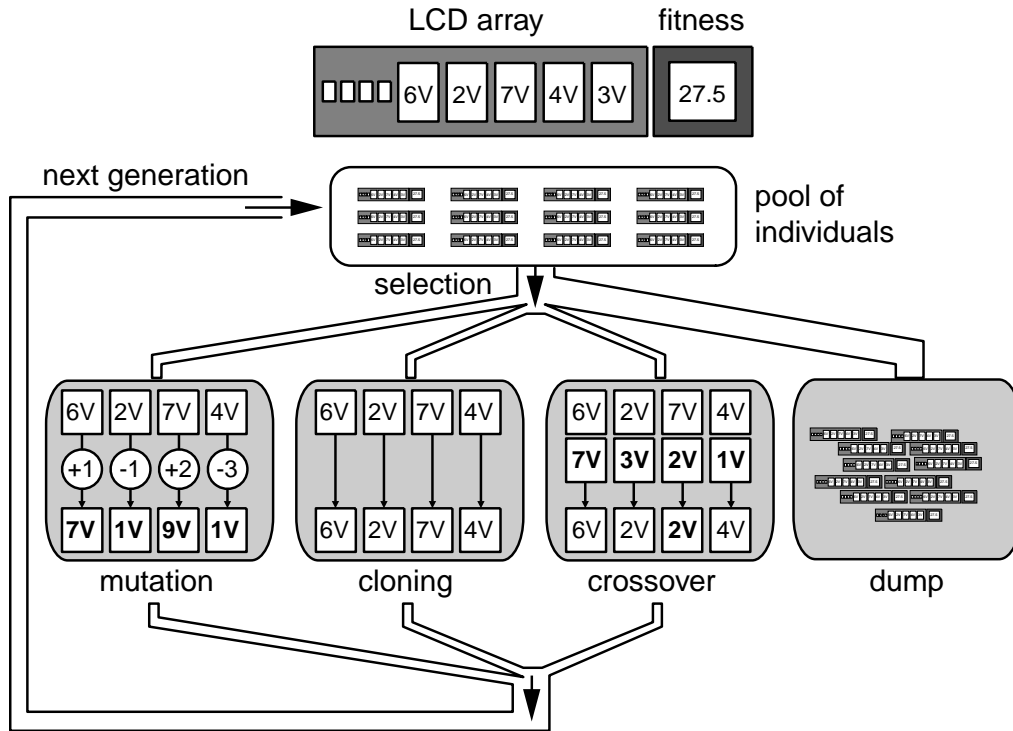


Figure 2.3: Evolutionary algorithm. This diagram shows one cycle of an evolutionary algorithm. Each individual within the population pool represents a specific laser pulse shape (i.e., specific LCD pixel voltage values). Depending on the fitness, an individual is either selected for reproduction or it is rejected. Reproduction operations include mutation, cloning, and crossover of the LCD voltage arrays. The individuals thus produced constitute the next generation, which is then evaluated in the same way. Iterating through this loop many times finally leads to optimized laser pulse shapes.

mixed types of algorithms are used. In general ES employ a floating number representation of the individuals, in this case the different pulse shapes, which has a direct physical meaning, like e.g. the phase at certain frequency positions or the Taylor coefficients of the Taylor expansion of the phase function $\Phi(\omega)$. GA in contrast use a binary representation and rely more on the crossover between two successful individuals in order to produce new individuals for the next iteration of the algorithm. ES, however, depend more on the mutation of successful pulse shapes for the iterative improvement. Here, an ES with some elements from a GA (crossover) is employed. Information on the exact implementation of the algorithm can be found in the dissertations by Seyfried or Brixner [32, 33].

As it is the problem with all global search algorithms, the question whether the reached optimum is global or local cannot be answered in general. One also has to be very careful when trying to extract information about the investigated quantum system from the evolution of the optimization. The speed of improve-

ment in fitness not only depends on the controlled quantum system, but also to a large degree on the exact implementation and parameters of the evolutionary algorithm.

However, the great advantage of this closed-loop learning control is that no a-priori knowledge about the molecular Hamiltonian is required. The method makes indeed optimal use of all accessible states of the quantum system in order to achieve the set control task. The drawback, on the other side, is that the optimal pulse shape often provides very little insight into the exact control mechanism. This problem is sometimes called the problem of inversion and remains one of the main challenges in the field of optimal control. Only a close cooperation between theory and experiment can sometimes shed a little light on this problem [34, 35].

Nevertheless this field has seen tremendous experimental progress. From the first control of excited state population of a laser dye [36] and the controlled dissociation of $\text{Fe}(\text{CO})_5$ in the gas phase, the technique has advanced to the control of energy transfer in large biological systems [37] and the controlled modification of the geometry of large molecules in the liquid phase [38]. Selective excitation of different vibrational modes in a liquid [39] as well as selective electronic excitation of dye molecules [40] have been demonstrated.

All of these experiments relied on the manipulation of the scalar properties of the femtosecond laser pulse, e.g. the momentary frequency, intensity or phase. The electric field, however, is a vectorial quantity. A lot of possibilities arise, if the vectorial character, i.e. the polarization state, could also be manipulated. The next section will briefly outline some theoretical proposals for this new level of quantum control.

2.1.3 Control of Chirality

One very exciting possibility would be the control of chiral molecules, if it was feasible to tailor the electric field also in its vectorial properties. Chiral molecules exist in two species called enantiomers, which only differ from each other in their geometry with one being the mirror image of the other. The two forms are called L- and R-enantiomers as they resemble a left- respectively right-handed geometry. Chirality is a very important phenomenon in biochemistry because biochemical reactions involving chiral molecules often require one specific enantiomer of the two possible ones. In particular the fact that all life on earth utilizes only the L-enantiomers of amino acids is known as homochirality of life. It has triggered off long standing interest as to its origin and is one indication that the biochemical origin of life might be extraterrestrial [41, 42].

Chemical reactions can produce one enantiomer selectively, only if chiral catalysts or reactants are involved or if some external chiral influence is present. But, if this is not the case, an equal mixture of both enantiomers, called a racemate, will be produced. Due to the chiral selectivity of biochemical reactions only one enantiomer has the desired effect, e.g. as medical treatment, whereas the other

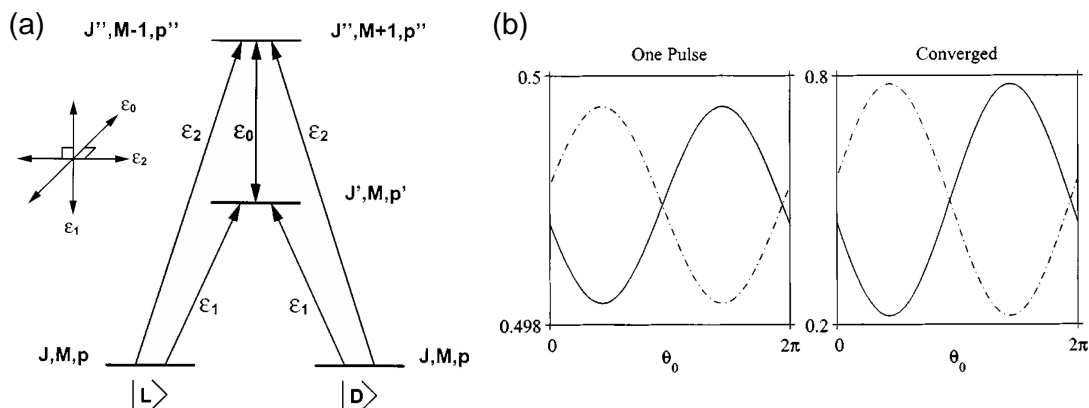


Figure 2.4: Control of Chirality. In this simplified model (a) the ground states of the $|L\rangle$ and $|D\rangle$ enantiomer are coupled by two laser pulses ε_1 and ε_2 to two achiral, excited states. These excited states are in turn coupled by a third laser ε_0 . Note that all three lasers have mutually orthogonal linear polarizations. As a function of the phase Θ_0 of laser pulse ε_0 different enantiomeric excess can be achieved (b). The ratio of $|L\rangle$ to $|D\rangle$ enantiomers can be further enhanced, if the laser pulse sequence is applied repeatedly. Figure taken from Ref. [48]

might be harmful. Therefore, it has been a long standing dream in chemistry to purify a racemate.

In principle, photochemistry with circularly polarized light can influence the chirality. However, since the effects involved here, like e.g. natural circular dichroism or magneto-chiral dichroism [43–45], rely on magnetic dipole interactions, the cross sections are very small and the achievable enantiomeric excess is very limited. In recent years there has been great theoretical effort to check whether quantum control techniques can achieve a substantial enantiomeric excess in a photochemical reaction. Most prominent are two proposals: one by Brumer, Shapiro and coworkers [46–48] and another by Fujimura, Manz and coworkers [49–51].

The scheme by Brumer and Shapiro relies on an extended version of the phase control scheme introduced in Section 2.1.1, which is shown in Fig. 2.4. The chiral ground state of the L- and D-enantiomer are coupled by two laser pulses ε_1 and ε_2 to two excited, achiral excited states, which in turn are coupled by a third laser ε_0 . The crucial requirement now is that all three lasers have mutually orthogonal laser polarizations. However, this combination of three mutually orthogonal laser polarizations allows to use a randomly oriented sample [52] and therefore does not require any techniques to align the molecules in an experimental realization of this scheme. As can be seen in Fig. 2.4b the enantiomeric excess after one pulse sequence is rather small, but still orders of magnitude higher than in conventional photochemistry with circularly polarized light. Therefore, the pulse sequence has to be applied repeatedly to achieve a substantial excess. Another drawback concerning the experimental realization is that it is not clear what will

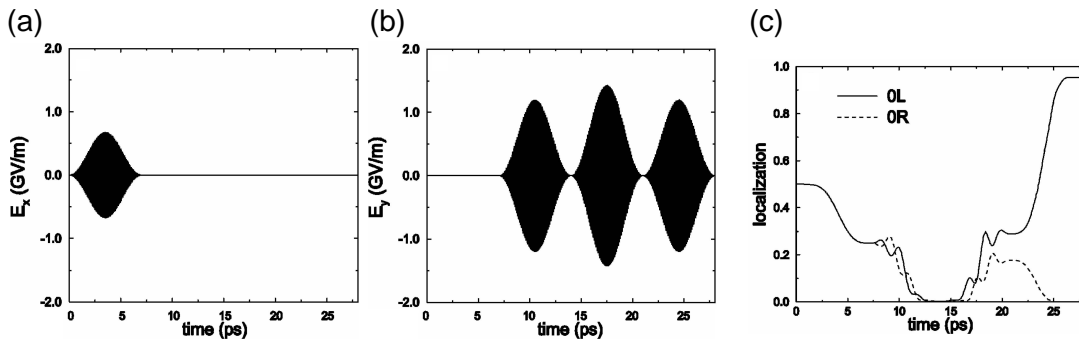


Figure 2.5: Selective preparation of the left enantiomer of H_2POSH by a series of four linearly x (a) and y -polarized (b) laser pulses. A z -polarized laser pulse is applied beforehand to orientate the molecule. The time evolution of the localization (c) shows the respective ground state populations of the L and R enantiomer. Figure taken from Ref. [49]

happen, if the laser pulses ε_1 and ε_2 overlap spectrally. Moreover, the fact that the electronic excitation ε_1 and ε_2 is most likely in the UV wavelength range and the coupling laser ε_0 in the mid-infrared also poses an experimental challenge.

The most fundamental obstacle is that the model predicts the opposite enantiomeric excess for a sign reversal of the electric field. As will be shown in the next chapter, the phase of the oscillation of the electric field under the pulse envelope is not fixed. In a conventional laser system it slips from pulse to pulse. Furthermore, pulse shaping techniques do not allow to influence this slip in the absolute phase. And what is even worse, conventional pulse characterization techniques cannot measure it. Progress in the stabilization of the absolute phase has only recently been made in special pulse generation setups [53, 54].

The scheme by Manz and Fujimura is based on an extended version of pump-dump control involving several pump and dump pulses. It also employs three mutually orthogonal polarization components [51]. Unlike the first scheme, one component is used to orientate the molecule and the other two for controlling the chirality. The pulse sequence in these two components is depicted in Fig. 2.5a and b. As can be seen from Fig. 2.5c the theory predicts a macroscopic enantiomeric excess after interaction with one optimally shaped laser pulse sequence. However, the fact that $\vec{E}(t) \rightarrow -\vec{E}(t)$ produces the opposite enantiomeric excess is also true for this scheme [51]. In other words, the experimental realization of this scheme would also require a femtosecond laser system with a stabilized absolute phase.

In conclusion, quantum control of chirality remains one of the most intriguing, but also most challenging prospects in coherent light-matter interactions. The dependence of these control schemes on the sign of the electric field and therefore on the absolute phase of the carrier oscillation with respect to the pulse envelope poses a demanding problem concerning an experimental realization. Nevertheless,

polarization-shaped laser pulses can increase the level of control in quantum systems and might simplify the experimental realization of control of chirality by replacing two polarization components in these models by one polarization shaped laser pulse. Some examples of less complicated processes sensitive to changes in the polarization of the exciting laser pulse are given in the next section.

2.2 Polarization-sensitive Processes

2.2.1 Introduction

All light-induced processes in molecules depend on the polarization of the exciting laser, since the interaction Hamiltonian in the electric dipole approximation is

$$H_1(t) = -\vec{\mu} \cdot \vec{E}(t), \quad (2.1)$$

where $\vec{\mu} = -e \cdot \vec{r}$ is the electric dipole moment. That means the absorption of polarized light in photochemical processes, for instance, depends upon the alignment of the molecule with respect to the polarization direction. This follows directly from the symmetry selection rules, that govern which transitions between which states are allowed for a given polarization direction. A simple example is the vibrational excitation of the linear molecule CO_2 , where the fundamental asymmetric stretch mode is excited by light polarized along the molecular axis, whereas the fundamental bending mode is excited only by light polarized perpendicular to the molecular axis.

Since one is now able to change the polarization state on an ultrafast timescale, as will be shown in Chapter 4 and 5, one can move on from these stationary examples to the case where the direction of the transition dipole moment changes during the dynamical evolution of the quantum system. An immediately apparent example is the photoisomerization of molecules. Since during this process the different nuclei of the molecule move with respect to each other, also the electronic orbitals will change their shape and orientation in space. Thereby, of course, also the transition dipole moments will alter their direction. In order to control such an isomerization reaction with shaped femtosecond laser pulses, it would be advantageous to tailor also the polarization state of these pulses in addition to their scalar properties, like momentary frequency and temporal amplitude. Thus, one would be able not only to provide the correct frequency at the right time, but also to spatially follow the dynamics with the polarization direction throughout the chemical reaction.

However, often these polarization effects are averaged out when dealing with a sample of randomly aligned molecules. In such an isotropic ensemble the interaction term must be averaged over all possible orientations of the molecule and thereby often the sensitivity to the polarization state of $\vec{E}(t)$ is lost. Thus, one solution is to break the isotropy by using a prealigned molecular sample. This

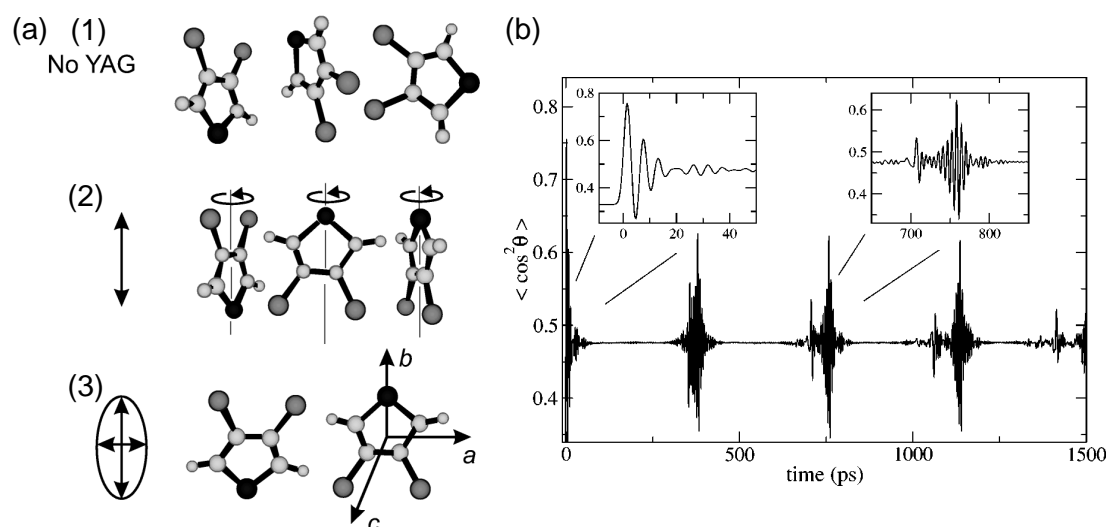


Figure 2.6: Laser alignment of molecules. The adiabatic alignment technique (a) uses a non-resonant, nanosecond laser (YAG) to align molecules along their symmetry axis. In this figure the orientation and rotation of the molecule 3,4-dibromothiophene for the case of no YAG laser (1), linearly polarized (2) and elliptically polarized YAG laser (3) is shown. The non-adiabatic method (b) uses an ultrashort laser pulse centered at $t = 0$ to create a rotational wave packet. The theoretical curve shows the degree of alignment of iodobenzene as a function of delay time. Note the field free alignment during the rotational revivals at 350 ps and 700 ps, for example. Figures taken from Ref. [59, 60]

alignment can be achieved by bringing the molecules onto a suitable surface. Molecules, for example, that can only bond to the surface at one position in the molecule can form a so-called self-assembled monolayer [55]. Another possibility for alignment is to bring hydrophobic molecules onto water surfaces, where they form an orientated layer. However, these methods are limited to certain molecules and the dynamics of the molecules might be rather different on the surface than in solution. Nevertheless, using chiral molecules aligned on a surface, Shen and coworkers were able to observe optical activity in sum-frequency generation and so to use nonlinear optics to probe molecular chirality [56, 57].

If it is not feasible or desirable to use molecules aligned on a surface, another possibility is laser alignment [58] of molecules. Here, two techniques are most prominent: adiabatic alignment in non-resonant laser fields [59] and non-adiabatic alignment via rotational wave-packet revivals [60]. Both methods are shown in Fig. 2.6. In the adiabatic method intense, non-resonant, nanosecond lasers are used to align molecules along the direction of their highest polarizability. Since the pulse duration is much longer than a rotational period, the field-free eigenstates transform adiabatically into the eigenstates with the field present, which are called pendular states. Similarly during the switch-off of the

field the molecules return adiabatically to their original field-free eigenstates, i.e. the ensemble becomes isotropic again and all alignment reached in the pendular states is lost. In these pendular states the molecule librates about the polarization axis because of its polarizability anisotropy, in such a way as to minimize its energy in the external electric field of the nanosecond laser. In the non-adiabatic method, on the other hand, the used pulse duration is much shorter than a rotational period. This short laser pulse leaves the system in a coherent superposition of rotational eigenstates that is aligned upon turn-off, dephases and subsequently revives and dephases periodically in time.

The major drawback of all these techniques is that they complicate the required experimental setup for quantum control using polarization-shaped laser pulses. The needed additional lasers or laser beams must spatially overlap with the focus of the polarization-shaped laser pulses. And what is more challenging, the pulses have to be provided with the correct time delay. This requirement is especially crucial in the case of non-adiabatic alignment, since the molecules during a rotational revival change from maximal alignment to completely randomly aligned in a quarter of the rotational period. This can be seen in the right inset in Fig. 2.6b. Due to these additional complications it is therefore advantageous for a first demonstration of polarization control to look for polarization sensitivity in a randomly aligned ensemble of molecules. In the following a few examples of processes of this type are given.

2.2.2 Polarization-Sensitivity in Isotropic Ensembles

One idea is to use the laser polarization itself to break the isotropy and exploit polarization-sensitive effects. In order to achieve this, very high intensities must be used, and the process that predominantly occurs is tunnel ionization. In tunnel ionization the electron is ejected along the polarization direction and since the field is strong enough, it is subsequently accelerated by the electric field. As the light electric field is an alternating one, the electron will reverse its direction half a field cycle later. Whether it recollides with the ion is strongly dependent on the polarization state of the laser. From a simple, classical picture it is immediately obvious that it has a much higher return probability for linear than for elliptical polarization [61]. One process that can happen, when the electron recollides, is high harmonic generation (HHG) [62, 63]. Using polarization-shaped laser pulses to drive HHG one can obtain control over this process on an ultra-short timescale. Therefore, time-dependent polarization profiles are proposed for the generation [64, 65] and characterization [66] of attosecond HHG pulses.

Besides these ultrahigh intensity effects there is a rather general, polarization-sensitive process at much lower intensities. If one considers a multiphoton process with intermediate resonances, where the subsequent transitions involve different polarizations, the first part of the polarization-shaped laser pulse selects a suitably aligned subset of molecules and the rest of the laser pulse can then exploit

polarization effects in this aligned subset. It can be shown with a simple calculation, that this kind of process is not averaged out by the random orientation of the molecules. For the simple case of a two photon transition with an intermediate state, where the first transition is, for example, parallel and the second perpendicular to the molecular axis, one calculates the population in the final state for the two cases: in one case both photons have the same polarization and in the second they have polarizations perpendicular to each other. For the calculation one has to project the electric fields onto the two transition dipole moments. For this it is advantageous to use spherical coordinates. The excitation probability for each transition is then proportional to the square of this projection. The averaging over all orientations of the molecule is then done by integrating the excitation probability over all polar and azimuthal angles. This calculation yields an excitation probability that is increased by a factor of two for the case of two perpendicular linearly polarized electric fields compared to the case with parallel fields.

This can be made plausible by realizing that in the parallel case, for the first transition those molecules that are parallel to the field are optimally excited. However, these molecules cannot undergo the second transition, since the projection of the electric field onto the transition dipole moment is zero. Therefore the best result in this case is achieved when the molecule is orientated at 45° with respect to the polarization direction. But then, of course, for both transitions only a projection of the electric field, i.e. a factor of $1/\sqrt{2}$, will take part in the process. On the other hand, in the case of perpendicular polarizations the whole electric field is effective for both transitions in the optimal orientation of the molecule. Even after averaging over all orientations a factor two more excitation probability can be achieved in this case. This scheme is rather general, since the case of subsequent parallel and perpendicular transitions occurs rather often in molecules. To illustrate this point further let us consider the case of diatomic homonuclear molecules. Within the scope of this work only a very simplified consideration can be given. A more thorough description and introduction into the formalism can be found in many textbooks on molecular physics, e.g. by Bransden and Joachain [67] or Kuhn and Försterling [68], and an even more detailed picture is given in the textbook on diatomic molecules by Herzberg [69].

Whether a transition requires polarization parallel or perpendicular to the molecular axis, is governed by the parity selection rules. Since the electric dipole moment $\vec{\mu} = -e \cdot \vec{r}$ has odd parity, the parity of the initial and final electronic orbital must be different. Otherwise the matrix element $\langle \Psi_f | \vec{\mu} \vec{E} | \Psi_i \rangle$ vanishes due to symmetry considerations. For transitions between two Σ states the direction of the transition dipole moment can be determined by looking at the symmetry of the participating electronic orbitals. Examples of different σ orbitals are shown in Fig. 2.7a. As can be seen in the figure, the electron probability density in σ orbitals does not depend on the azimuthal angle. Therefore the only direction in which a change of sign after inverting a spatial direction $z \rightarrow -z$ (i.e. odd parity)

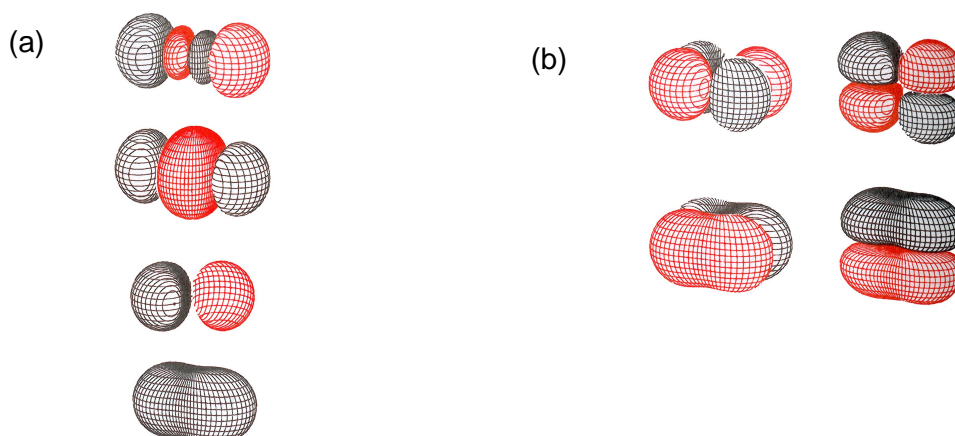


Figure 2.7: Electronic orbitals of a diatomic molecule. Different σ orbitals calculated using the LCAO (linear combination of atomic orbitals) method are shown in (a). For comparison different π orbitals are depicted in (b). In this figure black lines denote positive values, whereas red stands for negative values. The contour lines connects points in space where the same absolute value of the wavefunction is reached. Figure taken from Ref. [68]

can occur is along the molecular axis. This means that for a transition between two Σ states the transition dipole moment is parallel to the molecular axis. In general, the direction of the transition dipole moment can be ascertained by analyzing the parity of the involved orbitals. It can be shown, that a transition is parallel when the projection of the total electronic angular momentum onto the internuclear axis Λ does not change, i.e. for a $\Sigma \leftrightarrow \Sigma$, $\Pi \leftrightarrow \Pi$ or analogous transition. Whereas for transitions with $\Delta\Lambda = \pm 1$ the transition dipole moment is perpendicular to the molecular axis. It should be noted that this is only true as long as Λ is a good quantum number, i.e. as long as the selection rules for Λ are obeyed. These parity considerations can, of course, be generalized for larger molecules. There group theory provides the necessary mathematical tools to calculate the direction of the transition dipole moment. However, if the symmetry of the states involved in the process is not known, adaptive polarization shaping is a very useful technique. It allows to exploit polarization sensitivity in quantum control even in the case of incomplete knowledge about the molecule.

3 Experimental Implementation

In this chapter the experimental implementation of coherent control using shaped femtosecond laser pulses is described. The concepts introduced in the previous chapter are realized with ultrashort laser pulses. The source for these laser pulses is presented in Section 3.1.1 and a necessary mathematical description of these laser pulses is given (Section 3.1.2). The experimental setup to shape them is detailed in Section 3.2.1, and the effects of frequency-doubling of shaped femtosecond laser pulses are briefly outlined (Section 3.2.2). From the ability to almost arbitrarily shape laser pulses, the necessity arises to accurately characterize them. Two methods for this purpose, Frequency-Resolved Optical Gating (FROG) and Spectral Interferometry (SI), are depicted in Section 3.3.1 and 3.3.2 respectively. An intuitive joint time-frequency representation of femtosecond laser pulses is given in Section 3.3.3 in order to present differently measured pulses in a standardized way.

3.1 Femtosecond Laser Pulses

Only eight years after the invention of the laser [70] the first ultrashort pulses were demonstrated [71]. These laser pulses, estimated to be just picoseconds long, were produced using a passively modelocked Nd:glass laser. The next advance was the invention of colliding-pulse modelocked dye lasers [72], which eventually were able to produce laser pulses lasting only a few femtoseconds. Yet, their operation required huge pump power and proved to be complicated and very maintenance intensive. Since these first beginnings ultrashort laser systems have progressed from these large, temperamental and “power-hungry” predecessors to today’s reliable workhorses of ultrafast, time-resolved science in biology, chemistry and physics [73, 74].

The key discoveries that made this progress possible are the solid-state laser medium Ti:sapphire with a broad gain bandwidth extending from about 700 nm to 1100 nm [75] and the reliable mechanism for passive mode locking, i.e. Kerr-lens mode locking [76]. The Kerr-lens mechanism forces all longitudinal modes to “lock” their phases and thus to produce ultrashort pulses. The mechanism is shown schematically in Fig.3.1. Basically, all media show an index of refraction at very high intensities that depends linearly on intensity. As the laser beam inside

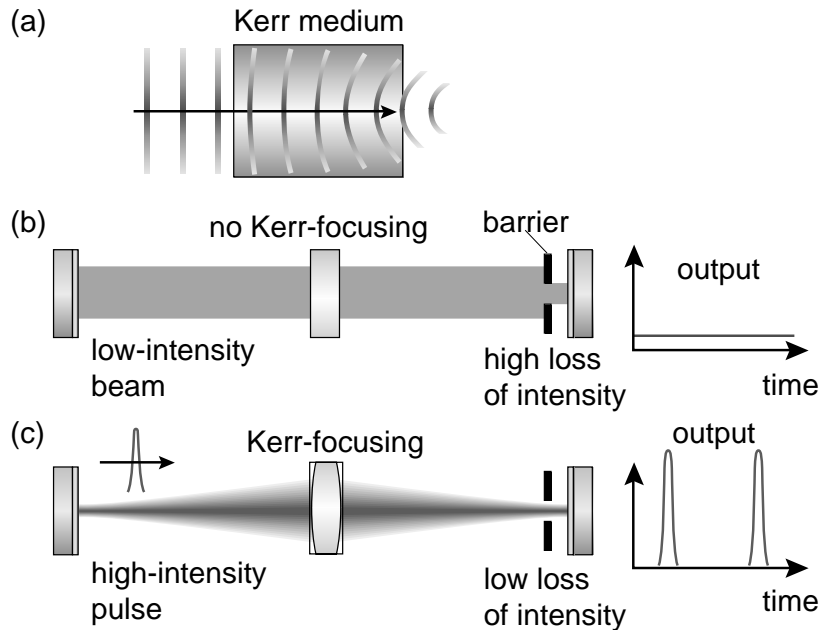


Figure 3.1: Kerr-lens modelocking. A suitable medium shows an intensity-dependent index of refraction at very high intensities (a). This can be used to favour the pulsed operation (c) over cw operation (b) of a laser. (taken from [73])

the resonator has a transverse gaussian profile, i.e. has higher intensity in the center of the beam, the medium acts as a lens for high intensities. The resonator introduces high losses for the low intensity cw modes via an aperture, whereas the high intensity pulsed mode has very small losses due to the Kerr lens. Therefore, the pulsed operation can start from initial optical noise, sometimes introduced via tapping a mirror or prism inside the resonator. Further more recent improvements were the development of compact, efficient, diode-pumped, solid-state lasers as pump-source and chirped mirrors [77] for intracavity dispersion compensation.

3.1.1 Generation of Femtosecond Laser Pulses

The lasers system used for most of this work (the experiments described in Chapter 5 being an exception) is shown schematically in Fig.3.2. It consists of a home-built Ti:sapphire oscillator that is optically pumped by an argon-ion, cw laser operated in multiline mode at 4 W. The oscillator produces 60 fs laser pulses at a repetition rate of 80 MHz with a pulse energy of 3 nJ at a central wavelength of 800 nm and with a spectral full width half maximum (FWHM) of 16 nm. Since for most experiments higher pulse energies are required, the oscillator pulses need to be amplified. However, direct amplification of femtosecond laser pulses leads to material breakdown of the amplifier gain material since the damage threshold is easily exceeded due to the high temporal peak intensities of femtosecond

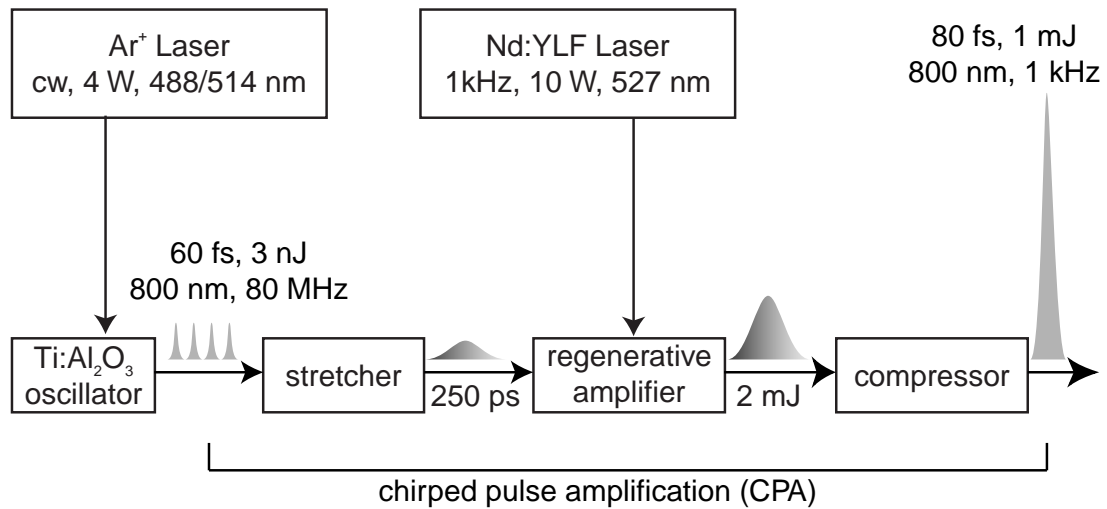


Figure 3.2: Femtosecond laser system. Femtosecond laser pulses from a high repetition rate Ti:sapphire oscillator are temporally stretched, amplified and recompressed in a chirped pulse amplification (CPA) system. At the output femtosecond laser pulses with a pulse energy of 1 mJ and a pulse duration of 80 fs are available for experiments at a repetition rate of 1 kHz.

laser pulses. Therefore, a more sophisticated amplification scheme, chirped pulse amplification (CPA), is employed, which was first demonstrated by Strickland *et al.* [78]. The idea is to first stretch the laser pulses temporally, then amplify them and recompress them afterwards. Thus very high temporal peak intensities in the amplifier can be avoided. The implementation here consists of a commercial Quantronix laser system, which is extensively modified in order to support a pulse duration of 80 fs of the amplified pulses. An appropriate setup of optical gratings, the so-called “stretcher”, introduces different path lengths for the different wavelengths of the laser pulse. Thereby, the pulse duration increases from 60 fs to about 250 ps. These temporally stretched laser pulses are then seeded into a regenerative amplifier, which in turn is pumped by a 1 kHz Q-switched Nd:YLF laser. After amplification, another setup of optical gratings, the “compressor”, compensates the phase introduced by the stretcher and recompresses the laser pulses in time. Due to nonlinear gain narrowing in the regenerative amplifier the spectral bandwidth is reduced to a FWHM of 12 nm. That is the reason why the pulse duration of the amplified pulses is 80 fs instead of the 60 fs generated by the oscillator. The pulse energy, on the other hand, has increased by a factor of about 10^6 to 1 mJ, whereas the repetition rate has decreased to 1 kHz.

For the shorter sub 30 fs laser pulses, which are used in the quantum control of the potassium dimer (see Chapter 5), a commercial multipass amplifier system from FemtoLasers is used. In order to achieve the shorter pulse duration a few technical improvements are employed. First the oscillator is not pumped by an

argon ion laser, but a diode pumped solid state laser, and uses chirped mirrors [77] instead of prisms for intracavity dispersion compensation. The better dispersion compensation of these mirrors results in sub-10-fs laser pulses from the oscillator. Because of the larger spectral bandwidth of the laser pulses the stretcher setup can be extremely simplified. Material dispersion of a 5 cm glass block and about ten passes over third order chirped mirrors provides sufficient temporal stretching. For amplification a multipass amplifier is used instead of a regenerative one since these cause less gain narrowing [79]. The compressor is built with prisms instead of gratings because they offer higher throughput.

3.1.2 Mathematical Description

Along with the experimental realization of femtosecond laser pulses comes the need to give an accurate mathematical description [80] of these laser pulses. The electric field of these pulses can either be specified in the time or in the frequency domain, with the Fourier transformation relating both descriptions.

$$E(t) = \frac{1}{\sqrt{2\pi}} \int_{-\infty}^{\infty} E(\omega) e^{i\omega t} d\omega. \quad (3.1)$$

$$E(\omega) = \frac{1}{\sqrt{2\pi}} \int_{-\infty}^{\infty} E(t) e^{-i\omega t} dt, \quad (3.2)$$

Since $E(t)$ is real, $E(\omega)$ obeys the symmetry $E(\omega) = E^*(-\omega)$, where $*$ denotes complex conjugation. Therefore, a reduced description is sufficient to fully characterize the light field. Only the positive frequency part of $E(\omega)$ is used.

$$E^+(\omega) = \begin{cases} E(\omega) & \text{if } \omega \geq 0, \\ 0 & \text{if } \omega < 0, \end{cases} \quad (3.3)$$

By inverse Fourier transformation one obtains the associated description in the time domain $E^+(t)$, which is now complex valued. So the descriptions in both time and frequency space can be unambiguously separated in a real amplitude part and a phase term.

$$E^+(t) = A(t) e^{i\Phi(t)} \quad (3.4)$$

$$E^+(\omega) = A(\omega) e^{-i\Phi(\omega)} \quad (3.5)$$

It is the manipulation of the spectral phase function $\Phi(\omega)$ that allows to shape the electric field of laser pulses on a femtosecond time scale. This will be shown

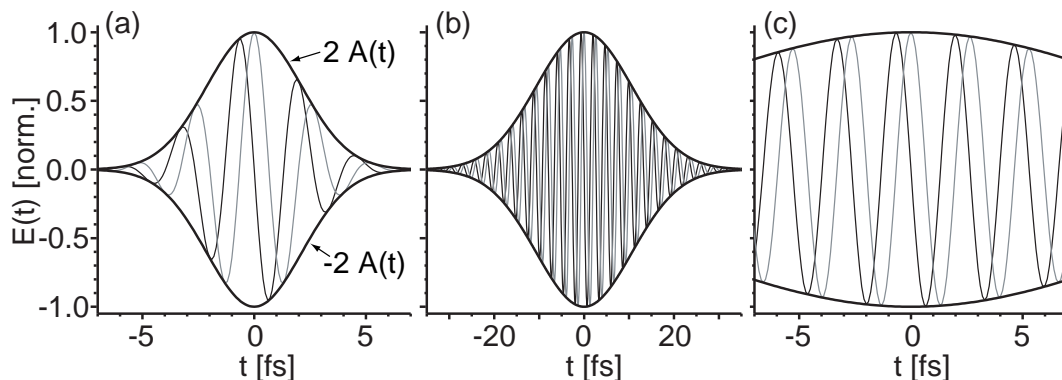


Figure 3.3: Absolute phase of femtosecond laser pulses. An unchirped laser pulse of duration 5 fs (a) is shown with two different values of absolute phase a_0 , displaying a “cosine pulse” $a_0 = 0$ (gray line) and a “sine pulse” $a_0 = \pi/2$ (black oscillating line). The temporal envelope function is identical in both cases. Same plots for an unchirped laser pulse of duration 25 fs (b) and (c). As can be seen in (c) the difference in the electric field is negligible for the two values of the absolute phase for 25 fs laser pulses as compared to the significant changes in (a) for 5 fs laser pulses.

in detail in the next section, but already from Eq. (3.1) it can be seen how manipulation in the frequency domain leads to shaping in the time domain. To better understand the action of the phase function, it is helpful to expand it into a Taylor series around $t = 0$ or respectively around the carrier frequency ω_0 .

$$\Phi(t) = \sum_{j=0}^{\infty} \frac{a_j}{j!} t^j = \sum_{j=0}^{\infty} \frac{1}{j!} \left. \frac{d^j \Phi(t)}{dt^j} \right|_{t=0} t^j \quad (3.6)$$

$$\Phi(\omega) = \sum_{j=0}^{\infty} \frac{b_j}{j!} (\omega - \omega_0)^j = \sum_{j=0}^{\infty} \frac{1}{j!} \left. \frac{d^j \Phi(\omega)}{d\omega^j} \right|_{\omega=\omega_0} (\omega - \omega_0)^j \quad (3.7)$$

In this Taylor series $b_j = d^j \Phi(\omega)/d\omega^j|_{\omega=\omega_0}$ denotes the spectral phase coefficients of j th order and $a_j = d^j \Phi(t)/dt^j|_{t=0}$ denotes the temporal phase coefficients. The zeroth order coefficients in both cases describe a constant phase. Its action can be understood easiest in the time domain, where a_0 is called absolute phase or carrier–envelope phase. It describes the temporal relation of the pulse envelope $A(t)$ with respect to the underlying carrier oscillation. The effect of the absolute phase on the electric field of a femtosecond laser pulse is shown in Fig. 3.3 for the case of a 5 fs and 25 fs laser pulse. As can be seen in Fig. 3.3 the absolute phase usually only becomes important for pulse durations below 10 fs. In addition, it is not stable in conventional femtosecond laser systems and changes from pulse to pulse. There exists also the additional difficulty that most pulse characterization methods (Section 3.3) are not sensitive to it. For the experiments in this thesis, however, it is not important due to the longer pulse durations which are used.

The first order spectral phase coefficient denotes a temporal translation of the laser pulse and all higher order terms changes of the temporal shape. The first order temporal phase coefficient, on the other hand, is the carrier frequency ω_0 . If the spectral width $\delta\omega$ is small compared to this carrier frequency, the fast oscillating term of the spectral phase is often split off to yield

$$\varphi(t) = \Phi(t) - \omega_0 t. \quad (3.8)$$

This condition can also be stated in the time domain, where it implies that the variation of $A(t)$ is small within one optical cycle of the carrier frequency. In this case Equation (3.8) and (3.4) can be combined to

$$E^+(t) = A(t)e^{i\varphi(t)} \cdot e^{i\omega_0 t}, \quad (3.9)$$

where $A(t)e^{i\varphi(t)}$ is called the complex envelope function. This separation (3.9) into the quickly oscillating term $e^{i\omega_0 t}$ and the complex envelope function is often used to simplify calculations of the temporal evolution and spatial propagation of the laser pulse. The factoring out of the quickly oscillating term in these calculations is called the slowly varying envelope approximation (SVEA) [80].

Another quantity that is often used to describe femtosecond laser pulses in the time domain is the momentary or instantaneous light frequency $\omega(t)$

$$\omega(t) = \frac{d\Phi(t)}{dt} = \omega_0 + \frac{d\varphi(t)}{dt}. \quad (3.10)$$

Laser pulses for which this is constant in time are called unchirped. If the momentary frequency increases (or decreases) with time, they are termed up-(down-)chirped. The special case where the frequency changes linearly with time, i.e. $d\omega(t)/dt = d^2\varphi(t)/dt^2 = a_2 = \text{const}$, is called linear chirp.

To regain the real valued electric field $E(t)$ from the reduced notation $E^+(t)$ the following equation is helpful

$$\begin{aligned} E(t) &= 2 \operatorname{Re} E^+(t) \\ &= 2A(t) \cos[\omega_0 t + \varphi(t)]. \end{aligned} \quad (3.11)$$

The temporal intensity is calculated from the electric field by averaging $E^2(t)$ over one oscillation period T

$$I(t) = \varepsilon_0 c n \frac{1}{T} \int_{t-T/2}^{t+T/2} E^2(t') dt' \quad (3.12)$$

$$= 2\varepsilon_0 c n A^2(t), \quad (3.13)$$

where the equivalence between the first and the second line is only true as long as the slowly varying envelope approximation is valid. The spectral intensity, which is more directly accessible in an experiment, is defined by analogy

$$I(\omega) = 2\varepsilon_0 c n A^2(\omega). \quad (3.14)$$

The pulse duration τ_p and the spectral bandwidth $\Delta\omega$ are customarily defined as the full width half maximum (FWHM) of the respective intensity functions

$$\tau_p = \text{FWHM}\{I(t)\}, \quad (3.15)$$

$$\Delta\omega = \text{FWHM}\{I(\omega)\}. \quad (3.16)$$

Obviously, this is only meaningful if these distributions have well defined, smooth shapes, e.g. gaussian or sech^2 distributions. The product of the two FWHMs is called the time–bandwidth product and has a lower limit on the order of one. The exact value of this limit depends on the exact shape of the intensity distributions. The time–bandwidth product is often given for linear frequencies $f = \frac{\omega}{2\pi}$ instead of angular ones ω . For the case of linear frequencies the lower limit has a value of $4 \ln 2 / (2\pi) = 0.441$ for gaussian distributions and 0.315 for sech^2 distributions. A pulse that exactly fulfills that lower limit is called bandwidth limited. In other words, for a given spectral width, there exists a minimal pulse duration, which can only be reached if the laser pulse has the optimal spectral phase $\Phi(\omega)$. For gaussian spectral distributions this phase is constant over ω . However, for a general spectral distribution, finding the optimal phase is a nontrivial problem. The following section deals with the problem, how to shape the spectral phase experimentally.

3.2 Femtosecond Pulse Shaping

Since direct shaping in time is limited to the nanosecond regime because of the maximum speed of electronic light modulation devices (e.g. Pockels cells), for femtosecond laser pulses one needs to employ frequency–domain pulse shaping. The action in the time domain for a given modulation in the frequency domain is described by equation (3.1). The most commonly used devices for frequency–domain pulse shaping are liquid–crystal displays (LCD), acousto–optic modulators (AOM) and deformable mirrors. In this work, only LCDs have been used and the description of femtosecond pulse shapers here is therefore limited to LCDs.

3.2.1 Phase–only Pulse Shaping

Frequency domain pulse shaping has been developed by Weiner and coworkers [81, 82] and refined by Nelson and coworkers [83, 84]. For a review of this field, see reference [85]. The setup used here for phase–only shaping has been described in detail in the diploma thesis of Brixner [86] and elsewhere [32, 87, 88]. A schematic of the setup is shown in Fig. 3.4. Basically, it consists of a zero dispersion compressor [89] in a $4f$ -geometry, which spatially disperses the different frequency components, focuses them into the Fourier plane and recollimates them without introducing any additional phase. In other words, the femtosecond laser pulses leave the zero–dispersion compressor with the same temporal

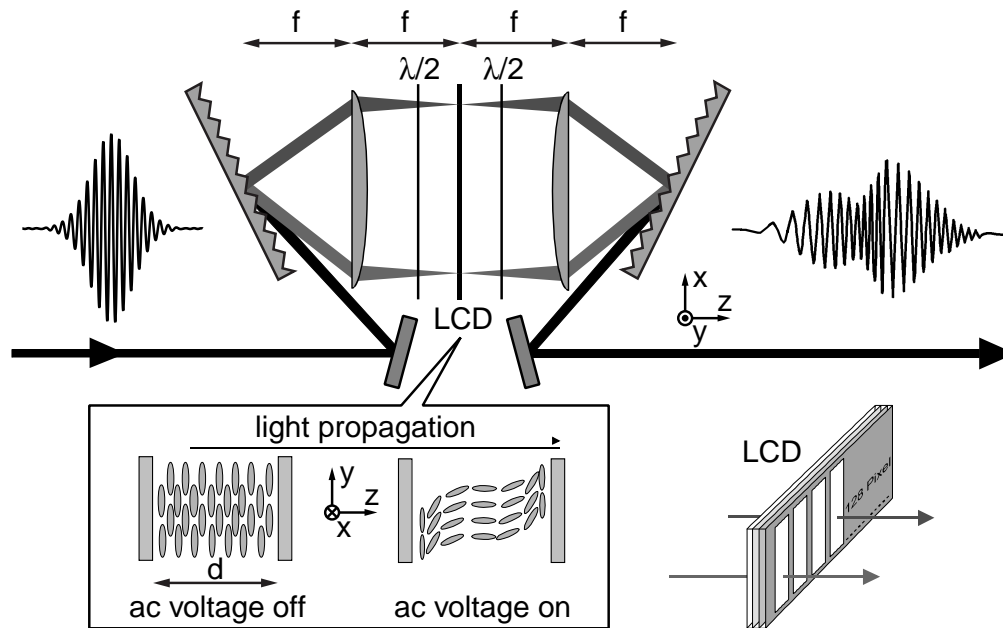


Figure 3.4: Femtosecond pulse shaper. A zero-dispersion compressor is used to spatially disperse the spectral components of a laser pulse. In the Fourier plane of the setup a LCD is placed, at whose 128 pixels the index of refraction can be individually modified. The change of the refractive index is achieved by different orientations of liquid crystal molecules.

profile with which they have entered it. The setup consists of a pair of optical gratings (1800 *lines/mm*) and 2 cylindrical lenses ($f = 80 \text{ mm}$), all spaced one focal length apart. After passing the first grating and lens, all frequency components of $E^+(\omega)$ travel parallel to the z -axis and are focused onto a line with a waist of $30 \mu\text{m}$. At this position, the so-called Fourier plane, maximum frequency resolution (i.e spatial separation of the different frequency components) is achieved. In order to shape the temporal profile a spatial light modulator is inserted into the Fourier plane of the optical setup. A spatial light modulator is by definition able to change the phase, amplitude and/or polarization of light separately at different positions. For this work, a liquid-crystal display (LCD) is used, which can change the polarization and/or phase of the incoming light depending on the orientation of the liquid crystal molecules with respect to the incoming linear light polarization. The change in orientation of these molecules is achieved via dynamic alignment by AC electric fields (square wave; amplitude: 0-10 V; frequency 500 Hz). These AC fields are applied to transparent indium tin oxide (ITO) electrodes, which are patterned into 128 electrodes each $97 \mu\text{m}$ wide, spaced $3 \mu\text{m}$ apart along the x axis. These electrodes are only 2 mm high in the y direction due to technical limitations on the maximum achievable uniformity. Because of that the beam size of the laser needs to be adjusted with a galilean

telescope from ≈ 10 mm to fit the pixel height. Each of those electrodes can be addressed separately and the liquid crystal molecules then tilt in the $y - z$ plane according to the applied amplitude of the AC square wave. A sketch of the orientation change is shown in the lower left inset in Fig. 3.4.

As a consequence of this reorientation the projected electric dipole moment of the molecules changes along the y axis, while it is left unchanged along the x axis. This in turn affects the dielectric tensor ε , which governs the direction-dependent index of refraction n of the medium. By applying the correct voltage U it is therefore possible to deliberately change the refractive index $n_y(U)$. If the light polarization direction is pointing along the y axis, an additional phase $\Delta\Phi(U)$ can be added to the spectral phase of the incoming laser pulse.

$$\Delta\Phi(U) = \frac{[n_y(U) - n_y(0)] \omega d}{c} \quad (3.17)$$

Since a different voltage can be applied to each of the 128 pixels, different additional phases can be added to the frequency components spaced along the x axis. But in order to calculate $\Delta\Phi(\omega, U)$, one needs to map the different frequency components onto the position x and the pixel on which they fall. Also, it is necessary to experimentally calibrate the added phase as a function of U . Both can be done by two calibration measurements, described in detail in Ref. [86]. In this procedure, it must also be taken into account that an individual frequency component has a finite size in the Fourier plane. Hence the mask function of the LCD, i.e. its pixel pattern, must be convoluted with the beam waist of an individual frequency component ω . This leads to a smoothing of the step-like modulations introduced by the pixelated LCD.

As the liquid crystal molecules are birefringent, modulation of only the spectral phase can be achieved as shown above, if the incoming light is polarized along the extraordinary direction. For any other orientation, the light polarization state will change. This can be transferred to an amplitude modulation by inserting a polarizer after the LCD. If two layers of liquid crystal molecules with different preferential orientation are used, phase and amplitude can be shaped simultaneously. Furthermore, such a device can be employed to gain control over the time-dependent polarization profile of ultrashort laser pulses as will be shown in detail in Chapter 4.

Now the limitations of LCD-based pulse shaping will be discussed briefly. Most noticeable are the effects due to the pixelation of the spatial light modulators. With the help of the Fourier transformation (Eq. (3.4)) it can be shown that the step-like nature of the phase function $\Phi(\omega)$ leads to pre- and postpulses, although at lower intensity than the corresponding main pulse [82, 84]. The pre-/postpulses have a time profile identical to that of the main pulse and are spaced $2\pi/\delta\omega = 4$ ps apart from it in time, where $\delta\omega$ is the frequency interval that falls on one pixel. These 4 ps give the time window in which the laser pulse can be shaped without needing to take interference effects with the pre-/postpulses into

account. This time window can of course be increased by the use of LCDs with a larger number of pixels [90]. Another limitation also arises from the Fourier relation between time and frequency domain. It implies that for a given spectral bandwidth there exists a limit for the shortest possible temporal features. For a pulse shaper, this means that in the shaped output laser pulse the fastest change in the temporal profile is on the order of the duration of a bandwidth limited input pulse. The last physically caused limitation is that the temporal shaping is also coupled to spatial effects. These spatio-temporal effects [91, 92] cannot be understood within the scope of the discussion given above. A more thorough theoretical treatment like space-time wigner functions [91] would be needed. In essence, the effects are caused by the spatially structured LCD phase pattern, which can diffract individual frequencies ω to different degrees. After recollimation this leads to different pulse shape across the transverse beam profile. This effect can be minimized by reducing the beam sizes of individual frequency components in the Fourier plane below the size of a pixel. This condition being fulfilled here, the effects are negligible for the experiments presented in this work. A limitation on a more technical level is the response time of LCD, which stems from the fact that it takes the liquid crystal molecules some time (on the order of 100 ms) to align to the AC field. Nevertheless, this waiting time accounts for a notable fraction of the duration of a typical adaptive femtosecond pulse shaping experiment. Therefore, this sets higher requirements for the long term stability of the laser system in order to successfully accomplish such an experiment. Another technical limitation is the transparency range of LCDs. Only femtosecond laser pulses with wavelengths greater than ≈ 450 nm and smaller than ≈ 1600 nm can be directly shaped by using liquid crystal spatial light modulators. A way to extend the pulse shaping capability into the UV range is presented in the next section.

3.2.2 Frequency-Doubling of Shaped Laser Pulses

Many photochemical reactions are triggered off by UV photons. However, pulse shaping with LCDs or AOMs is not possible in this wavelength region, either due to absorption or respectively due to low diffraction efficiency of acoustic waves below 450 nm. If multiphoton absorption is not feasible or desirable, one has a need for shaped UV laser pulses. Direct shaping with micro mirror arrays [93, 94] is a very attractive possibility, yet such devices are currently not commercially available. Other spatial light modulators which are capable of operating in the UV, like deformable mirrors [95] or an array of fused-silica plates [96], are only able to produce “simple”, smooth pulse shapes or their mechanical setup is too complicated and large. However, for chemical reaction control, often quite complex pulse shapes are necessary. Therefore, nonlinear frequency conversion of shaped NIR or VIS laser pulses is the only option for shaped UV-pulses.

The simplest way to achieve this is frequency doubling of shaped laser pulses

in a suitable nonlinear crystal, i.e. second harmonic generation (SHG). As a result of this nonlinear conversion step, the transfer of the pulse shape from the NIR to the UV is not straightforward. Especially, the question arises what the frequency-doubled shaped pulse looks like. For simple pulse shapes this has been extensively investigated by Sidick *et al.* [97, 98] both theoretically and experimentally. The case of sinusoidal spectral phase modulation of the fundamental laser pulse has also been explored [99]. However, in all of these experiments the phase of the second harmonic was never measured and only auto- or cross-correlation measurements (see next section) were performed. On the other hand, the nonlinear interaction in the SHG crystal leads to a coupling of phase and amplitude. Therefore, the second harmonic pulses are shaped in phase and in amplitude, even if phase-only pulse shaping is used on the fundamental laser pulse. The nonlinear interaction is governed for the case of type-I phase matching by two coupled differential equations [80] for the fundamental (subscript 1) and the second harmonic (subscript 2)

$$\left(\frac{\partial}{\partial z} + \frac{1}{v_1} \frac{\partial}{\partial t} - i \frac{g_1}{2} \frac{\partial^2}{\partial t^2} \right) \tilde{\mathcal{E}}_1 = -i \chi^{(2)} \frac{\omega_1^2}{2c^2 k_1} \tilde{\mathcal{E}}_1^* \tilde{\mathcal{E}}_2 e^{i\Delta k z} \quad (3.18)$$

$$\left(\frac{\partial}{\partial z} + \frac{1}{v_2} \frac{\partial}{\partial t} - i \frac{g_2}{2} \frac{\partial^2}{\partial t^2} \right) \tilde{\mathcal{E}}_2 = -i \chi^{(2)} \frac{\omega_2^2}{4c^2 k_2} \tilde{\mathcal{E}}_1^2 e^{i\Delta k z}. \quad (3.19)$$

Here $v_i = d\omega/dk|_{\omega_i}$ is the group velocity, $g_i = [(dk/d\omega)^2/k + (d^2k/d\omega^2)]|_{\omega_i}$ the group velocity dispersion coefficient, $\Delta k = 2k_1 - k_2$ the wave vector or phase mismatch and $\chi^{(2)}$ the nonlinear optical susceptibility of second order. For simplification of notation the differential equation is stated using the complex envelope function $\tilde{\mathcal{E}}_i = 2A_i(t) \cdot e^{i\phi_i(t)}$, which is only reasonable under the SVEA. For the thin crystals used in this work the following simplifications can be made. In a thin crystal and for moderate conversion efficiency no pump depletion occurs, i.e. the fundamental E_1^+ does not depend on z . All group velocity dispersion effects are negligible and can be ignored. This implies in particular for the differential equation system (3.19) that the term in front of the second partial derivative with respect to time vanishes. For efficient SHG it is essential to cancel the wave vector mismatch, i.e. $\Delta k = 0$. This condition for the wave vectors can be rewritten in terms of the refractive index $n(\omega_1) = n(\omega_2 = 2\omega_1)$. It can be fulfilled, for example, by using birefringent crystals, where the fundamental is polarized as the ordinary wave and the second harmonic as the extraordinary wave $n_o(\omega_1) = n_{eo}(2\omega_1)$. Thus, the wave vector mismatch cancels out and the fundamental and second harmonic are phase matched. Despite the phase matching, the group velocities may still differ, since they depend on the derivative of the refractive indices with respect to ω . This causes the SHG bandwidth to shrink as the SHG efficiency for all but the central frequencies decreases. For crystals which are thin enough,

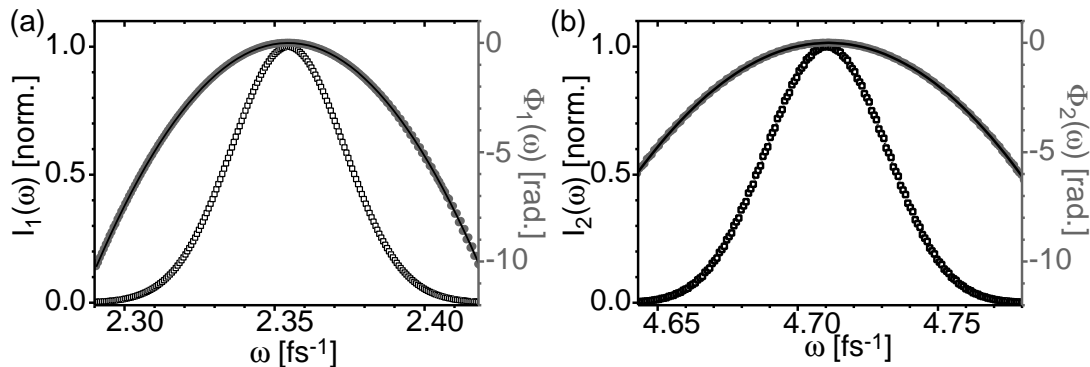


Figure 3.5: SHG with shaped laser pulses. The fundamental laser pulse (a) has a quadratic spectral phase with a Taylor coefficient $b_{2,FP} = -5000 \text{ fs}^2$. After SHG in a $400 \mu\text{m}$ thick BBO crystal this results in a 400 nm laser pulse (b) with a quadratic spectral phase of $b_{2,SH} = -2500 \text{ fs}^2$. The respective quadratic fit to the spectral phase is shown as a black line.

this effect can be neglected and Eq. (3.19) reduces to

$$E_2^+(\omega) \propto \int E_1^+(\Omega) E_1^+(\omega - \Omega) d\Omega, \quad (3.20)$$

i.e. for the complex field envelopes $\tilde{\mathcal{E}}$ in the time domain

$$\tilde{\mathcal{E}}_2(t) \propto \left(\tilde{\mathcal{E}}_1(t) \right)^2. \quad (3.21)$$

So for thin crystals the temporal profile almost retains its shape apart from squaring of the temporal amplitudes. As Eq. (3.20) is a convolution integral, the effects in the frequency domain are more complicated and a mixing of frequency components occurs. Therefore, both spectral phase and amplitude of the second harmonic are influenced by a modulated spectral phase of the fundamental. Since femtosecond pulse shapers act on the spectral phase, as discussed in the previous section, it is helpful to calculate the action of a certain spectral phase of the fundamental on the second harmonic pulse shape. The convolution integral (3.20) can be solved analytically only for a few special cases like gaussian spectral amplitude distribution with quadratic spectral phase. For the following discussion a gaussian shaped spectrum of the fundamental will always be considered with different spectral phases. In the case where no analytical solution exists, the differential equation is solved numerically. The effects of slightly different group velocities in this case is fully taken into account when performing the calculations.

It can be shown analytically [33, 98] for quadratic spectral phase of the fundamental that the spectrum of the second harmonic remains the same as with a bandwidth-limited fundamental laser pulse, only at reduced efficiency. The second harmonic laser pulse also has a quadratic spectral phase with its Taylor

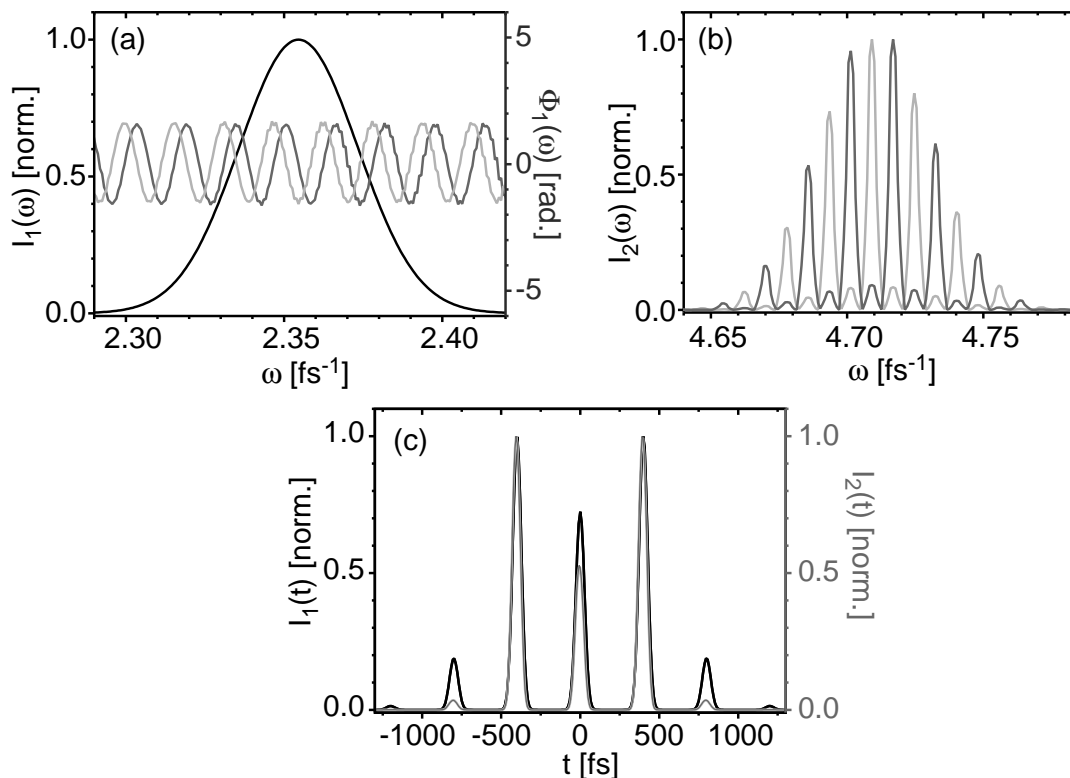


Figure 3.6: SHG with sinusoidally phase-shaped laser pulses. The fundamental laser pulse (a) has a spectral phase with a sine (light gray) or cosine (dark gray) like shape. Both phase functions result in the same temporal profile $I(t)$ (c, black line), although with different temporal phase (not shown). The temporal profile of the second harmonic (c, gray line) is also identical for both cases. The spectrum at 400 nm (b), however, is different for the sine (light gray) or cosine (dark gray) case.

coefficient (see Eq. (3.7)) $b_{2,SH}$ being $b_{2,FP}/2$ of the fundamental. To illustrate this further a numerical example is shown in Fig. 3.5. The quadratic spectral phase of the fundamental, in this example $b_{2,FP} = -5000$ fs², is transferred to the second harmonic, but the 400 nm laser pulse has only a spectral phase with a Taylor coefficient $b_{2,SH} = -2500$ fs². The spectrum of the second harmonic, on the other hand, is not affected by the quadratic spectral phase of the fundamental laser pulse. This can be seen when comparing the spectrum from Fig. 3.5b to the second harmonic spectrum of a bandwidth limited 800 nm laser pulse (light gray line in Fig. 3.7).

Another case that is analytically solvable [99] is sinusoidally modulated spectral phase, which corresponds to a pulse train in the time domain. For large enough temporal separation, i.e. a sinusoidal phase with large enough modulation frequency, the second harmonic is also a pulse train due to Eq. (3.21). Interestingly, almost no spectral phase modulation of the second harmonic is present, but the spectrum is periodically modulated (with contrast down to zero amplitude

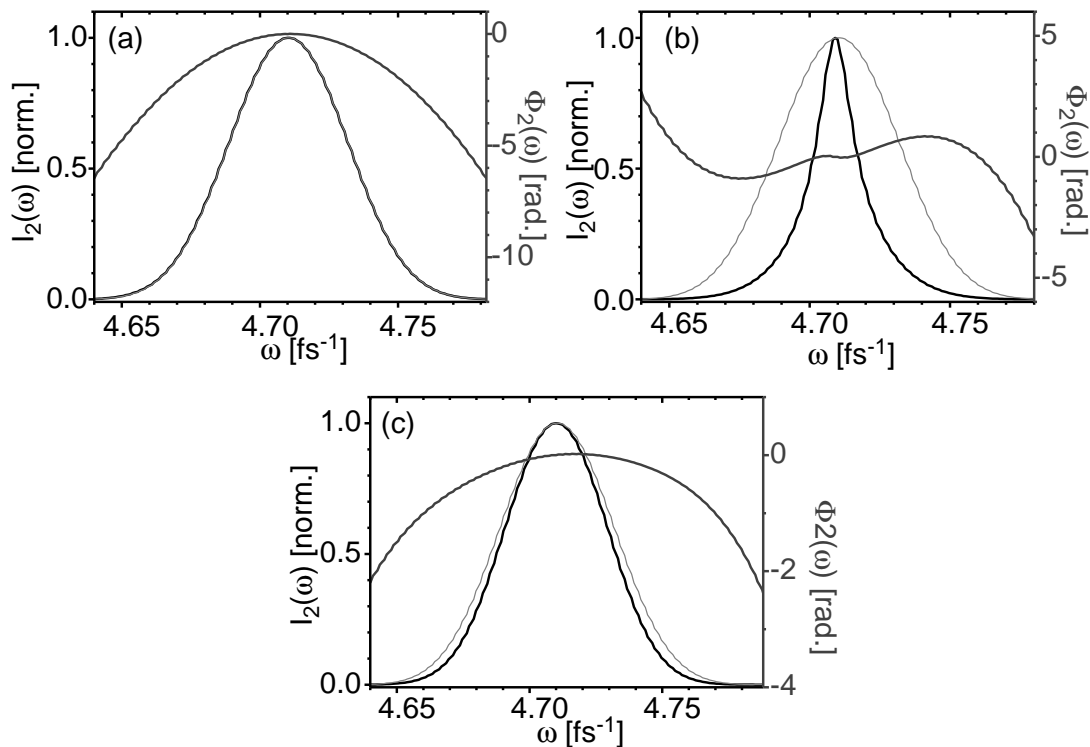


Figure 3.7: SHG with differently phase-shaped laser pulses. Whereas quadratic spectral phase ($b_{2,FP} = -5000 \text{ fs}^2$) of the fundamental (a) leaves the second harmonic spectrum identical to that of a bandwidth-limited laser pulse (light gray line, shown for comparison in all three cases), cubic phase ($b_{3,FP} = 5 \cdot 10^5 \text{ fs}^3$) modulation (b) causes dominantly a spectral narrowing. Fourth order ($b_{4,FP} = 1 \cdot 10^7 \text{ fs}^4$) spectral phase modulation (c), on the other hand, produces almost the same spectrum as a unshaped 800 nm laser.

in between) to yield the pulse train in the second harmonic. So this case is very similar to the situation present in spectral interferometry (SI) measurements (see Section 3.3.2). An example of sinusoidally modulated phase is shown in Fig. 3.6. In this case the action of frequency-doubling is very simple to understand in the time domain, where the pulse train in the fundamental retains its temporal shape almost completely asides from squaring of the amplitudes. However, the spectrum at 400 nm is very different from the bandwidth-limited case. As can be seen in Fig. 3.6b, the pulse train at 400 nm is produced by spectral amplitude modulation. In contrast to the fundamental, the second harmonic has almost no spectral phase modulation. This example illustrates, even though the picture in the time domain is quite simple, that this must not be the case in the frequency domain.

Most other cases can only be solved numerically, unless it is possible to use the mathematical technique of quadratic completion. For cubic spectral phase the dominant effect is a spectral narrowing of the second harmonic and only odd

orders of spectral phase are present. Fourth order spectral phase, on the other hand, produces only negligible deformations of the spectral amplitudes and the dominant action is only even-order spectral phases. An overview of the action of different polynomial orders of spectral phase modulation on the resulting second harmonic pulse shape is given in Fig. 3.7. Here the case of quadratic (Fig. 3.7a), cubic (Fig. 3.7b) and fourth order spectral phase modulation of the fundamental laser pulse is shown.

In conclusion, one can say that it is possible to understand the nonlinear conversion of the pulse shape and calculate the resulting second harmonic pulse for the case of thin crystals, although the relationship between incident phase-only shaped fundamental and resulting second harmonic is nontrivial. The numeric calculations of arbitrary phase-shaped fundamental laser pulses require very precise knowledge of the pulse shape. Even small deviations in the spectral phase can lead to quite different calculated second harmonic pulses. It is therefore advantageous to directly characterize the shaped second harmonic since the uncertainties in the numeric results are large for anything but very smooth spectral phases of the fundamental. That is the reason why experimental methods to characterize both the fundamental and the second harmonic are introduced in the next section.

3.3 Laser Pulse Characterization

The ability to almost arbitrarily shape femtosecond laser pulses causes the necessity to accurately characterize them. Yet, the problem that one faces is the following: in order to measure a short event in time one usually employs an even shorter event to measure it. As femtosecond laser pulses are one of the “shortest man-made events” [100] no shorter gate event is available to characterize them. Therefore, one uses the pulse itself (or other femtosecond laser pulses) to fully characterize the laser pulse in phase and amplitude.

3.3.1 FROG and XFROG

As the laser pulse itself is used for the measurement, all frequency-resolved optical gating (FROG) measurements are in essence correlation measurements. The setup for an autocorrelation measurement is shown in Fig. 3.8a. The laser pulse is split into two copies in a Mach-Zehnder type interferometer. One arm of the interferometer is used to introduce a variable time delay. The two copies of the laser pulse are then recombined, either collinear (not shown in figure) or non-collinear, and focused into a nonlinear optical crystal or a nonlinear optical detector, e.g. a 2-photon diode. The spectrally integrated signal $I(\tau)$ is given by

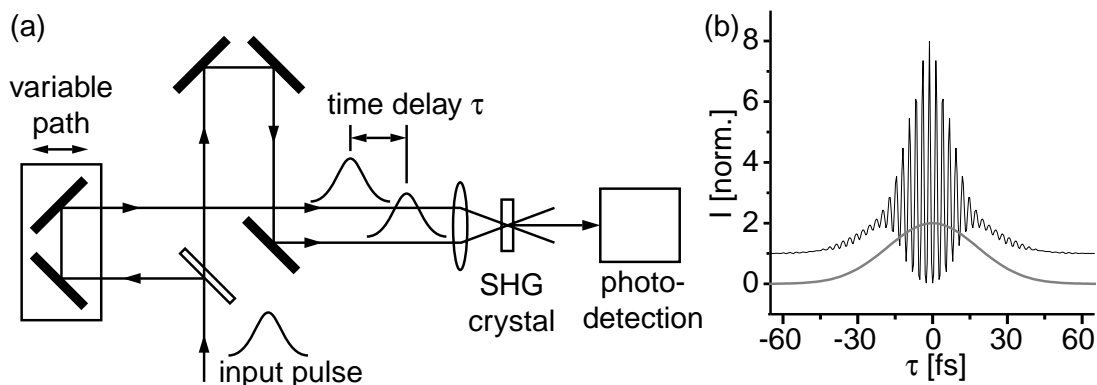


Figure 3.8: Autocorrelation measurement of femtosecond laser pulses. The schematic setup of a non-collinear autocorrelator (a) utilizing a SHG-crystal is shown together with the autocorrelation signal (b) for the non-collinear (gray) and collinear (black) case.

$$I(\tau) = \int_{-\infty}^{\infty} [E(t) + E(t - \tau)]^4 dt \quad (3.22)$$

for the collinear case, which is often called interferometric autocorrelation, and by

$$I(\tau) = \int_{-\infty}^{\infty} I(t)I(t - \tau) dt \quad (3.23)$$

for the non-collinear case, often called intensity autocorrelation. In order to resolve the fringes in the graph of the interferometric autocorrelation much shorter pulses than during the experiments are used for the simulation with Lab2 [101] of the signals in Fig. 3.8b. The laser pulse which was used has a spectral width FWHM = 127 nm at a center wavelength of 800 nm, which corresponds to a bandwidth limited pulse duration of 7.5 fs. As can be seen from the vanishing of the fringes at the outer regions, the pulse is chirped and the duration increases to 30 fs. This corresponds to a spectral phase coefficient $b_2 = 77.7 \text{ fs}^2$.

Since only the non-collinear setup is employed for all experiments in this work, the further discussion is restricted to this case. The intensity autocorrelation can be used to quickly determine the approximate pulse duration and to get an indication of the underlying pulse shape. In principle, it is possible to extract the complete information about the electric field from an autocorrelation measurement [102–104] together with an independently measured spectrum. However, it requires ultra low noise measurements with very high dynamic range in order for the iterative retrieval algorithm to give accurate results. Furthermore, it tends to yield shorter pulse durations than actually present and has only been tested

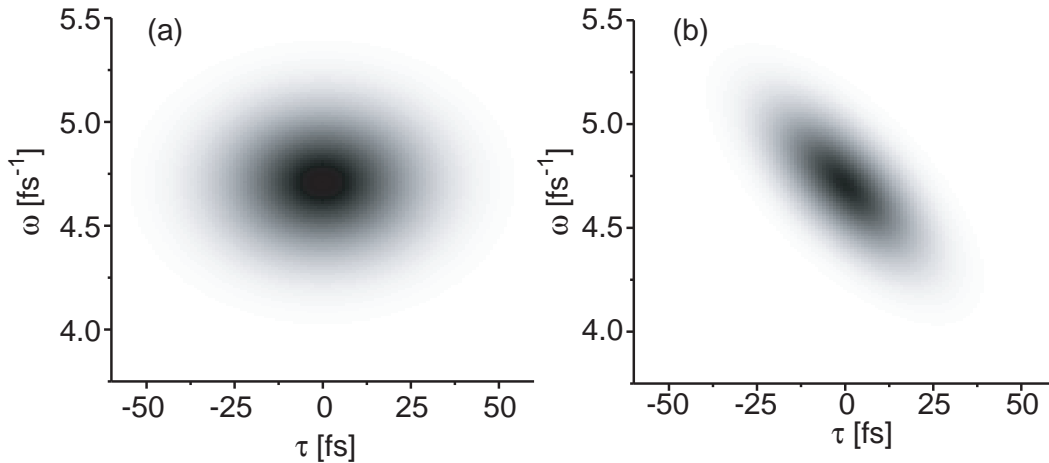


Figure 3.9: FROG and XFROG traces of femtosecond laser pulses. The FROG trace of the linearly chirped laser pulse of Fig. 3.8 is shown in (a) and the corresponding XFROG trace of this pulse with an unchirped 7.5 fs laser pulse in (b). It should be noted that the FROG trace of a bandwidth–limited laser pulse has the same shape (but with a different scale) as the one of a linearly chirped laser pulse due to the time delay reversal symmetry of FROG. This symmetry is not present in the case of XFROG.

on rather simply chirped pulses. Also the iterative algorithm used to retrieve the spectral phase from the autocorrelation measurement does not converge for all pulse shapes and in these cases it gives ambiguous results. For arbitrarily shaped laser pulses this method is not sufficient and it is advantageous to use a spectrometer to record the signal (3.23) spectrally resolved. This technique has been called frequency–resolved optical gating (FROG). It was first introduced by Trebino and coworkers [105, 106], who give an extensive review in Ref. [107]. The method has also been extended to spectrally resolved crosscorrelation measurements (XFROG) [108, 109]. There, the unknown laser pulse is combined with a known reference pulse in the nonlinear optical crystal. XFROG is useful to measure extremely weak pulses [110] or laser pulses at a central wavelength where there are no SHG crystals available. It is for example employed to characterize shaped 400 nm laser pulses. In Fig. 3.9 a simulation of the measured signal, often called FROG trace, is shown for the FROG (a) and XFROG (b) method. They both correspond to the linearly chirped laser pulse from Fig. 3.8. The fact that the FROG trace is symmetric with respect to delay although the underlying laser pulse is not, indicates the difficulties to get from the trace to the complete pulse characterization. The XFROG trace might be somewhat easier to interpret for the case of a very short, bandwidth–limited reference pulse. But, if the reference pulse has a pulse duration on the same order as the unknown laser pulse and shows some structure itself, the XFROG trace becomes even harder to interpret. Therefore, an exact mathematical treatment is needed to derive the pulse shape

from the measured signal. However, this is not an analytically solvable problem and an iterative algorithm must be used to retrieve the electric field. The procedure will be outlined briefly for the FROG case with a SHG crystal. The method for XFROG is similar and will not be shown here explicitly. The FROG trace is given by

$$I_{\text{FROG}}(\tau, \omega) = \left| \int_{-\infty}^{\infty} E_{\text{sig}}(\tau, t) e^{-i\omega t} dt \right|^2, \quad (3.24)$$

with the proportionality factors left out for clarity and with the signal field

$$E_{\text{sig}}(\tau, t) = E^+(t)E^+(t - \tau) \quad (3.25)$$

depending only on the electric field $E^+(t)$ of the unknown laser pulse and the time delay τ between the two pulse copies. The goal is now to transform Eq. (3.24) so that it states a two-dimensional phase-recovery problem. For this purpose one defines the Fourier transformation of $E_{\text{sig}}(\tau, t)$ with respect to τ

$$E_{\text{sig}}(\Omega, t) = \frac{1}{\sqrt{2\pi}} \int_{-\infty}^{\infty} E_{\text{sig}}(\tau, t) e^{-i\Omega\tau} d\tau \quad (3.26)$$

and its inverse transformation

$$E_{\text{sig}}(\tau, t) = \frac{1}{\sqrt{2\pi}} \int_{-\infty}^{\infty} E_{\text{sig}}(\Omega, t) e^{i\Omega\tau} d\Omega. \quad (3.27)$$

Then Eq. (3.24) can be rewritten in terms of the two-dimensional Fourier transform of $E_{\text{sig}}(\Omega, t)$ as

$$I_{\text{FROG}}(\tau, \omega) = \frac{1}{2\pi} \left| \int_{-\infty}^{\infty} \int_{-\infty}^{\infty} E_{\text{sig}}(\Omega, t) e^{i\Omega\tau - i\omega t} d\Omega dt \right|^2. \quad (3.28)$$

Since $E_{\text{sig}}(\Omega = 0, t)$

$$E_{\text{sig}}(\Omega = 0, t) = \frac{1}{\sqrt{2\pi}} \int_{-\infty}^{\infty} E_{\text{sig}}(\tau, t) d\tau = E^+(t) \frac{1}{\sqrt{2\pi}} \int_{-\infty}^{\infty} E^+(t - \tau) d\tau \quad (3.29)$$

is directly proportional to $E^+(t)$, which can easily be seen by substituting $\tau \rightarrow t - \tau$ in Eq. (3.29), the only remaining task is to find the phase to the two-dimensional Fourier transform. The two-dimensional phase retrieval problem can — unlike the one-dimensional case — be solved by employing suitable iterative

algorithms [111, 112]. The ambiguities that remain are only trivial. For example, because of the time delay reversal symmetry of $I_{\text{FROG}}(\tau, \omega)$, which was already evident in Fig.3.9, the sign of $\Phi(\omega)$ cannot be ascertained. However, this problem can be resolved by an additional FROG measurement, where the phase of the unknown laser pulse is modified in a known way, e.g. by introducing a certain amount of material dispersion or by means of a pulse shaper. In this work, commercial software (Frog 3.1) from Femtosoft Technologies was used for the FROG and XFROG retrieval process. In spite of the performance of this software the computational effort is still on the order of 20 minutes for a retrieval and, which is even worse, tends to increase even further for complex shaped pulses. Therefore, another pulse characterization technique is introduced in the next section, which does not rely on iterative algorithms.

3.3.2 Spectral Interferometry

The technique of spectral interferometry (SI) [113–115] allows complete characterization of an unknown laser pulse with the help of a well-known reference pulse. Its advantages are the non-iterative data manipulation, very low computational requirements and its ability to give real-time pulse characterization. Requiring only linear optical measurements, it has a very wide dynamic range, i.e. it is capable to measure very short as well as very complex shaped, long pulses without adjustment of the experimental setup. The drawback, however, is the need to characterize the reference pulse separately. If this is done via FROG, the whole method is called TADPOLE (temporal analysis by dispersing a pair of light electric fields) [116] for linearly polarized pulses and POLLIWOG (polarized light interference versus wavelength of only a glint) [117] for arbitrarily polarized laser pulses. The setup is shown in Fig. 3.10 together with a simulated measurement of the same pulse as in Fig. 3.8 and 3.9. During the measurement, the time delay is not varied but left at a fixed delay, so that the two pulses do not overlap temporally. Unlike in the previously introduced methods, the pulse shaper is placed in one arm of the interferometer and not in front of it. The overlap of the shaped and the reference pulse inside the spectrometer results in an interference spectrum. This spectrum is recorded by a high-resolution spectrometer. For the SI to give accurate results the spectrometer must have a very accurate wavelength calibration [118]. The fringe spacing (see Fig. 3.10b) is roughly $(2\pi)/\tau$ and the deviation from these positions is caused by the difference in spectral phase between reference and unknown laser pulse. The interference spectrum is given by

$$I_{\text{SI}}(\omega) = 2\varepsilon_0 c n \left| E_0^+(\omega) + E^+(\omega) e^{-i\omega\tau} \right|^2, \quad (3.30)$$

where the additional phase $e^{-i\omega\tau}$ is due to the delay τ between the shaped pulse $E^+(\omega) = A(\omega)e^{-i\Phi(\omega)}$ and the reference pulse $E_0^+(\omega) = A_0(\omega)e^{-i\Phi_0(\omega)}$. The data

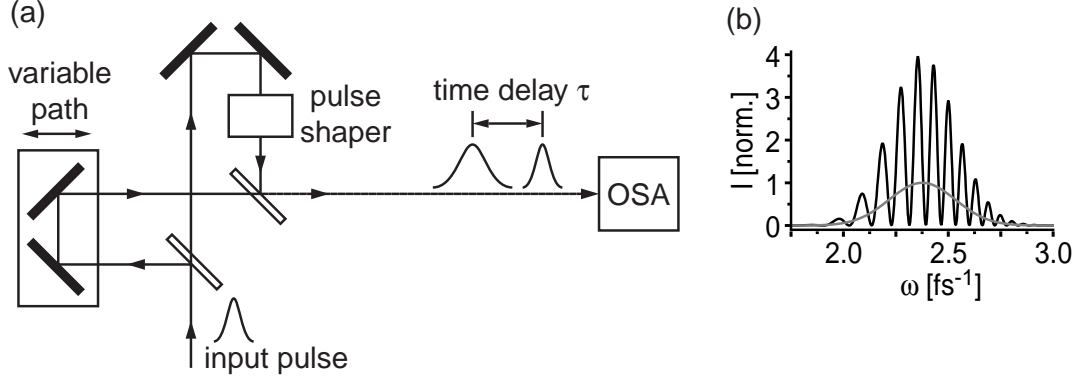


Figure 3.10: Spectral interferometry of femtosecond laser pulses. The schematic setup (a) is shown along with a simulated interference spectrum (black) of the linearly chirped laser pulse from Fig 3.8 and a bandwidth limited 7.5 fs laser pulse at a mutual time delay τ of 80 fs (identical individual spectra of both laser pulses shown in gray).

evaluation is sketched in Fig. 3.11. The necessary mathematical transformations for this data evaluation are briefly outlined next.

In the following discussion, all proportionality constants $2\varepsilon_0cn$ are omitted for the sake of simplicity. Briefly first the individual spectra $I_0(\omega) = A_0(\omega)^2$ and $I(\omega) = A(\omega)^2$ are subtracted from Eq. (3.30). The signal is then

$$S(\omega) = I_{SI}(\omega) - I(\omega) - I_0(\omega) \quad (3.31)$$

$$= [E_0^+(\omega)]^* E^+(\omega) e^{-i\omega\tau} + E_0^+(\omega) [E^+(\omega)]^* e^{i\omega\tau} \quad (3.32)$$

$$= 2\sqrt{I_0(\omega)I(\omega)} \cos[\Phi_0(\omega) - \Phi(\omega) - \omega\tau]. \quad (3.33)$$

In principle, it is possible to obtain the desired information $\Delta\Phi(\omega) = \Phi_0(\omega) - \Phi(\omega)$ directly from Eq. (3.33) with the help of the arccos function. However, it was shown in [115] that the presence of experimental fluctuations affects the results very strongly when using the arccos function. Therefore, a different data analysis is performed. The signal $S(\omega)$ is Fourier transformed into the time domain

$$S(t) = \frac{1}{\sqrt{2\pi}} \int_{-\infty}^{\infty} S(\omega) e^{i\omega t} d\omega \quad (3.34)$$

$$= \frac{1}{\sqrt{2\pi}} \int_{-\infty}^{\infty} [E_0^+(\omega)]^* E^+(\omega) e^{i\omega(t-\tau)} d\omega + \left(\frac{1}{\sqrt{2\pi}} \int_{-\infty}^{\infty} [E_0^+(\omega)]^* E^+(\omega) e^{i\omega(-t-\tau)} d\omega \right)^* \quad (3.35)$$

$$= \tilde{S}(t - \tau) + \tilde{S}^*(-t - \tau). \quad (3.36)$$

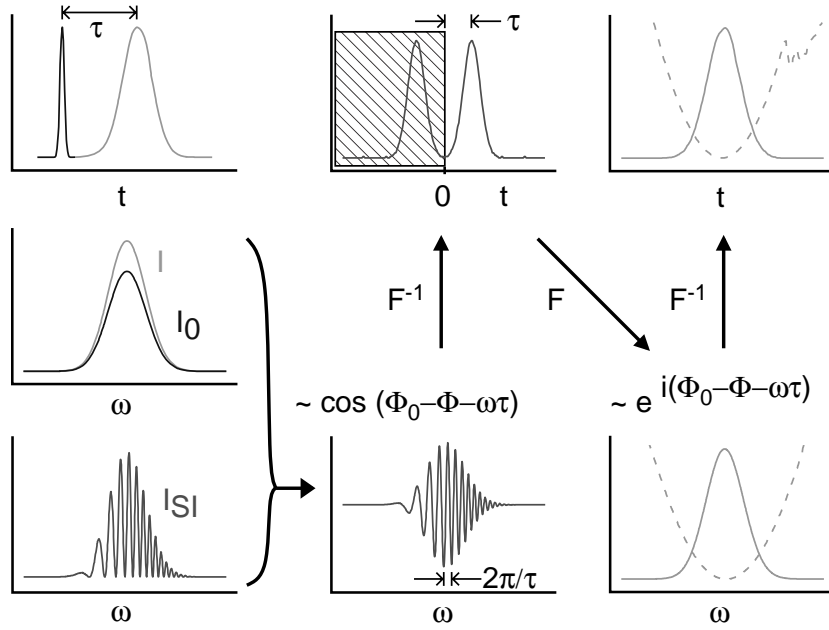


Figure 3.11: Spectral interferometry data evaluation. The diagram shows the data evaluation of the interference spectrum and the two spectra of the shaped and the reference pulse. Here F and F^{-1} denote the Fourier transformation or the inverse Fourier transformation.

Since $S(\omega)$ is real, $S(t)$ obeys the symmetry relation $S(t) = S^*(-t)$. If the pulse separation τ is longer than the individual pulse durations τ_p , it is sufficient to consider only the positive delay part $S^+(t)$ of $S(t)$. Hence, the two contributions of $S(t)$ around time $t \approx \tau$ and $t \approx -\tau$ can be separated from one another. Without loss of generality one assumes $\tau > 0$, then keeping only the positive-delay part amounts to the definition

$$S^+(t) = \tilde{S}(t - \tau). \quad (3.37)$$

The inverse transformation into the frequency domain then yields

$$\begin{aligned} S^+(\omega) &= \frac{1}{\sqrt{2\pi}} \int_{-\infty}^{\infty} \tilde{S}(t - \tau) e^{-i\omega t} dt \\ &= [E_0^+(\omega)]^* E^+(\omega) e^{-i\omega\tau} \\ &= \sqrt{I_0(\omega)I(\omega)} e^{i[\Phi_0(\omega) - \Phi(\omega) - \omega\tau]}. \end{aligned} \quad (3.38)$$

Now the cosine function of Eq. (3.33) is transformed into a complex valued exponential form. The desired information $\Delta\Phi$ can now be obtained by evaluating the argument $\arg[S^+(\omega)]$ of the complex valued quantity $S^+(\omega) = |S^+(\omega)|e^{i\arg[S^+(\omega)]}$. Evaluating the argument (i.e. the phase) of a complex number is much less

sensitive to noise than applying the arccosine function to a real number. This can be easily understood by considering the fact that the cosine function is bounded to the interval $[-1, 1]$ and experimental noise can lead to values of $S(\omega)/(2\sqrt{I_0(\omega)I(\omega)})$ outside that interval.

As the spectrum of the unknown laser pulse is also measured during the SI characterization and the phase of the reference laser pulse is known from a separate FROG measurement, one now has a complete characterization of the unknown laser pulse. That means of its spectral amplitude $A(\omega)$ and phase $\Phi(\omega)$. From this information the time domain representation $E^+(t)$ can be calculated using Eq. (3.1). However, sometimes the pulse representation purely in the time or frequency domain is not very intuitive for understanding “what the pulse looks like”. Because of that a joint time–frequency representation of femtosecond laser pulses is given in the next section.

3.3.3 Joint Time–Frequency Representation

Joint time–frequency representations (JTFR) [119] are useful in many areas of physics, engineering and computer science where complex signal profiles in the time or frequency domain are involved. One example from computer science is speech recognition. If the signal, here speech, is purely considered in the time or frequency domain, the computer recognition can simply be fooled by speaking for example faster or in a higher tonal range. JTFR, on the other hand, allow the computer to recognize the repeating patterns in the signal and thus to understand human speech. In femtosecond laser physics JTFR can aid the intuitive understanding of complex pulse shapes since they can give a picture which frequencies appear at which time during the shaped laser pulse. Of the different JTFR, here only the Wigner and Husimi distribution are used. The Wigner distribution was originally introduced as a phase space representation in quantum mechanics [120]. Both the Wigner and the Husimi representation have been heavily used in quantum optics [121]. The first ones to use these distributions for the representation of ultrashort light pulses were Paye *et al.* [91, 122]. The Wigner distribution of a femtosecond light pulse is given by

$$W(E^+; t, \omega) = \int_{-\infty}^{\infty} E^+(\omega + \Omega) [E^+(\omega - \Omega)]^* e^{i2\Omega t} d\Omega, \quad (3.39)$$

or equivalently by

$$W(E^+; t, \omega) = \int_{-\infty}^{\infty} E^+(t + \tau) [E^+(t - \tau)]^* e^{-i2\omega\tau} d\tau. \quad (3.40)$$

The Wigner distribution is always real valued and bounded, although it may contain negative numbers. Therefore, it cannot be interpreted as a probability

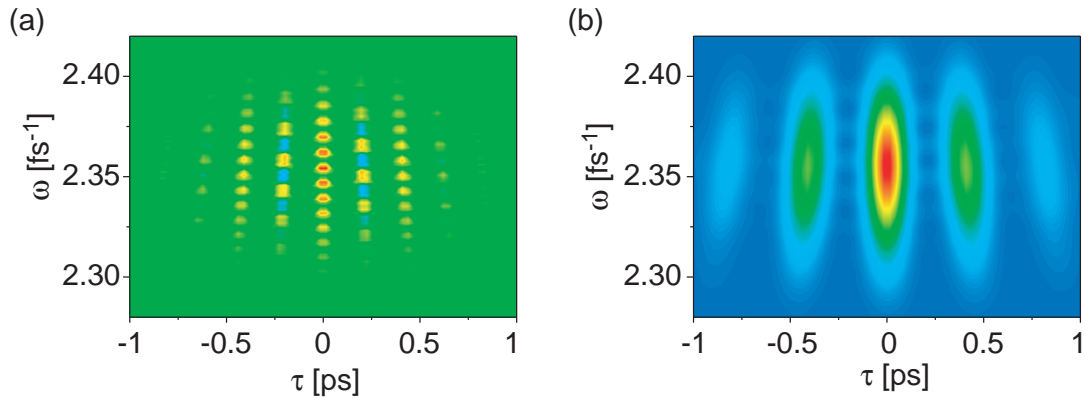


Figure 3.12: Wigner (a) and Husimi (b) representation of ultrashort laser pulses. The laser pulse is a pulse train with a time spacing of 400 fs.

distribution. The reason for this is the Fourier relation between the time and frequency domain (or Heisenberg’s energy–time uncertainty relation), which imposes an upper boundary on the temporal precision of a frequency measurement or vice versa. Fig. 3.12a shows the Wigner representation of a femtosecond pulse train with a temporal spacing between adjacent pulses of 400 fs. The fact that the Wigner distribution shows rapidly oscillating interference terms between two phase-related signals make the interpretation of the plot rather complicated. This can be seen in the plot, for example, at a time delay τ of -200 fs and +200 fs.

The Husimi distribution, on the other hand, fulfills the conditions for a probability interpretation. It can be derived from the Wigner distribution by two-dimensional smoothing that fulfills the minimum uncertainty product condition. If, for example, a convolution with a two-dimensional gaussian is used for smoothing, the two widths of the gaussian must fulfill the relation $\sigma_\tau\sigma_\omega = 4 \ln 2$. From the condition for the two widths it is already obvious, that there exist many Husimi distributions for a given Wigner distribution. In this work the symmetrically smoothed Wigner distribution, i.e. $\sigma_\tau = \sigma_\omega = 2\sqrt{\ln 2}$, is always used for the Husimi distribution.

Now the value of the Husimi distribution can be interpreted as the probability of finding a photon of frequency $\omega \pm \sigma_\omega$ at time $\tau \pm \sigma_\tau$. In Fig. 3.12b the Husimi representation of the same pulse train as in Fig. 3.12a is depicted. The Husimi distribution looks very similar to the corresponding XFROG trace, if a very short, bandwidth-limited reference pulse is used for XFROG. However, there are some differences: the ω -axis on the XFROG trace is the sum frequency of reference and shaped laser pulse, whereas the frequency axis of the Husimi distribution directly shows the frequency of the shaped laser pulse. It is very interesting to note that the interference terms of the Wigner distribution, which do not have a direct physical meaning, have vanished in the Husimi representation. The Wigner representation, on the other hand, has the advantage that the integration over

all delay times τ yields the spectrum of the ultrashort laser pulse. Similarly the integration over all frequencies ω gives the temporal intensity profile $I(t)$. The Husimi distribution, in contrast, does not fulfill these marginal relations.

4 Ultrafast Polarization Shaping

In this chapter the generation, characterization and application of polarization-shaped laser pulses will be presented. Not only the momentary frequency and amplitude can now be changed, but also the ellipticity and orientation of the principal axis. In a sense, the phase-only shaped laser pulses from the previous chapter are leaving “Flatland” and are entering the three-dimensional world. The pulse-shaping setup to generate these laser pulses and the methods necessary to characterize them are discussed in Section 4.1. The influence of optical elements like mirrors or glass plates on the polarization-shaped pulses is analyzed in Section 4.2. Possible compensations for those polarization modulations are also discussed here. In the last Section 4.4 adaptive optimization with polarization shaped laser pulses in an optical demonstration experiment, i.e. SHG in a BBO crystal, is shown.

4.1 Generation and Characterization

In principle, the generation of polarization-shaped femtosecond laser pulses can be achieved by splitting the laser pulse into two orthogonal polarization components within a Mach-Zehnder interferometer. Each of these laser pulses in the two arms can then be manipulated separately. By introducing frequency-dependent phase modulation, e.g. via material dispersion [117], a time-varying polarization state after recombination of the two laser pulses with a suitable time delay can be accomplished. Other possibilities to introduce spectral phase modulations have been simple time delay, self-phase modulation and grating compressors [123–125]. Yet all these setups offer no flexibility and require extensive realignment in order to change the temporal polarization profile. That is why only relatively simple polarization-shaped laser pulses have been produced. To offer more flexibility and to ease the requirements for realignment, the use of conventional femtosecond pulse shapers (as described in Chapter 3.2.1) in the individual arms of the interferometer has been suggested [124], but not realized in an experimental setup. This could be due to a problem that all of the setups, incorporating Mach-Zehnder interferometers, share, namely the requirement for stability on the scale of the optical wavelength.

This requirement can be illustrated by using the following simple Gedanken

experiment. Let one assume that only time delay as frequency-dependent phase modulation is introduced. If one chooses the time delay to be a quarter of the oscillation period of the center frequency of the original linearly polarized laser pulse, this pulse is transformed into a circularly polarized one. If now the relative optical path length between the two arms fluctuates by only a small fraction of the optical wavelength, the resulting polarization state changes to elliptical. In the case of general spectral phase modulations, the resulting changes of the polarization state, caused by path length fluctuations, can be even more drastic. However, to provide this interferometric stability over an extended time period, which is necessary for the experiments, is very difficult and requires elaborate optical setups. Therefore, this method is not very suitable for typical quantum control experiments, which usually take several hours.

In order to overcome this requirement of interferometric stability the two polarization components must travel along the same beam path like they do for example in wave plates. So to retain flexibility it is better, of course, to use liquid-crystal displays instead of wave plates with their fixed optical retardance of the two polarization components. The increased flexibility of LCDs has been demonstrated with a three-layer device, which is capable to transform an arbitrary, time-independent polarization state of a continuous-wave laser into any other polarization state [126]. Eriksen *et al.* [127] have extended this method with the use of two many-pixel LCDs to encode information in the polarization state along the beam profile. Besides, these cw-applications two-layer LCDs have been used to modulate the spectral phase of two orthogonal polarization components [83]. The drawback of their setup was, however, the very low efficiency of the gratings for p-polarized light. Because the intensity of one component was lower by approximately two orders of magnitude than that of the other, this produced phase and amplitude modulated pulses rather than polarization-shaped ones. An improved optical setup for shaping the time-dependent polarization state of femtosecond pulses is presented in the following.

4.1.1 Polarization Pulse Shaper Setup

The femtosecond polarization pulse-shaper setup [128] is shown in Fig. 4.1. It consists of an all-reflective zero-dispersion compressor in a $4f$ -geometry. The input light, polarized along the x axis (for orientation of the different axes see Fig. 4.1), is diffracted by a holographic grating (1800 lines/mm) in Littrow configuration, tilted upwards by a small angle. The spatially dispersed spectrum hits a concave cylindrical mirror, placed at a distance of one focal length (80 mm) from the grating. A folding mirror (minimizing lens aberrations as compared to “direct” beam geometries) directs the spectrum along the x axis of a two-layer LCD (Cambridge Research & Instrumentation), which is placed in the so-called Fourier plane of the zero-dispersion compressor, at a distance of another focal length from the first cylindrical mirror. Each layer consists of 128 separate pixels, sized 100 μm

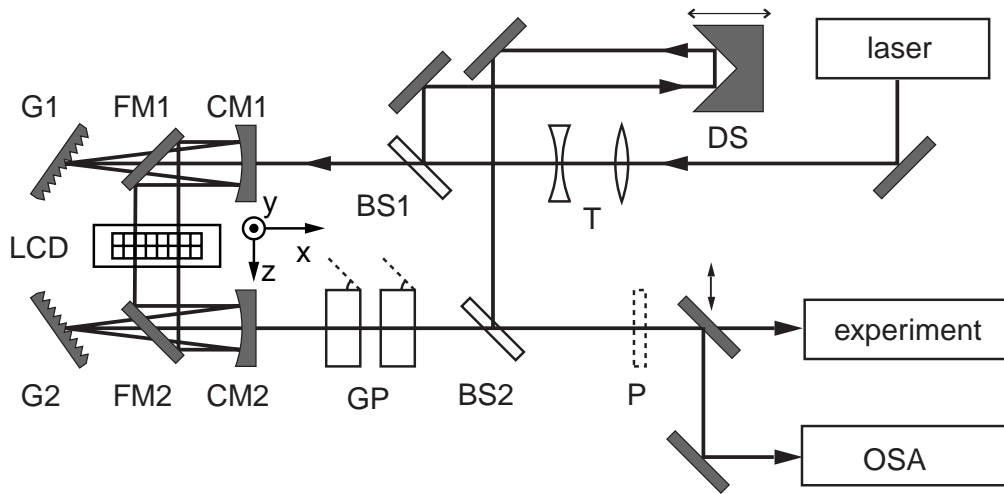


Figure 4.1: Setup of the polarization pulse shaper. A telescope (T) is used to adjust the beam diameter of the Ti:sapphire femtosecond laser. Beam splitters (BS1 + BS2) and a delay stage (DS) provide an unshaped reference beam for the pulse characterization. Pulse characterization is carried out in the beam path toward the experiment. For that purpose a polarizer (P) can be introduced in the beam path. The pulse shaper itself consists of an all-reflective zero-dispersion compressor employing holographic gratings (G1 and G2), cylindrical mirrors (CM1 and CM2), planar folding mirrors (FM1 and FM2) and a double-layer liquid-crystal display (LCD). All mirrors have “protected silver” coating. Compensation for the polarization-sensitive grating diffraction efficiency is achieved by transmitting the beam through a stack of glass plates (GP) at approximately Brewster’s angle.

width by 2 mm height. The z axis defines the direction of propagation. The preferential orientation axes of the nematic liquid-crystal molecules in the first and in the second LCD layers are located in the x - y plane, rotated by -45° and $+45^\circ$ respectively, from the x axis. The x -polarized input light has polarization components of equal magnitude along these two orientation axes, labeled as 1 and 2 in the following. If suitable voltages are applied to the separate pixels, the liquid-crystal molecules are tilted in the 1 - z and 2 - z planes respectively. Thereby they permit independent changes of the refractive indices for the two corresponding light-polarization components at 128 individual frequency intervals throughout the laser spectrum.

Recollimation of the laser beam is achieved by the symmetrically arranged second set of folding mirror, concave mirror, and grating. The grating efficiency is approximately 90% (30%) for x -(y -)polarized light. In order to compensate for this difference, a stack of four glass plates at approximately Brewster’s angle is used at the output of the pulse shaper, each reflecting 25% of the x -component out of the beam path and transmitting 100% of the y -component. Variations of

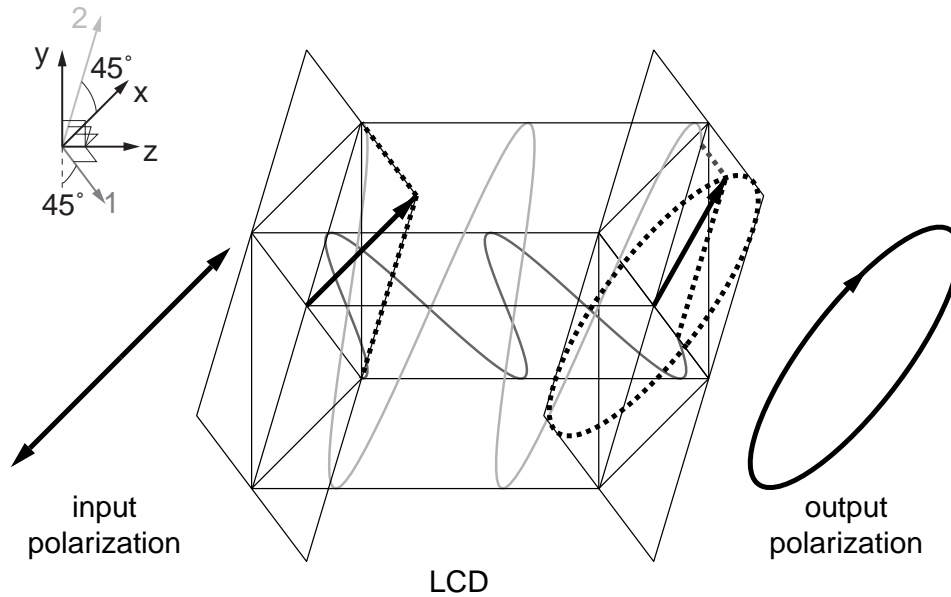


Figure 4.2: Principle of operation of the polarization pulse shaper. The linearly x -polarized input light of one particular frequency component can be decomposed into the polarization components 1 (dark gray) and 2 (light gray), which propagate collinearly but with different optical wavelengths. The resulting phase difference after passage through the LCD—which can be varied by applying suitable voltages—leads to elliptically polarized output light.

the total pulse energy for different pulse shapes are smaller than 1% for 60 fs laser pulses. For the broader spectrum of the sub 30 fs pulses used in Chapter 5 the maximal pulse energy variation is 5% because the difference in grating efficiency is slightly wavelength dependent and this cannot be compensated for all wavelengths simultaneously by the Brewster stack. The total energy throughput of the polarization shaper (including telescope, pulse characterization pickoffs and Brewster stack) is approximately 15%. It is interesting to note that the polarization pulse shaper can easily be converted into an amplitude-and-phase shaper by simply adding a polarizer after the LCD with its transmissive axis parallel to x , for instance. By sending the same phase functions to both layers it is also possible to use the polarization shaper as a phase-only shaper without adding any additional optics.

The principle of operation of the polarization pulse shaper is illustrated for one particular frequency component in Fig. 4.2. Starting with the projection of the x polarization (left side) onto the two components 1 and 2 (dashed lines), the propagation through the LCD begins with identical phase. However, the tensorial nature of the susceptibility is responsible for direction-dependent refractive indices and thus for a difference in optical wavelength between components 1 (dark gray) and 2 (light gray). These wavelengths can be varied individually

by applying suitable voltages to the electrodes of the corresponding LCD layers. The momentary electric field vector resulting at the exit plane of the LCD (arrow on the right) is constructed geometrically by appropriate projections of the phase-shifted components 1 and 2 (dashed lines). But, since light is a traveling wave, the momentary phases are functions of time; and the tip of the electric field vector evolves along the ellipse shown on the right side of the diagram. The degree of ellipticity depends on the relative phase difference between components 1 and 2, acquired upon propagation through both LCD layers. As the electric field amplitudes along the axes 1 and 2 remain constant upon transmission, any possible elliptical polarization has to be tangential to a square as indicated in the figure with its sides parallel to the 1 and 2 directions. Thus the principal axes of any polarization ellipse of one particular frequency component always point along the x and y directions. Yet, such transformations from linearly to elliptically polarized light can be performed independently for each spectral component. The total electric field in the time domain then depends on the interference between all the individual elliptically polarized frequency components. This leads to complex polarization-shaped laser pulses where there is no restriction on the direction of the principal axes.

4.1.2 Mathematical Description and Experimental Characterization

In order to describe polarization-shaped laser pulses it is sufficient to represent the electric field in two linearly independent vector components E_1 and E_2 , where E_1 and E_2 are given in either frequency or time domain. It is convenient (although not necessary) to choose the basis vectors linear and parallel to the LCD orientation axes 1 and 2. Assume that the vectorial electric field profile is given by its spectral components $E_1(\omega)$ and $E_2(\omega)$. The temporal electric field components $E_1(t)$ and $E_2(t)$ can then be obtained from $E_1(\omega)$ and $E_2(\omega)$ by inverse Fourier transformations. Polarization-shaped laser pulses can thus be described by

$$\begin{pmatrix} E_1(t) \\ E_2(t) \end{pmatrix} = \begin{pmatrix} 2A_1(t) \cos[\omega_0 t + \varphi_1(t)] \\ 2A_2(t) \cos[\omega_0 t + \varphi_2(t)] \end{pmatrix} \quad (4.1)$$

in terms of temporal amplitudes $A_1(t)$ and $A_2(t)$, the center frequency ω_0 and temporal phase modulations $\varphi_1(t)$ and $\varphi_2(t)$. Although this is a complete description, it gives very little insight about the time evolution of the polarization state of the laser pulse. This is due to the fact that the components E_1 and E_2 are coherently superimposed and interfere with each other. A much more intuitive picture of the laser pulse can be gained, if a principal axis transformation is performed from this “linear” description to an “elliptical” one.

In Fig. 4.3 the connection between the “linear” parameters $A_1(t)$ and $A_2(t)$ and the ellipticity ε and the orientation angle θ of the ellipse with respect to the laboratory-frame is graphically illustrated. As remaining parameters the total

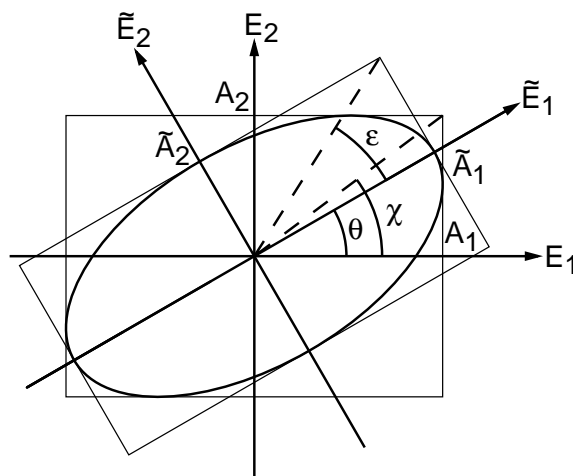


Figure 4.3: Elliptical pulse parameters. The light polarization ellipse is characterized by the major principal axis \tilde{A}_1 and the minor principal axis \tilde{A}_2 . These two amplitudes define the angle of ellipticity ε . The ellipse-inherent \tilde{E}_1 – \tilde{E}_2 coordinate system is rotated by the orientation angle θ with respect to the laboratory-frame E_1 – E_2 coordinate system. In the laboratory system, the ratio of the amplitude components A_1 and A_2 defines the angle χ as indicated.

intensity I and the so-called “total phase” $\varphi(t)$ are chosen. The total intensity transforms rather trivially from one description into the other, namely it is identical in both representations since the total pulse energy must not depend on the chosen coordinate system. The last remaining elliptical pulse parameter, the total phase $\varphi(t)$, is chosen as the sum of $\varphi_1(t)$ and the “geometrical” phase α which is associated with the fraction of one light field oscillation, which takes the electric field from pointing along the laboratory direction E_1 to pointing toward the perihelion of the ellipse. This relationship is illustrated in Fig. 4.4. Therefore, if one polarization component is small [e.g., $A_1(t) \approx 0$], the total phase $\varphi(t)$ resembles the phase of the remaining component [i.e., $\varphi(t) \approx \varphi_2(t)$]. For the exact mathematical transformation and the associated sign conventions see reference [129].

With the ability to almost arbitrarily shape the time-dependent polarization state of a femtosecond laser pulse and to describe it intuitively with the elliptical pulse parameters, it is necessary to adequately characterize the pulse shape experimentally. The characterization method must also cope with the difficulty that the polarization state is modified upon interaction with optical elements. This modulation is analyzed in detail in the next section of this work. Due to these changes in the polarization state the characterization must take place directly at the position of the experiment. This can be done by dual-channel spectral interferometry. This pulse diagnosis is very similar to the single channel spectral interferometry, already described in Chapter 3.3.2.

But unlike that technique it requires the collection of six different spectra: the

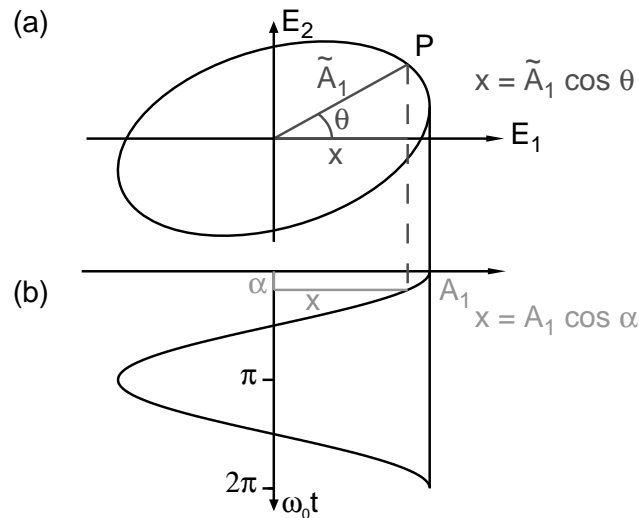


Figure 4.4: Meaning of the total phase. This figure illustrates the connection between the electric field oscillation of polarization-shaped light pulses (a) and the projection of the oscillation onto one polarization component (b). The position of the perihelion (P) of the light ellipse at orientation angle θ is related to the geometrical phase α of the associated oscillation of component E_1 . This relation can be evaluated by equating the distances x from both parts of this figure.

reference and shaped beams separately as well as combined for both polarization components. It had already been reported that such a setup could be used to analyze (simple) time-dependent polarization profiles [117, 130]. However, that discussion did not include the issue of total phase $\varphi(t)$. Since the reference pulse is linearly polarized, it can be characterized by standard techniques. For example, the reference pulse can be analyzed by FROG. The combination with dual-channel spectral interferometry has been called POLLIWOG (Polarization-Labelled Interference versus Wavelength of Only a Glint) [117].

The experimental setup for the pulse-characterization technique with dual-channel spectral interferometry is shown in Fig. 4.1. With the help of a first beam splitter (BS1), a small pick-off from the x -polarized input light is sent over a variable delay stage (DS). The two parts are then recombined collinearly at a second beam splitter (BS2). A polarizing film (P in Fig. 4.1, Polarcure) is placed directly into the recombined beam with its transmission axis at either $+45^\circ$ or -45° orientation with respect to the x axis. In this way both polarization components of the recombined laser beam can then be directed separately into the spectrometer by a single set of mirrors. Computer-controlled automatic shutters are used to facilitate the measurement of the interference spectra as well as the spectra of shaped and reference pulse alone. Spectral interference patterns of both components are recorded by a multichannel optical spectrum analyzer (OSA) with 2048 pixels and a resolution of 0.05 nm.

For the determination of the elliptical pulse parameters it is essential to measure the relative phase between the two polarization components in all spectral or temporal regions. For example, the ellipticity ε depends on the momentary value of the temporal phase difference between the two light polarization components. Therefore, it is important here that the relative phase between the two polarization components is always preserved. This relative phase can be determined (modulo 2π , which is sufficient) from the relative phase of the interference fringes between the two components, which are seen when the reference and shaped pulse both hit the spectrometer. This means that the exact positions of the interference maxima and minima of one polarization component with respect to those from the other component are evaluated. The experimental setup has to be stable enough to guarantee that the peak positions do not shift between the interferometric measurement of one and the other polarization component. This is generally feasible because stability is only required over a short time period. It is not critical if the fringe positions shift between successive measurements of different pulse shapes. Alternatively, two separate spectrometers or an imaging

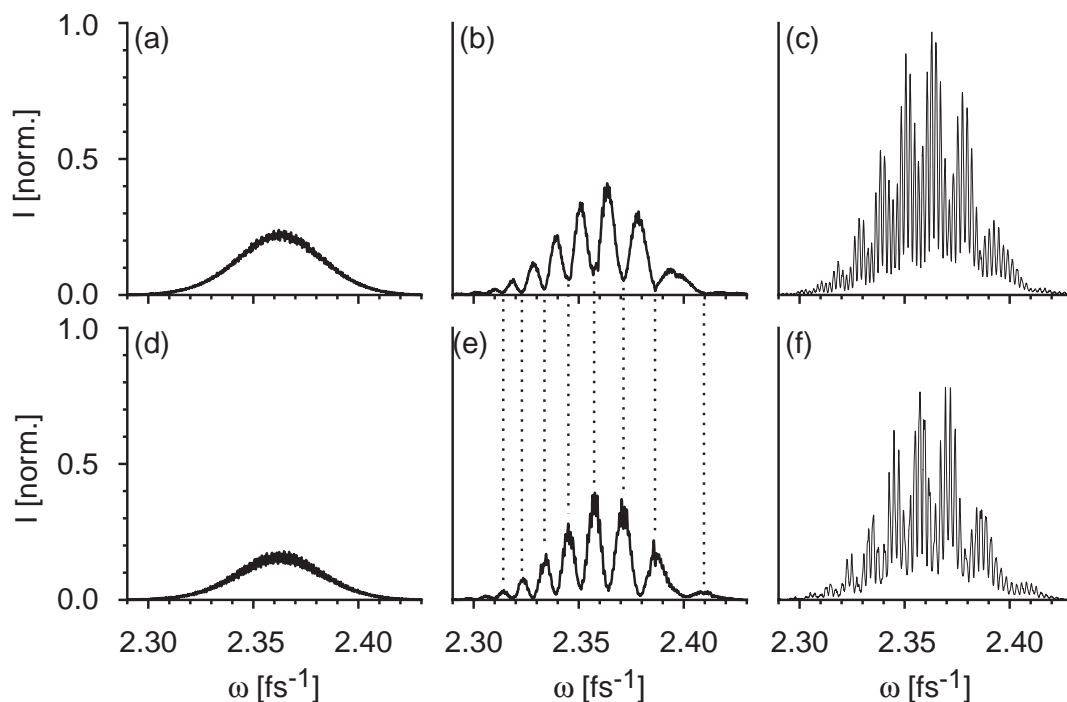


Figure 4.5: Dual-channel spectral interferometry. This graph shows experimental data as follows: (a) component 1 of reference laser field, (b) component 1 of shaped field, (c) component 1 of combined fields, (d) component 2 of reference field, (e) component 2 of shaped field, and (f) component 2 of combined fields. The intensities of the different spectra relative to each other have been preserved in this figure. The dotted guidelines emphasize that the intensity modulations in components 1 and 2 are out of phase with each other.

spectrometer with spatial resolution (for the two polarization components) could be used. It is emphasized again that the generation of the polarization-shaped pulses does not require interferometric stability, because both polarization components always travel along the same beam path.

In the following experimental example, linear spectral phase modulation of $b_1 = 500$ fs was applied to polarization component 1, and quadratic phase modulation of $b_2 = 5 \times 10^3$ fs² was applied to component 2. Here the coefficients b_1 and b_2 are the ones defined in Eq. (3.7). The six collected laser spectra necessary for the analysis are shown in Fig. 4.5. The two components of the reference beam (Figs. 4.5a and 4.5d) display the smooth Gaussian envelope of the Ti:sapphire oscillator used here. In contrast, the shaped spectra (Figs. 4.5b and 4.5e) are strongly amplitude-modulated (the origin of which will be explained in Section 4.2). It is noted that the oscillations in the two polarization components are out of phase with each other as can be seen by following the dotted guidelines. Hence it is possible that the total pulse energy remains constant despite the apparent redistribution of intensity. Note that these oscillations are not the interference fringes of spectral interferometry. The interference spectra between shaped field and reference field are rather shown in Figs. 4.5c and 4.5f, and the fringe spacing is much narrower than the distance between two intensity peaks of the shaped laser field in Fig. 4.5b and 4.5e. The amplitude modulation shows up in the interference spectra as a beating structure. The data analysis of Fig. 4.5 by the Fourier-transform method (see Chapter 3.3.2 and also Ref. [115, 131, 132]) leads to a complete characterization of the polarization-shaped laser pulse.

4.2 Polarization–Modulation

4.2.1 Polarization–Modulation by Subsequent Optical Elements

In this section the origin of the spectral amplitude modulations (see Fig. 4.5) is discussed. The modulation is caused by the additional optical elements, like metal-coated mirrors, gratings and glass plates. The reflection and transmission properties of these elements are governed by the Fresnel formulas [133]. If only the amplitudes for s- and p-polarization are different, like in the case of the gratings, this can be compensated by the Brewster stack. But amplitude differences in the Fresnel coefficients cannot account for the transfer of spectral components from the 1 to the 2-direction, as can be seen in Fig. 4.5, because such a difference would lead to an attenuation of both components by a different amount, but not to a transfer.

The different Fresnel coefficients for s- and p-polarization, however, introduce not only amplitude changes, but also phase differences. In order to illustrate the effect of such phase modulations consider the simple case of only one frequency

component and of equal amplitudes for s- and p-components and a phase difference of zero between them. It can easily be seen that this corresponds to a linearly polarized light field. After the acquisition of the additional phase difference, the amplitudes in the s- and p-direction remain unchanged, only one component lags behind the other. This, of course, corresponds to an elliptical polarization state. This polarization ellipse is still tangent to a square spanned by the equal amplitudes in s- and p-direction. If one analyzes this polarization state in the 1- and 2-direction, which is rotated by a certain angle with respect to the s-/p-system, one finds that there are amplitude changes along the 1- and 2-direction. What is even more important is that the changes have opposite signs. But this is exactly the situation one can see in Fig. 4.5, where spectral amplitudes have been transferred from one polarization direction into the other.

To summarize, the resulting polarization state of the light field at the position of the experiment is produced by pure spectral phase modulation by the LCD along the 1- and 2-direction to be followed by pure spectral phase modulation by the optical elements between the LCD and the experiment along the respective s- and p-directions. The result, however, is spectral amplitude modulation in the 1- and 2-components, which depends on the settings of the LCD.

4.2.2 Compensation Schemes for Phase Distortion

The question now arises whether it is possible to compensate those additional phase modulations, like it is possible for the amplitude modulations with the help of the Brewster stack. If the phase modulations are not frequency-dependent, in principle a compensation with $m \frac{\lambda}{n}$ wave plates is possible, where m is the number of optical elements after the LCD and $\frac{\lambda}{n}$ the negative of phase retardation introduced by the respective element. The following consideration shows, why this hypothetical setup allows for phase compensation. Just assume that one rotates the first wave plate in such a way that its ordinary and extraordinary directions coincide with the s- and p-direction of the last optical element. Since its retardation is the negative of the one introduced by the optical element, they cancel each other out. Therefore, the additional phase modulations by the optical elements can in principle be compensated one at a time. On the other hand, a setup containing m odd wave plates, where m is on the order of ten, is experimentally not feasible. Hence the possibility to replace the waveplates with one 3-layer 1-pixel LCD is investigated.

It was shown both experimentally and theoretically by Zhuang *et al.* [126], that such a device is capable to transform an arbitrary starting polarization state into any other polarization state on the Poincaré sphere. As the action of the combination of $m \frac{\lambda}{n}$ wave plates is m rotations about different axis on the Poincaré sphere, one can replace the m rotations by one rotation, connecting the start and end point, if no amplitude modulation occurs in between. Since the amplitude modulation in the polarization shaper setup mainly occurs at the grating and is

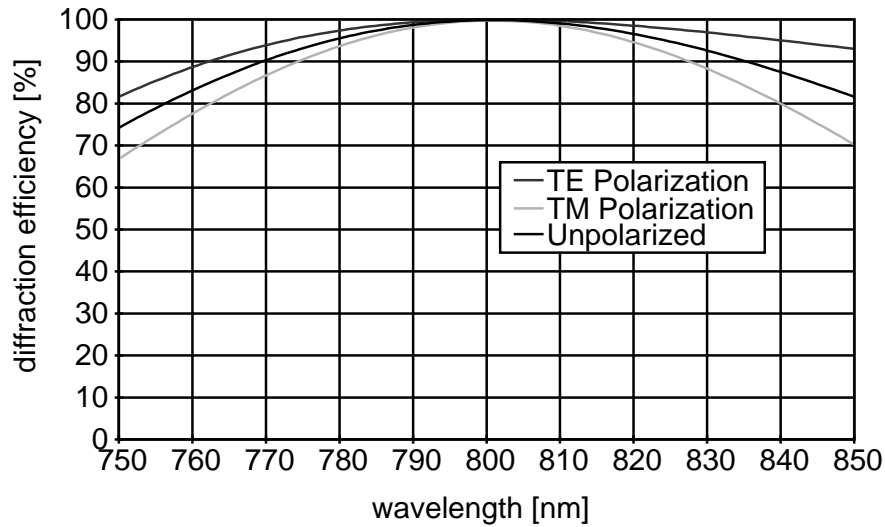


Figure 4.6: Diffraction efficiency of VPH gratings. This graph shows the theoretical performance curve (Kogelnik analysis) of a VPH grating of almost identical line spacing as the now used holographic reflection grating. Note that the diffraction efficiency within the bandwidth of the used laser pulses does not differ by more than 3% for the two polarization components. Data shown is courtesy of Kaiser Optical Systems.

subsequently canceled out by the modulation in the Brewster stack, this condition is not very well fulfilled. In order to use such a 3-layer 1-pixel LCD for compensation of additional phase modulations, it would be advantageous to avoid the amplitude modulations beforehand. The polarization dependence of the diffraction efficiency, however, is rather strong, 30% versus 90%, for the used holographic reflection gratings. Yet, there is a recent development from the telecommunication's community, so-called volume phase holographic (VPH) gratings. These gratings can offer diffraction efficiencies over 90% for both polarizations with a maximal difference of below 3%. A theoretical performance curve is shown in Fig. 4.6. The use of such gratings, from Kaiser Optical Systems for example, would allow to get rid of the Brewster stack. Thereby the number of optical elements after the LCD could be greatly reduced. This in turn also minimizes the introduced phase modulations by the optical elements. As an additional benefit, it would also allow to compensate for these phase modulations with one device that can transform any arbitrary, time-independent polarization state into any other. Besides the above mentioned 3-layer 1-pixel LCD, this would also be feasible with a Berek's Compensator [134]. The total energy throughput of the polarization shaper should also increase from 15% to about 60%, if VPH gratings are used.

However, the issue of additional phase modulation is only of minor importance, since its effects can be taken accurately into account via experimentally calibrated Jones matrices. The problem to deliver a specific polarization profile (not changed

by the phase modulations of the optical elements) for an experiment can be addressed by adaptive polarization shaping with experimental feedback. These two methods are presented in the following two sections.

4.3 Jones-Matrix Calculus

To calculate the output laser pulse from the settings for the LCD one needs to take the already discussed additional polarization modifications into account. This could be done theoretically by calculating the Fresnel coefficients for each optical element. However, in practice the errors e.g. in the determination of the incidence angles would add up to the point where no reliable prediction for the output polarization profile could be made. Therefore, the method of experimentally calibrated Jones matrices is employed. First a short introduction into the Jones matrix calculus is given with special emphasis on describing the action of the polarization pulse shaper. For a more thorough description of this matrix technique see reference [135].

The electric field of a polarization-shaped laser pulse can be described by a 2-component vector with two linearly independent components. As the temporal electric field $E(t)$ is real, knowledge about the positive frequency part of $E(\omega)$ is sufficient.

$$E^+(\omega) = \begin{cases} E(\omega) & \text{if } \omega \geq 0, \\ 0 & \text{if } \omega < 0. \end{cases} \quad (4.2)$$

The transfer function of any linear optical element can then be expressed by a 2×2 , complex valued, frequency-dependent matrix [135]. This is still true for non-isotropic elements like wave plates. The so-called Jones matrix \hat{J} relates the complex input field \vec{E}_{in}^+ with the output field \vec{E}_{out}^+ .

$$\begin{pmatrix} E_{1,out}^+(\omega) \\ E_{2,out}^+(\omega) \end{pmatrix} = \begin{pmatrix} J_{11}(\omega) & J_{12}(\omega) \\ J_{21}(\omega) & J_{22}(\omega) \end{pmatrix} \begin{pmatrix} E_{1,in}^+(\omega) \\ E_{2,in}^+(\omega) \end{pmatrix}. \quad (4.3)$$

For a combination of n elements the total Jones matrix is the matrix product of the n individual Jones matrices.

$$\hat{J}(\omega) = \hat{J}^{(n)}(\omega) \hat{J}^{(n-1)}(\omega) \dots \hat{J}^{(1)}(\omega). \quad (4.4)$$

The Jones matrix of the first optical element in the beam path is labeled \hat{J}^1 . The ordering is important since the matrix multiplication is non commutative. The action of the polarization pulse shaper can then be expressed by the following equation.

$$\begin{pmatrix} E_{1,out}^+ \\ E_{2,out}^+ \end{pmatrix} = \begin{pmatrix} J_{11}^{(2)} & J_{12}^{(2)} \\ J_{21}^{(2)} & J_{22}^{(2)} \end{pmatrix} \begin{pmatrix} e^{i\Phi_1} & 0 \\ 0 & e^{i\Phi_2} \end{pmatrix} \times \begin{pmatrix} J_{11}^{(1)} & J_{12}^{(1)} \\ J_{21}^{(1)} & J_{22}^{(1)} \end{pmatrix} \begin{pmatrix} E_{1,in}^+ \\ E_{2,in}^+ \end{pmatrix} \quad (4.5)$$

Here $\hat{J}^{(1)}$ is the combined Jones matrix of all optical elements from the first beam splitter to the LCD and $\hat{J}^{(2)}$ is the Jones matrix of all elements after the LCD. Φ_1 and Φ_2 are the phase functions applied by the two layers of the LCD. Equation (4.5) is very general. It can account for different coordinate systems of input and output fields as well as shaping directions. This coordinate transformation is achieved by rotation matrices, which are a very simple example of a Jones matrix. The ability for coordinate-system rotation is very useful in the case of imperfect alignment. It can take into account, for example, that the analyzing polarizer is not 100% collinear with the 1 and 2 direction of the LCD and still gives the correct output field. The goal of Jones-matrix analysis is to give a relation between the phase functions Φ_1 and Φ_2 and the output field $\vec{E}_{out}^+(\omega)$. Thus, it is convenient to simplify equation (4.5) to the following form.

$$\begin{pmatrix} E_{1,out}^+ \\ E_{2,out}^+ \end{pmatrix} = \begin{pmatrix} a_{11} & a_{12} \\ a_{21} & a_{22} \end{pmatrix} \begin{pmatrix} e^{i\Phi_1} \\ e^{i\Phi_2} \end{pmatrix} \quad (4.6)$$

Here the active element, the LCD, is separated from the modifications introduced by the passive optical elements. The \hat{a} matrix contains the input fields E_1^+, in , E_2^+, in and is identical for all pulse shapes.

In order to determine \hat{a} the output field is measured for m sets of different phase functions Φ_1 and Φ_2 via dual-channel spectral interferometry. It is important to sample a large part of the definition interval $[-\pi, \pi]$ of Φ_i to keep the experimental uncertainties low. Equation (4.6) is then separated into real and imaginary parts and converted to the standard form of 4m linear equations. The \hat{a} matrix is determined by a least-squares fit for each spectral component. The overdetermination of (4.6) and consecutive least-squares fit has proven to be more robust concerning measurement noise than measuring just two pulse shapes and solving the linear equation system with the minimal number of necessary measurements. It is, however, necessary that the relative phase relations are preserved during the entire measurement. The \hat{a} matrix from equation (4.6) can then be used to predict the pulse shape at the position of the experiment.

The result of an experimental determination of the \hat{a} matrix can be seen in Fig. 4.7. The absolute amplitude of the a_{kl} coefficients contains the spectra of the femtosecond laser pulse, as can be seen by their gaussian shape. The fact that they are not identical is due to the additional phase modulations, which transfer energy between E_1 and E_2 . This is also observed in the pulse characterization by dual-channel spectral interferometry (see Fig. 4.5e and 4.5f). The phases of the a_{kl} coefficients reflect mainly the introduction of quadratic spectral phase modulation in the pulse shaper setup. The quadratic term in the phases is due to material dispersion, which is mostly caused by the stack of glass plates at Brewster's angle. But, this introduced chirp is not critical since it can be compensated by the pulse shaper itself. This could even be done, if the exact amount of quadratic spectral phase modulation is not known, via adaptive recompression of the femtosecond laser pulses [87, 136, 137].

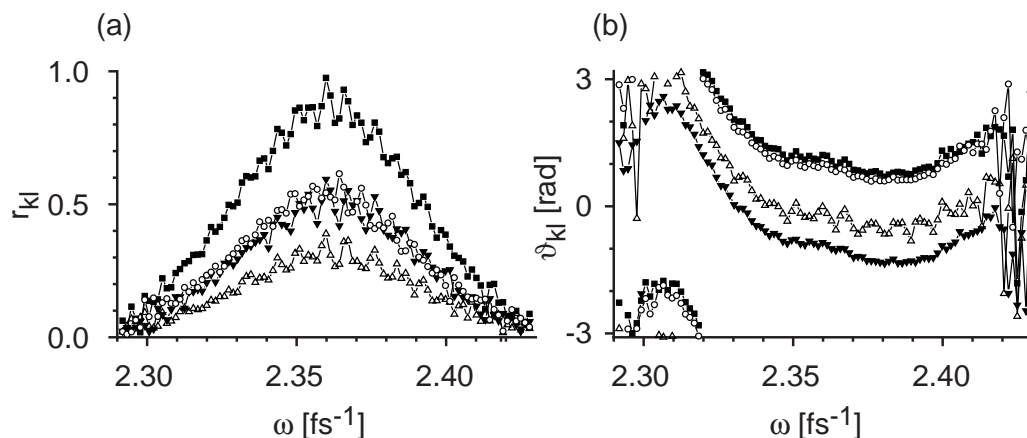


Figure 4.7: Experimental Jones-matrix determination. The results of the least-squares fit are (a) the absolute magnitudes r_{kl} and (b) the phases ϑ_{kl} of the frequency-dependent matrix coefficients a_{11} (solid squares), a_{12} (open circles), a_{21} (solid triangles), and a_{22} (open triangles). Not all data points acquired are shown in this figure. The pulse shapes used for this fit were generated by applying the following four pairs of spectrally constant phases: $\{\Phi_1/\text{rad}, \Phi_2/\text{rad}\} = \{b_0 = 3.0, b_0 = 0.0\}$, $\{b_0 = -1.78, b_0 = 0.0\}$, $\{b_0 = 0.0, b_0 = 1.5\}$, and $\{b_0 = 0.0, b_0 = 3.0\}$.

To check the reliability of experimentally calibrated Jones matrices for exact output pulse prediction, its results are now compared to an independent output measurement by using dual-channel spectral interferometry for a sample pulse. First, the output of an idealized pulse shaper is shown in Fig. 4.8a. For this idealized shaper a perfect gaussian shaped input laser spectrum is assumed. As no additional pulse modification takes place, both spectra are identical and show no amplitude modulation. The spectral phases match exactly the preset phase functions of $b_1 = 500 \text{ fs}$ for Φ_1 (dashed line) and $b_2 = 5 \times 10^3 \text{ fs}^2$ for Φ_2 (solid line) at the LCD. Yet, as it is shown in the previous sections, actual pulse shapers do exhibit additional pulse modifications. Therefore, deviations from the ideal case should be present in the two measurements shown in Fig. 4.8b with dual-channel spectral interferometry and 4.8c with Jones matrix calculus. Both measurements exhibit spectral amplitude modulation as discussed in Section 4.2. The general shapes of the output phases are similar to the ideal case, but some distortions are clearly seen. Those distortions originate from the same effects that lead to the spectral amplitude modulation. Comparing Fig. 4.8b and c, it can be seen that Jones matrix calculus has the ability to precisely predict the spectral intensity modulations (top row) and the phase distortions (bottom row). Both experimental characterization methods give consistent and reliable results, thus enabling one to quantitatively understand the complete behaviour of the polarization pulse shaper.

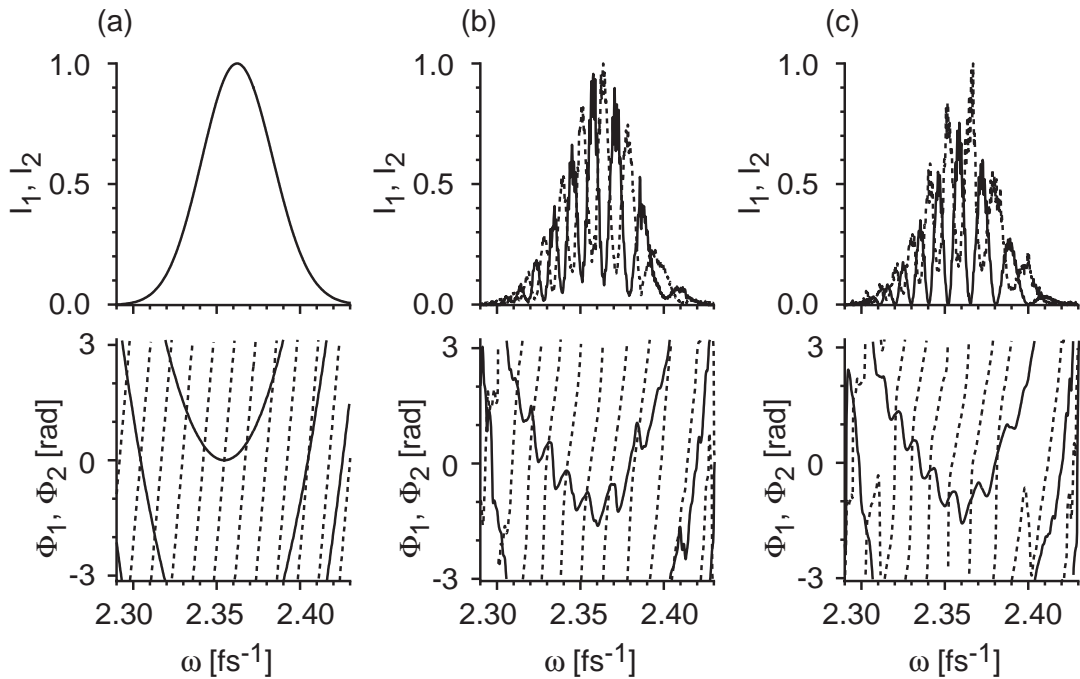


Figure 4.8: Comparison of polarization pulse characterization methods. Spectral intensities (top row) and spectral phases (bottom row) of a polarization-shaped laser pulse are shown for the polarization components 1 (dashed lines) and 2 (solid lines) as determined (a) by simulation without additional pulse-shape modification, (b) by dual-channel spectral interferometry, and (c) by Jones calculus.

4.4 Adaptive Polarization Shaping

With the complete quantitative understanding of the polarization shaper one can now think about adaptive quantum control experiments, which use polarization as an active agent. In a general quantum control experiment the optimal pulse shape is often not known a priori. Therefore, quantum control has greatly benefitted from the implementation of learning loops with experimental feedback [36, 37, 40, 138]. Polarization shaping, which can further on access the vectorial properties of femtosecond laser pulses, can be expected to reach new levels of control of quantum systems as compared to phase-only pulse shaping. A time-dependent polarization profile should play an important role, for example in the selective production of enantiomers [46, 51, 139, 140]. But, considering the complexity of this and other potential applications, it is highly unlikely that the optimal time-dependent polarization profile can be known from theory. Even if this should be the case, the modification of polarization shaped laser pulses by additional optical elements makes it very difficult to deliver this pulse shape to the position of the experiment. For this reason polarization shaping should capitalize on the implementation of adaptive learning algorithms. The following experiments can

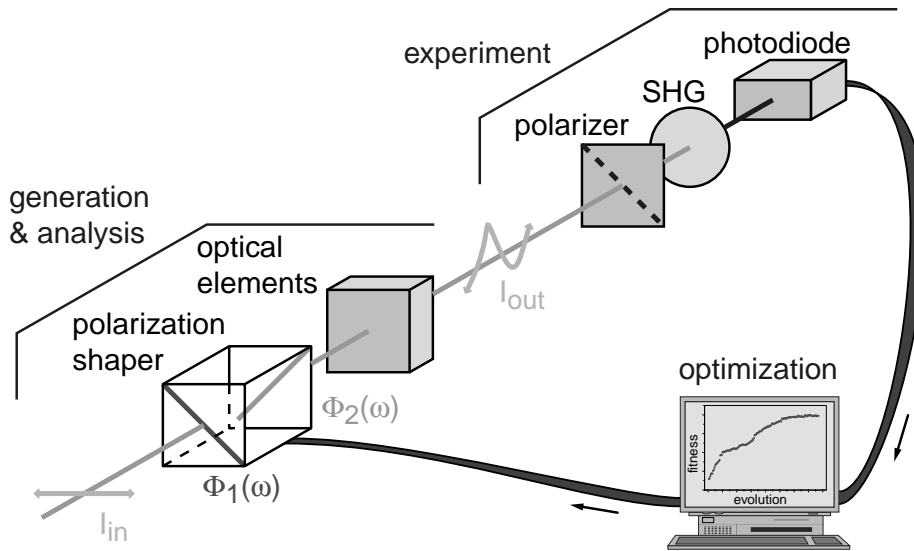


Figure 4.9: Setup for optical demonstration experiments. In the generation-and-analysis part, polarization-shaped laser pulses are produced by spectral phase variations $\Phi_1(\omega)$ and $\Phi_2(\omega)$ of two orthogonal polarization components. These laser pulses are then partially modified by additional optical elements. The experimental part is based on second-harmonic generation (SHG) after a polarizer, a shortpass filter to remove the fundamental, and a photomultiplier tube (PMT) for signal detection. The experimental feedback is used in an optimization algorithm which iteratively improves the pulse-shaper settings such that the SHG intensity is maximized.

be regarded as “laboratory simulations” of such more complex quantum control experiments for which the optimal time-dependent polarization profile is not known a priori.

4.4.1 Linear Polarization as Target

The first optical demonstration experiment consists of a polarizer aligned along the 1-axis of the pulse shaper and subsequent second harmonic generation (SHG) in a 100 μm thick BBO crystal (Beta Barium Borate). The setup is shown in Fig. 4.9. The SHG is filtered with a shortwave-pass BG-40 color glass filter and measured spectrally and temporally integrated with a photomultiplier tube (PMT, 1P28 from Hamamatsu). This SHG signal is used as feedback for the evolutionary algorithm. Since SHG in thin crystals is proportional to the square of the incoming fundamental field $E(t)$ (see Section 3.2.2), a temporally short, bandwidth-limited laser pulse with linear polarization is the optimal solution.

The evolution of the SHG feedback signal is shown in Fig. 4.10. The optimization is performed for three different numbers of free parameters. The free parameters are the phase value at the 256 individual pixels of the LCD. In order

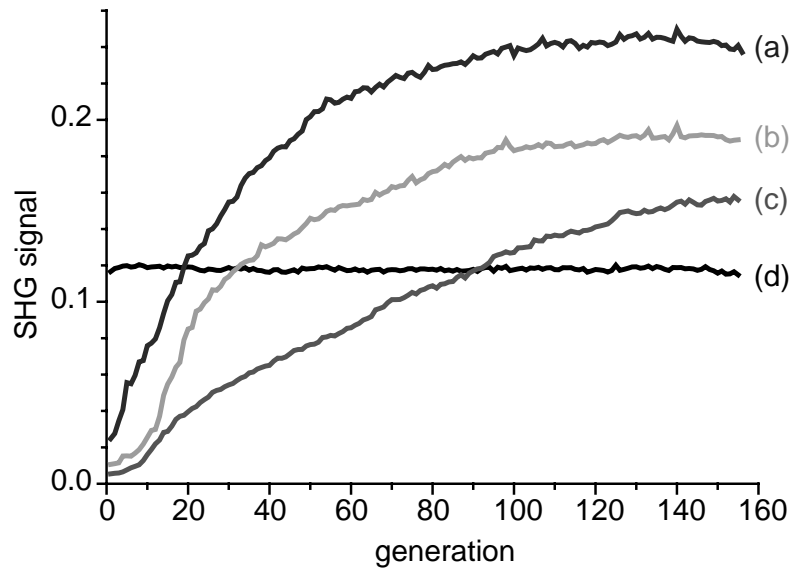


Figure 4.10: Evolution curve for adaptive polarization shaping to maximize SHG. The second harmonic signal is shown for the case of 64 (a), 128 (b) and 256 (c) free parameters of the pulse shaper as a function of the generation. For comparison curve (d) displays the yield of an unshaped laser pulse. Note that all three optimizations were run in parallel in order to avoid changes due to different input laser performance.

to reduce this number, 2 or 4 adjacent pixels in each one of the two layers are coupled together. As to avoid unmeaningful differences in the comparison of the three optimizations, the three strategies are run in parallel. This ensures identical experimental conditions for all three cases. For the maximum number of parameters to be optimized (Fig. 4.10c) the slowest convergence rate is observed. After 150 generations the signal has not yet converged to an optimum. For lower and lower number of free parameters the convergence rate increases and a higher SHG signal is reached at the end of the optimization. This is probably due to the fact that the required optimal pulse shape is rather simple. Therefore the higher spectral resolution offered by more free parameters is not needed for this optimization. However, it cannot be excluded that the algorithm needs to be adapted for higher parameter numbers and thereby vastly larger search spaces. In order to compare two optimizations directly, it might therefore be advantageous to use the same number of parameters in both cases. Nevertheless, the algorithm has found an optimal pulse shape in each case that performs significantly better than an unshaped laser pulse. It is therefore interesting to analyze the optimal pulse shape and check to what extent it matches the expectation of a temporally short laser pulse linearly polarized along the 1-direction.

In Fig. 4.11a the original unshaped laser pulse is shown. It has nearly equal intensities along the 1- (open squares) and 2-direction (solid triangles), which sum up to give the total intensity shown as solid line (top row). The ellipticity ε (bot-

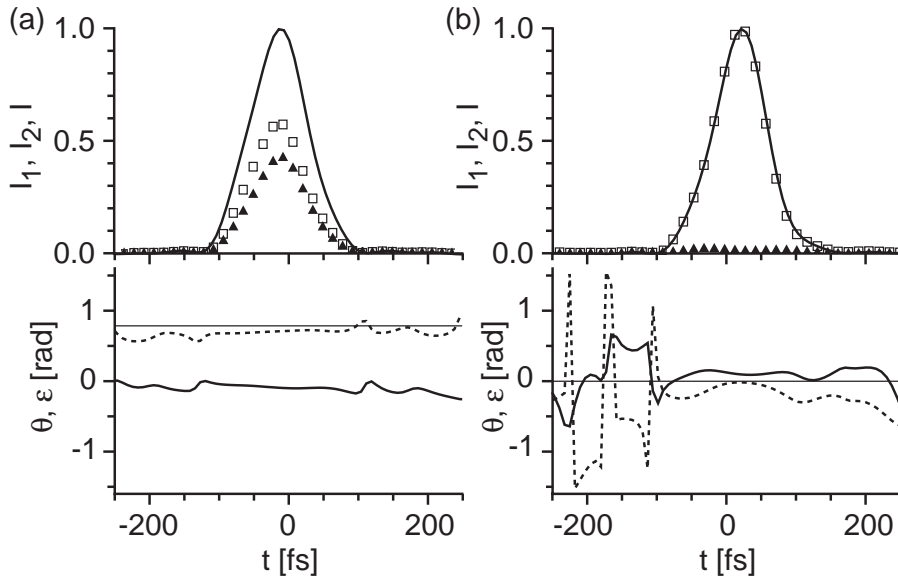


Figure 4.11: Laser pulse shapes after adaptive polarization shaping (a) for an unmodulated laser pulse, and (b) for the optimized laser pulse. In the top row, the temporal total intensity (solid line) and the intensity components I_1 (open squares) and I_2 (solid triangles) are shown. The bottom row contains the temporal polarization parameters ε (thick solid line) and θ (dashed line), analyzed by Jones-matrix calculus.

tom row, thick solid curve) is zero at all spectral positions with non-zero intensity. The orientation angle θ (dashed curve) is approximately $\pi/4$ (thin solid curve), denoting a linearly x -polarized laser pulse. Since the input laser pulse is linearly x -polarized, this behaviour of the pulse shaper is expected for zero LCD phases. The slight deviations from this expected polarization state can be explained by the additional modifications caused through the optical elements (as discussed in Section 4.2). The optimal polarization-shaped laser pulse [Fig. 4.11b] found by the evolutionary algorithm after 150 generations is indeed linearly polarized, i.e. the ellipticity ε (bottom row, thick solid curve) is approximately zero (thin curve). The orientation angle θ (dashed curve), however, is now also zero. In other words, the polarization is pointing along the transmission axis of the polarizer. The intensity from component I_2 (top row, solid triangles) has been almost completely transferred to intensity component I_1 (open squares). To summarize, the polarization shaper in combination with an evolutionary algorithm found the desired short laser pulse linearly polarized along the 1-axis. In this experiment the special ability of the pulse shaper to produce time-dependent polarization profiles is not exploited since the result could have been achieved with a zero-order 800 nm wave plate as well. Nevertheless, the operation of adaptive femtosecond polarization shaping proved successful.

4.4.2 Compensation for Dispersion and Polarization Distortion

In quantum control of complex systems more complicated pulse shapes are expected. The question now arises whether the adaptive polarization-shaping technique can also come up with such—more complicated—solutions, if they are required for the optimization of the feedback signal. To answer this question, the experiment shown schematically in Fig. 4.12 is performed. In comparison to the first adaptive polarization-shaping experiment, the polarizer is replaced by a multiple-order wave plate for 620 nm. This introduces a frequency-dependent phase difference between the two polarization components 1 and 2. In other words, the linear input polarization is completely “messed up”. On top of that a highly dispersive SF10 glass rod is inserted in the beam path. This results in dominantly second-order spectral phase modulation for both polarization components. Previous experiments [87] have shown adaptive recompression of such chirped pulses using phase-only shaping. In this experiment, however, both chirping and polarization modulation is required for the optimal pulse shape.

Therefore, two optimization strategies are used here, namely phase-only shaping and polarization shaping. For both strategies the same spectral resolution is used. The phase-only shaping is achieved by forcing Φ_1 to equal Φ_2 . The evolution curves are shown in Fig. 4.13 for both cases. The SHG yield of unmodulated laser pulses is outdone for both strategies in the first generation and significant further improvements are achieved. However, polarization shaping gives more than twice the SHG signal than phase-only shaping. This is due to the fact that here not only the second-order group-velocity dispersion from the SF10 rod is compensated, but also the polarization modulations introduced by the “wrong” wave plate. The spectral phases (see Fig. 4.14a and b support that explanation further. The dominant contribution in both cases is the second-order spectral phase that compensates the material dispersion. When looking at the differences between graph c and d, the following features are most pronounced. In the case

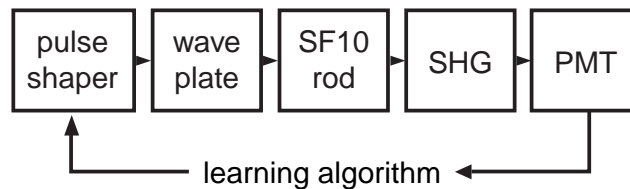


Figure 4.12: Schematic experimental setup for adaptive dispersion-and-polarization compensation experiment. After the pulse shaper a multiple-order wave plate designed for use at 620 nm distorts the polarization state and dominantly second order spectral phase is introduced by material dispersion in a 10 cm SF10 glass rod. The feedback signal for the learning algorithm is generated by SHG in a 100 μm thick BBO crystal.

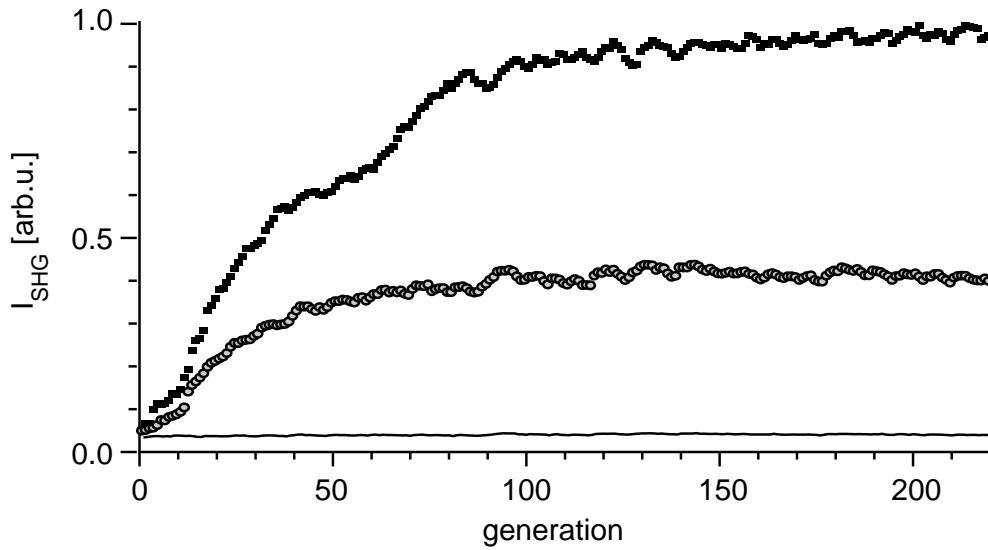


Figure 4.13: Evolution curves of dispersion-and-polarization compensation experiment. The SHG signal for the fittest individuals is plotted as a function of generation number of the evolutionary algorithm. In the case of polarization shaping (solid squares), sequences of two neighbouring pixels were coupled together. In the case of linear phase-only shaping (open circles), sequences of two pixels and additionally the phase values of the first and the second LCD layer were coupled together. The simultaneously recorded SHG signal for unmodulated laser pulses is also shown (solid line).

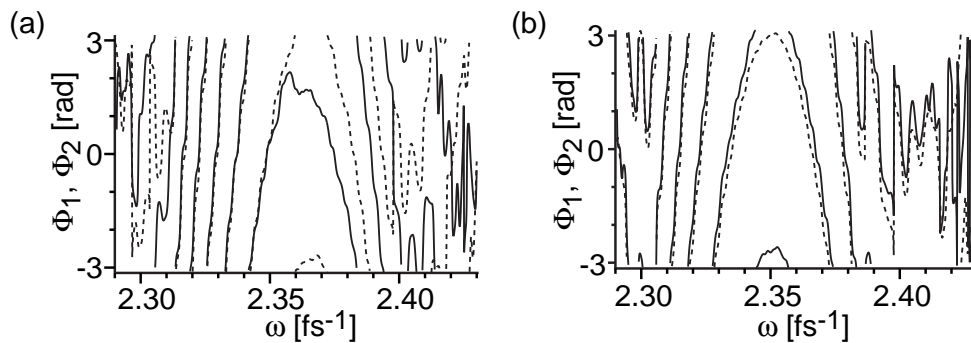


Figure 4.14: Resulting phases of dispersion-and-polarization compensation experiment. The resulting phases show in both cases, polarization shaping (a) and phase-only shaping (b), a dominant parabolic term that compensates material dispersion. Note that in the polarization-shaping case the phases Φ_1 and Φ_2 differ in the high frequency part to compensate the polarization distortion of the “wrong” wave plate.

of linear phase-only shaping (Fig. 4.14b), the two phase components are almost identical, because they were not allowed to vary independently. The small difference between Φ_1 (dashed line) and Φ_2 (solid line) is attributed to additional pulse-shape modifications in optical elements as described in the previous sections. With phase-only shaping, it is possible to compensate for the material dispersion, but not for the polarization modulation of the wave plate. This additional compensation is achieved in the phase-and-polarization shaping experiment (Fig. 4.14a). Here, the two phase components are different from each other. This deviation is seen mainly in the high-frequency part where Φ_1 (dashed line) lies above Φ_2 (solid line), canceling the frequency-dependent phase introduced by the “wrong” wave plate. Hence, both the polarization state of a “distorted” laser pulse was “cleaned up” and material dispersion was compensated for.

4.5 Conclusion

In conclusion, the technique of polarization-shaping of femtosecond light pulses was introduced. It allows to change the polarization state, i.e. the ellipticity and angle of orientation of the elliptical principal axes, on an ultrafast timescale. Complete pulse characterization was achieved by dual channel spectral interferometry. Alternatively experimentally calibrated Jones matrices were used to predict the pulse shape at the position of the experiment. This is very important as additional optical elements modify the polarization profile. These modifications were investigated and some solutions suggested to further improve the optical setup of the polarization shaper. The polarization-shaped laser pulses were then combined with a learning algorithm in an optical demonstration experiment. After these successful “laboratory simulations” of adaptive femtosecond polarization shaping, the next step is to apply this technique to a quantum system. There, the new degree of freedom, i.e. to vary the polarization state on an ultrashort time scale, should open a new level of control. This is investigated in the next chapter using the potassium dimer as model quantum system.

5 Ultrafast Polarization Quantum Control

In the previous chapter the generation and characterization of polarization-shaped femtosecond laser pulses were introduced. The implementation of these techniques within a learning loop with an optical signal as feedback was demonstrated. In this chapter, adaptive polarization shaping is applied to a model quantum system, the potassium dimer. At first, the advantages of using polarization as active agent in quantum control are introduced (Section 5.1). Section 5.2 shows the polarization-sensitive multiphoton ionization pathways in this molecule. For this purpose pump-probe experiments with different linearly polarized laser pulses are carried out. In Section 5.3 these polarization-sensitive pathways are exploited in a more general way via adaptive quantum control by ultrafast polarization shaping.

5.1 Introduction

Coherent control is a powerful method, which allows to “steer” quantum-mechanical processes toward a desired outcome by applying optimal light fields [141]. The main experimental tool for achieving this goal has been spectral phase shaping of femtosecond laser pulses. However, “conventional” pulse shaping [85] accesses only the scalar properties of ultrashort laser pulses, while the electric field is a vectorial quantity. Since quantum systems and their wavefunctions are three-dimensional objects, the use of polarization as an active agent could tremendously increase the degree of attainable control.

Time-dependent polarization states have been suggested, for example, for the generation [64, 65] and characterization [66] of attosecond light pulses, optical control of lattice vibrations [142] and the selective production of enantiomers [46, 49]. Simple time-dependent polarization profiles (without using pulse shapers) had already been exploited in several experiments on optical [117, 123], atomic [124], and molecular systems [125]. Molecular Chlorine, for example, was spun to “death” by using a time-dependent polarization profile to accelerate the molecule from near rest up to angular momentum states with $J \approx 420$, where it dissociates. Oron *et al.* have used spectral modulation of phase and polarization

direction in coherent anti-Stokes Raman spectroscopy (CARS) [143].

However, the prospect for manipulating light–matter interactions in three dimensions using complex polarization-modulated laser pulses goes beyond these initial suggestions or demonstrations. While this interaction is governed by the scalar product $\vec{\mu} \cdot \vec{E}(t)$, in most experimental and theoretical studies on quantum control or nonlinear spectroscopy, the vectorial character of $\vec{E}(t)$ is ignored completely and only $\mu E(t)$ is considered. But, if the momentary polarization of the applied electromagnetic field is varied, $\vec{\mu} \cdot \vec{E}(t)$ can be optimized throughout the complete temporal evolution of a quantum system. This opens many experimental perspectives, e.g. controlling which dipole transitions are allowed at any particular time during a wave–packet evolution. Thus, one can address and exploit the spatio–temporal properties of quantum wavefunctions.

In order to illustrate the novel features of such polarization quantum control experiments the photoionization in a small prototype system, the potassium dimer K_2 , is maximized (Section 5.3). The reason for this polarization sensitivity is investigated with pump–probe experiments with mutually perpendicular polarizations and parallel polarizations of the femtosecond laser pulses (Section 5.2).

5.2 Polarization–Sensitive Dynamics in the K_2 –System

The potassium dimer is well investigated and understood both experimentally and theoretically [144–150]. The potential energy curves are shown in Fig. 5.1. Within the bandwidth of the laser system, the dominant transition pathway that contributes to the K_2^+ yield [150] populates the $2^1\Pi_g$ state as an intermediate before the final ionization step. The $2^1\Pi_g$ state can be reached from the $X^1\Sigma_g^+$ ground state by a two-photon process with intermediate wave–packet propagation in the $A^1\Sigma_u^+$ state. This pathway is strongly polarization dependent, because according to selection rules the two involved electronic transitions, $A^1\Sigma_u^+ \leftarrow X^1\Sigma_g^+$ and $2^1\Pi_g \leftarrow A^1\Sigma_u^+$, require electromagnetic fields with polarizations parallel and perpendicular to the molecular axis, respectively. This means that for maximum population of the $2^1\Pi_g$ state one needs a laser pulse sequence in which the correct direction of the electric field vector is provided at the appropriate Franck–Condon transition windows reached during vibrational wave–packet motion. The enhancement factor for polarization-shaped laser pulses can be estimated in a simple model. Consider an isotropic ensemble of quantum systems in which two subsequent transitions require two electromagnetic fields with mutually perpendicular polarizations. If one employs two laser pulses with the same linear polarization, only the projections of the polarization vector onto the involved dipole moments of the randomly oriented systems contribute to the transition rates. The total transition rate is then given by averaging over the isotropic ensemble. In comparison then, if the polarizations of the two laser pulses are perpendicular

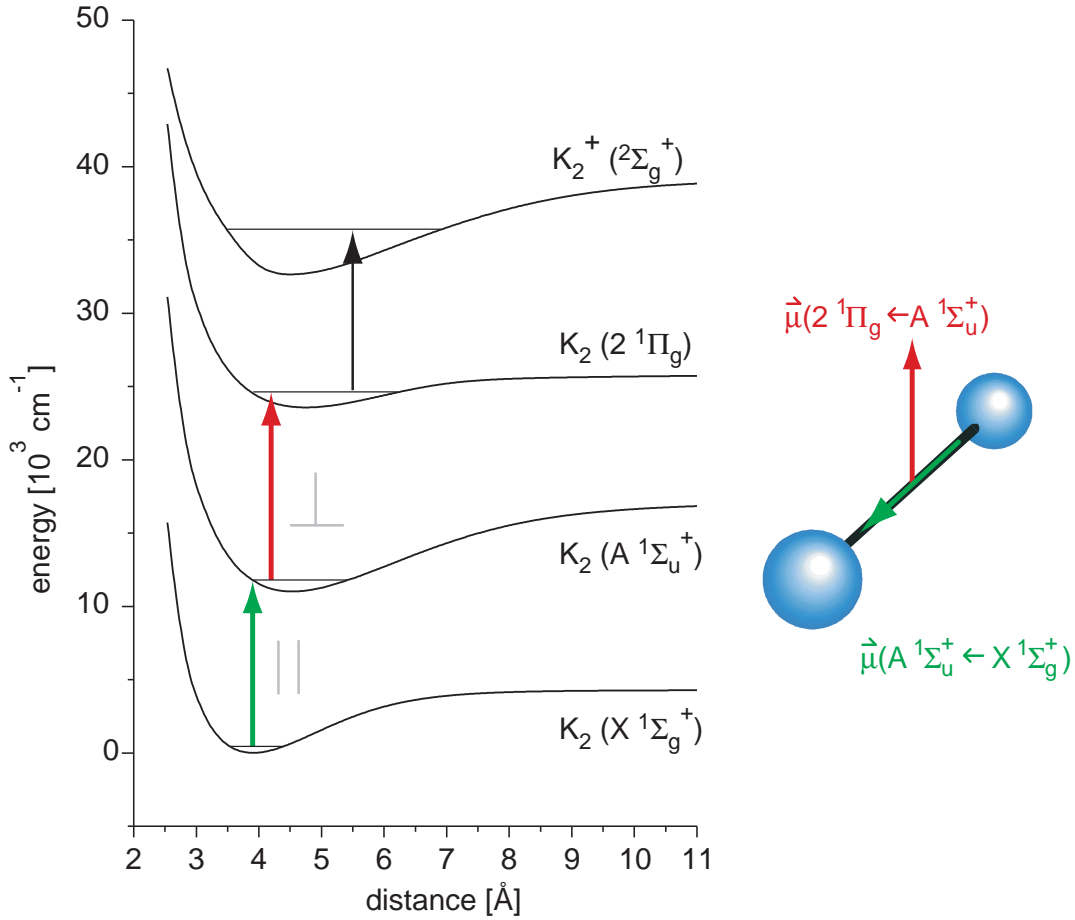


Figure 5.1: Calculated potential energy curves of the potassium dimer system. Only those curves are shown which are relevant at the central excitation wavelength of $\lambda = 785$ nm used in this experiment. The arrows indicate the multiphoton pathway that leads to the production of K_2^+ -ions. The gray symbols indicate the transitions with the light polarization parallel or respectively perpendicular to the molecular axis. The potential energy curves are taken from Ref. [150]. On the right side a graphical illustration of the K_2 together with the directions of the first two transition dipole moments is shown.

to each other, the averaging procedure gives a yield that is enhanced by a factor of two. Further advantages of polarization shaping arise if the quantum systems are aligned or oriented with respect to the incoming light fields [55, 58]. Optimal control of the multiphoton ionization process therefore requires both adjustment of the temporal intensity profile (to maximize the transition probability in the Franck–Condon regions) as well as variation of the polarization direction to fulfill the appropriate selection-rule requirements. Such a scheme cannot be achieved with shaped laser pulses of only one polarization component.

In order to illustrate these issues further, a “conventional” pump–probe ex-

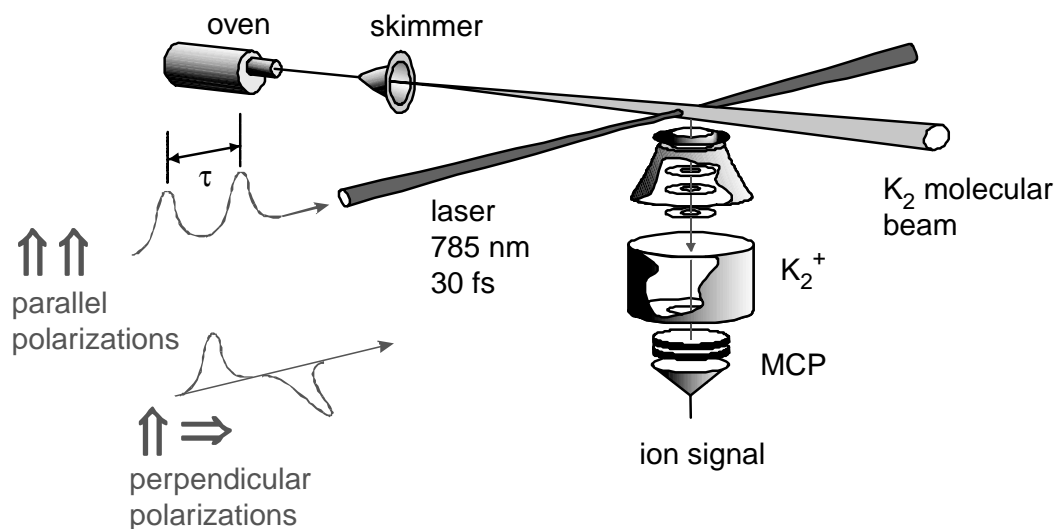


Figure 5.2: Pump–probe setup. The pump and probe laser pulses with polarizations parallel or perpendicular to the time-of-flight (TOF) mass spectrometer axis intersect with a supersonic molecular beam of potassium dimer molecules. The produced ions are detected in a TOF mass spectrometer with a multi–channel plate (MCP) detector.

periment is performed in partially aligned K_2 molecules where the alignment is due to suitable molecular beam conditions [151–153]. The experimental setup, shown in Fig. 5.2, consists of a supersonic molecular-beam apparatus with a linear time-of-flight (TOF) mass spectrometer. Both pump and probe laser pulses have an energy of 150 nJ and are focused with a 500 mm lens onto a molecular beam of potassium dimers thus avoiding strong field effects. The molecular beam was created by using an oven temperature of 500 °C and by seeding the beam with Ar of 1.5 bar pressure. In the TOF mass spectrometer the produced ions of the same charge state q are accelerated to a certain kinetic energy $E_{kin} = mv^2/2 = qU$ with the accelerating voltage U . The ions pass then through a field free drift region and hit a micro channel plate (MCP) detector. The voltage pulse produced in this detector is then recorded either via boxcar integration (SR250 from Stanford Research Systems) and analog–to–digital conversion in a computer card or via direct transient analysis in a digital oscilloscope (LC574A from LeCroy). The time of flight, i.e. the time between laser interaction and detection of the ions in the MCP, is, of course, proportional to the square root of their mass for singly charged ions. The mass resolution of the linear TOF mass spectrometer is sufficient to separate the potassium isotopes ^{39}K (93% natural abundance) and ^{41}K (7%). All further experiments are performed on the most abundant dimer $^{39,39}K_2$.

First, equally intense pump and probe laser pulses both polarized parallel to the TOF axis are used. The amount of K_2^+ as a function of pump–probe delay

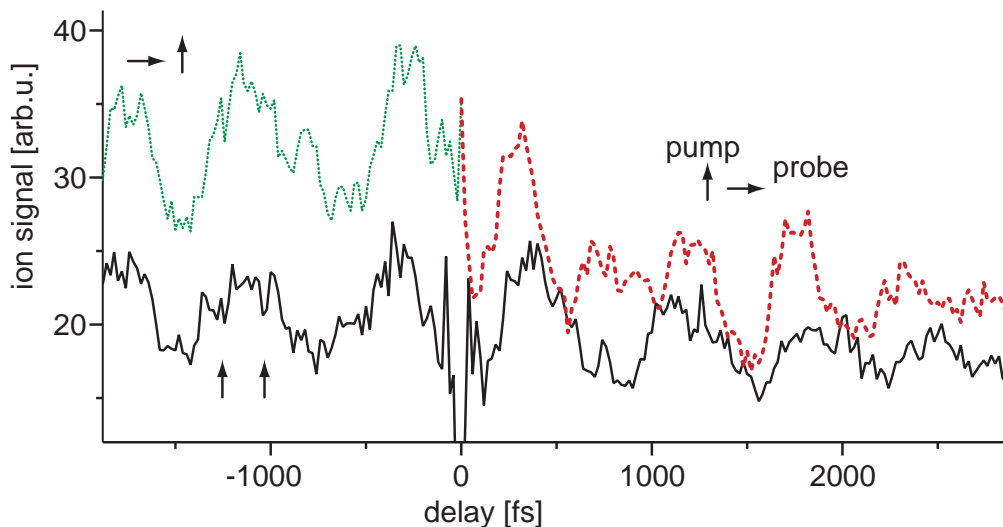


Figure 5.3: Section of pump-probe transients with mutually parallel (solid black line) and crossed (dotted green/dashed red line) linear polarizations around delay time zero. The timing of the differently polarized pump and probe pulses is depicted with arrows.

(Fig. 5.3, solid black line) is symmetric and shows a minimum with respect to time zero. On the other hand, if the probe-pulse polarization is perpendicular to that of the pump laser pulse, the signal is asymmetric (Fig. 5.3, dotted green/dashed red line); and for negative time delays the K_2^+ production is significantly enhanced. This result proves the polarization dependence of the K_2^+ ionization pathways. It indicates that a certain final quantum state (in this case the K_2^+ ion) can be more efficiently reached by a time-dependent polarization of the controlling laser field. The asymmetry in the pump-probe transient, i.e. higher average signal at negative times, is a clear indication of the partial alignment of the K_2 molecules. Since pump and probe laser are identical but for their polarization direction, higher signal at negative delay times, where the first laser pulse is polarized perpendicular to the TOF mass spectrometer axis (see Fig. 5.2), is a sign that more K_2 molecules fly along with their rotational angular momentum vector perpendicular than parallel to the molecular beam.

Fourier analysis of the pump-probe transients reveals that for mutually parallel pump and probe polarizations (Fig. 5.5, left graph) only the dynamics in the $2^1\Pi_g$ state (average vibrational quantum number $\bar{\nu}' = 24$) with a vibrational period of 740 fs [150] (corresponding to 45 cm^{-1}) is visible. This observation of $2^1\Pi_g$ state dynamics shows that ionization from the $2^1\Pi_g$ is dependent on the internuclear distance and occurs predominantly at the outer turning point. For mutually perpendicular pump and probe polarizations (Fig. 5.5, right graph) an additional Fourier peak is found at 65 cm^{-1} (corresponding to 510 fs), which can be attributed to vibrational dynamics in the $A^1\Sigma_u^+$ state ($\bar{\nu}' = 14$). The

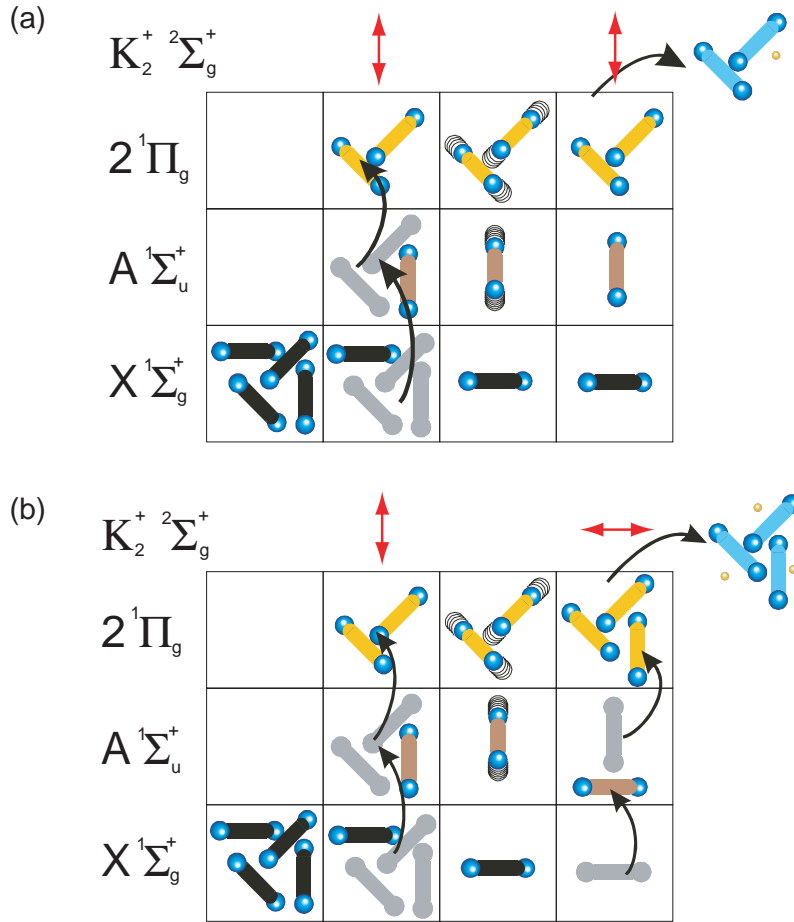


Figure 5.4: Model for pump-probe transients in K_2 for the case of parallel (a) and perpendicular (b) pump-probe polarizations. The squares from left to right depict a movie of the K_2 dynamics. The steps are: isotropic ensemble before laser interaction, interaction with pump pulse, field-free time evolution and finally interaction with probe pulse. The laser polarization is indicated with the red arrows and the vibration of the molecules with black shadows. Molecules that have been transferred out of a certain state are grayed out. The arrows illustrates which molecules with which orientation can undergo a certain transition for a given laser polarization.

explanation why the latter peak is not visible in experiments with mutually parallel polarizations can be given from Franck-Condon arguments. The transition dipole matrix elements at the center wavelength employed here favour the transition from the $A^1\Sigma_u^+$ state to the $2^1\Pi_g$ state over the transition from the $X^1\Sigma_g^+$ ground state to the $A^1\Sigma_u^+$ state. Thus, essentially all population that can be transferred to $2^1\Pi_g$ with two identically polarized laser pulses is already depleted after the first step. The remaining $A^1\Sigma_u^+$ population which vibrationally oscillates is not visible to the probe pulse due to the selection rule. Therefore, no $A^1\Sigma_u^+$ dynamics can be seen in Fig. 5.5 (left graph). In order to illustrate which

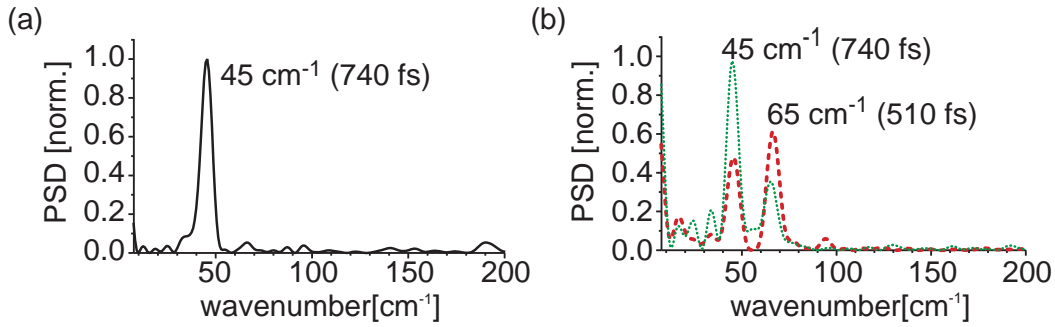


Figure 5.5: FFT-analysis of pump-probe transients with parallel (left graph) and perpendicular (right graph) mutual polarizations. The numbers in brackets indicate the vibrational period of the associated wave-packet motion. The FFTs have been performed over time periods from -4 ps to 0 ps for perpendicular polarizations (b) (negative delays, dotted green line), 0 ps to +4 ps for perpendicular polarizations (b) (positive delays, dashed red line) and 0 ps to +3 ps for parallel polarizations (a) (solid black line, identical at negative delay times).

molecules with which orientation can be transferred by the pump or probe laser pulse to a certain state a diagram of these dynamics is given in Fig. 5.4a for the case of parallel polarizations. On the other hand, if the second pulse is polarized perpendicular to the first one, it can effectively drive the remaining $A^1\Sigma_u^+$ population into the final $2^1\Pi_g$ state because it has the correct orientation with respect to the molecular axis. So, the pump-probe transient for mutually perpendicular polarizations shows additional dynamics. This can also be seen, if the right column of Fig. 5.4b is compared to the corresponding one of Fig. 5.4a. The different relative contributions of $A^1\Sigma_u^+$ and $2^1\Pi_g$ for negative versus positive delay times (Fig. 5.5, dotted line and dashed line respectively) can be explained by partial alignment of the K_2 molecules.

The results of these pump-probe measurements show that the polarization state of ultrashort laser pulses is an important parameter in light-induced molecular dynamics. Depending on the polarization sequence, different states can be selected for intermediate wave-packet propagation. Note that all other experimental parameters in the two cases of Fig. 5.3 and 5.5 were identical (pulse intensities etc.) so that the differences in the observed transients are entirely due to light polarization properties. This type of polarization sensitivity can then be exploited even in much more generality in connection with adaptive femtosecond laser pulse shaping, providing a qualitatively novel mechanism for the control of quantum systems. In the following, flexible and automated polarization and phase shaping of femtosecond laser pulses is used in combination with an evolutionary algorithm to control molecular dynamics and, in this case, maximize ionization of K_2 .

5.3 Quantum Control of K_2

For this purpose, the experimental setup is complemented by a polarization pulse shaper and a computer with the optimization algorithm, as described in the previous chapter on the adaptive “clean up” of a polarization distortion. Only for this experiment the pulse shaper is realigned for the broader spectrum of the 30 fs laser pulses with a center wavelength of 785 nm used here. As mentioned in Chapter 4.1.1 conventional phase-only pulse shaping can be realized, if the same phase function is applied to both LCD layers. Therefore, without any mechanical realignment optimizations both with linearly polarized shaped pulses and with polarization modulated pulses can be performed. In the optimization experiment shaped 300 nJ laser pulses are used instead of the unshaped pump and probe laser pulses with 150 nJ each. Hence both experiments are carried out in the same intensity regime and strong field effects are avoided.

Two types of adaptive control experiments are performed to maximize the K_2^+ yield: spectral polarization-and-phase laser pulse shaping as well as phase-only shaping. In both cases the same number of free parameters is optimized and the two strategies are run in a parallel implementation. This ensures identical experimental conditions, i.e. in terms of laser pulse energy and molecular beam parameters, allowing one to compare the results directly. The evolution of the K_2^+ signal as a function of generation number within the evolutionary algorithm is shown in Fig. 5.6. The increase for phase-only pulse shaping (solid circles) is due to the adaptation of the laser pulse structure to the vibrational dynamics of the potassium dimer, providing high laser intensities when the wave packet is in a suitable Franck–Condon region. This general type of mechanism is what had been exploited and discussed in the theoretical and experimental literature on quantum control to date.

However, when the additional mechanism of light-polarization control is used (open circles), one can go beyond the limitations set by linearly polarized fields and achieve significantly higher product yields. This demonstrates not just a quantitative improvement, but rather a qualitative extension of quantum control mechanisms, because it goes beyond one-dimensional addressing of transition dipoles and rather makes use of their directional properties by shaping the polarization state of the controlling laser pulse.

Figure 5.7 shows a representation of the best laser pulse shape reached in the final generation of the polarization optimization. The momentary frequency and the polarization state of the optimized pulse changes substantially in a complex fashion as a function of time. Some reasons for this complexity are now briefly discussed. First, the detection step in this experiment (i.e., the ionization) needs to be considered in more detail. Observation of $2^1\Pi_g$ state dynamics in the pump–probe measurement (Fig. 5.3 and 5.5) proves that ionization from the $2^1\Pi_g$ state is dependent on the internuclear distance and occurs predominantly at the outer turning point [150]. Ionization, for example, can occur via doubly excited,

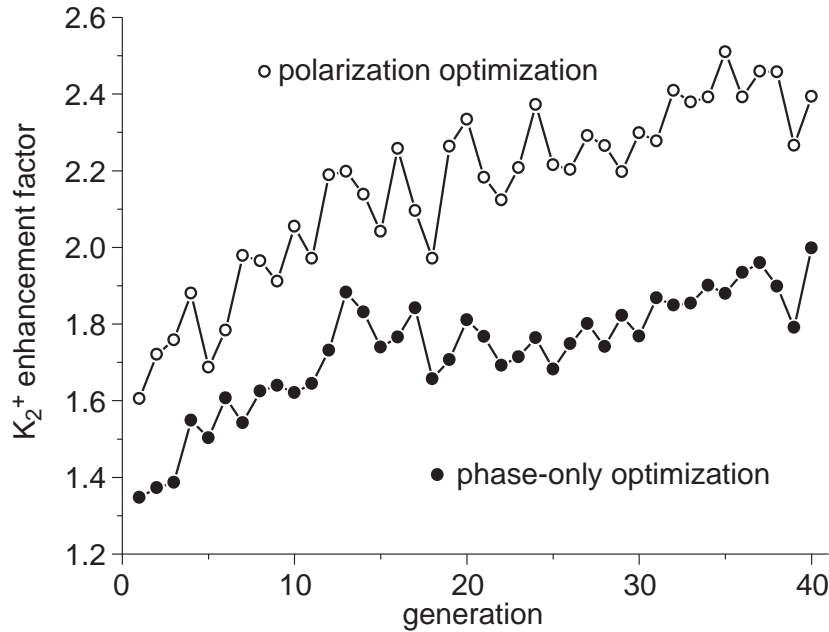


Figure 5.6: Evolution curves showing the K_2^+ ion yield relative to that obtained with an unshaped laser pulse. The best individual of each generation for the polarization optimization (open circles) and phase-only optimization (solid circles) is plotted.

autoionizing states [154]. Excitations of these doubly excited states via the outer turning point in the $2^1\Pi_g$ state as well as transitions involving the $4^1\Sigma_g^+$ state have not been considered in the previous simplified discussion. Another reason for the complicated pulse structure is the broad spectrum of the ultrashort laser pulse. The vibrational dynamics of the potassium dimer are known to depend strongly on the center frequency of the excitation laser pulse [150]. In this experiment that means that the optimized polarization needs to be provided for a wide distribution of frequencies and timings.

Another complicating factor can be seen in Fig. 5.8. It shows an example of an optimal polarization-shaped laser pulse from a series of optimizations, where the molecular beam conditions are different. The seed gas Ar of the molecular beam is heated up to approximately 150 °C. Under these conditions the partial alignment effects in the pump-probe measurements vanish and the vibrational temperature of the K_2 is expected to have increased. If one now compares this optimal pulse to the one with the “cold” molecular beam, the pulse shapes are remarkably different. This cannot be attributed to statistical variations of the pulse shape in different optimizations, because also with the “cold” molecular beam several optimizations were performed and the optimal pulse shapes are more or less similar to the one shown in Fig. 5.7. Therefore, this is an indication that the optimal pulse shape depends on the molecular beam conditions. Interestingly, the pulse shapes with the “hot” molecular beam resemble much more the expectation

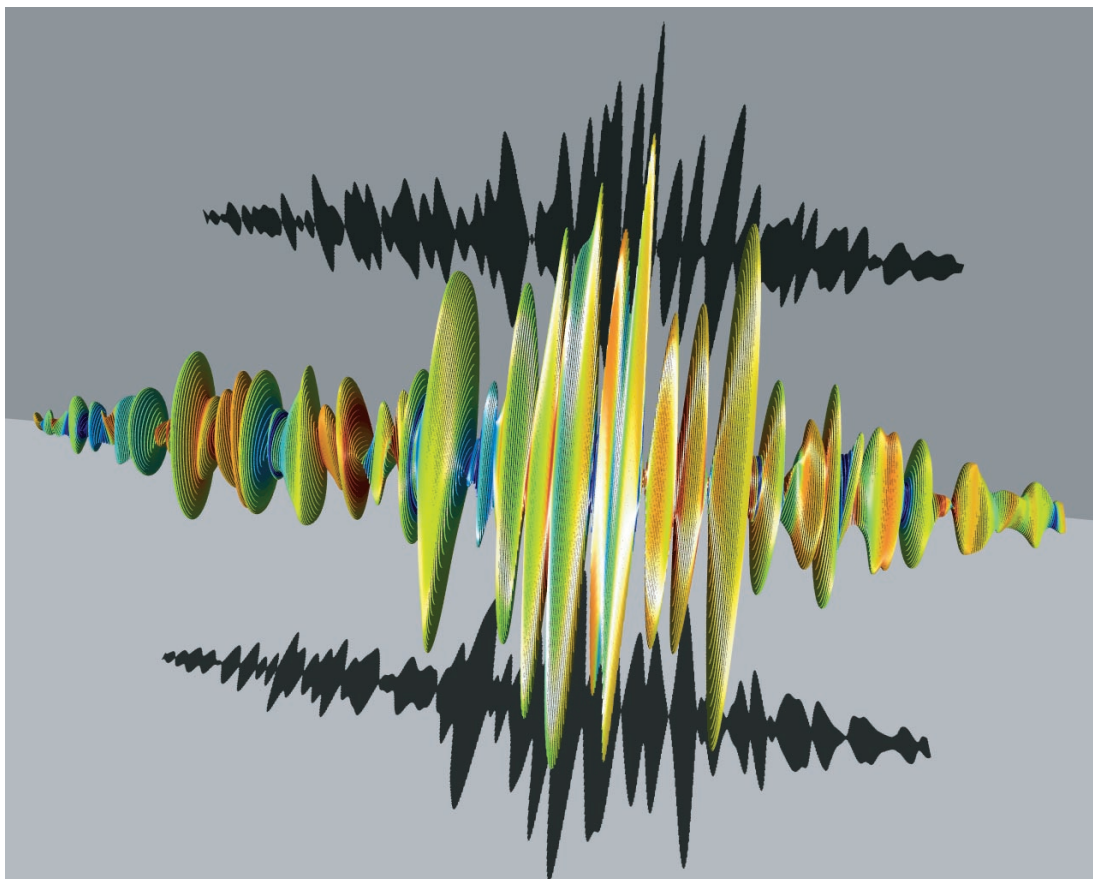


Figure 5.7: Quasi-three-dimensional representation of the optimal polarization-shaped laser pulse. Time evolves from -1.5ps (left) to $+1.5\text{ps}$ (right), and electric field amplitudes are indicated by the sizes of the corresponding ellipses. The momentary frequencies are indicated by colors; and the shadows represent the amplitude envelopes of the two orthogonal components parallel to the shaping directions of LCD layers.

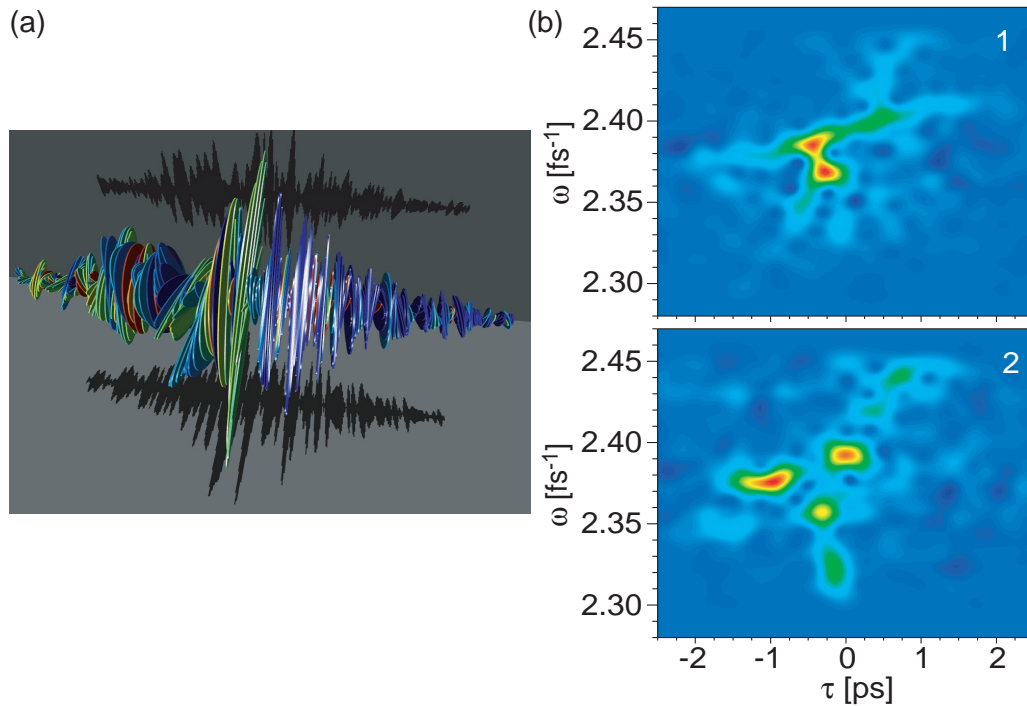


Figure 5.8: Optimal polarization-shaped laser pulse with “hot” molecular beam. (a) shows the optimal pulse in the quasi-three-dimensional representation and (b) shows the Husimi distributions of the 1- and 2-polarization component of the same pulse. The two Husimi plots display some indications for the simple pulse sequence with varying linear polarizations discussed in the simple model given in Section 5.2.

from the simple model given in Section 5.2, i.e. a pulse sequence with varying linear polarizations. However, without a detailed calculation and simulation of the interaction between the optimal field and the K_2 dimer one has to refrain from speculations about the underlying control mechanism.

While all these factors complicate the analysis and interpretation efforts of the optimal pulse shape, the important point is that despite the complexity an optimized electric field with time-varying polarization indeed has been exploited by the evolutionary learning algorithm as a novel control agent.

5.4 Conclusion

In conclusion, one can say that it has been demonstrated that time-dependent shaping of femtosecond light polarization can give access to a further level of control in quantum systems. Pump-probe measurements with different linear polarizations show how a time-dependent polarization can give access to dynamics on additional states. Comparative optimizations of K_2^+ yield show that polarization laser pulse shaping is superior to phase-only shaping, because the vectorial

electric field can adapt to the time evolution of the polarization-dependent transition dipole moments. Hence the vectorial properties of light–matter interaction have been exploited to achieve quantum control in a molecular model system. This opens the door to a number of new experimental schemes, which exploit the full vectorial temporal response of quantum systems. This allows to address stereochemical aspects in quantum control such as chiral selectivity, where polarization–shaped laser pulses are a crucial ingredient. The optical control of lattice vibrations [155] and the generation and characterization of attosecond light pulses [64, 65] are further examples of numerous new perspectives.

6 Optimal Control of Photoisomerization

The previous chapters have dealt with the three-dimensional aspects of shaped laser pulses. In this chapter the three-dimensional aspects of the controlled quantum system are investigated. The large scale motion of complex molecular groups is detailed with special emphasis on *cis-trans* isomerization in Section 6.1. In the next section, the ultrafast photoisomerization dynamics of 3,3'-diethyl-2,2'-thiacyanine iodide (NK88) are presented as a basis for the optimal control of these dynamics in Section 6.3.2. The possible influence of polarization on the isomerization process is discussed in Section 6.3.1 and a possible scheme for polarization-shaping is suggested.

6.1 Introduction

Over the last decade, remarkable theoretical and experimental progress has been achieved in the field of optimal control of chemical reactions [2, 36, 37, 40, 138]. In this multi-parameter control scenario, shaped femtosecond laser pulses, which are best suited for solving the control task, are found by the quantum system itself in an automated iteration loop. In this approach no a-priori knowledge of the molecular Hamiltonian is required. Therefore, the method is also applicable in the liquid phase, where interactions with the solvent molecules increase the complexity. Up till now, none of the liquid-phase control experiments [36, 37, 39, 40] have tried to control the modification of the molecular geometry. In this context, *cis-trans* isomerization [28, 156–159] has attracted much attention because of its importance in chemistry and biology (e.g. primary step of vision) [160, 161]. The control of isomerization reactions, on the other hand, is also of fundamental theoretical interest. Since the successful modification of the molecular structure can be regarded as a further step towards controlled stereoselectivity in photochemistry, for example the selective conversion between enantiomers [46, 49].

An intensely investigated class of molecules that exhibit *cis-trans* isomerization are symmetrical cyanines (for a summary see reference [162]). The molecule investigated in this experiment, 3,3'-diethyl-2,2'-thiacyanine iodide (NK88), belongs to the group of cyanines with a short polymethine-chain. The isomeriza-

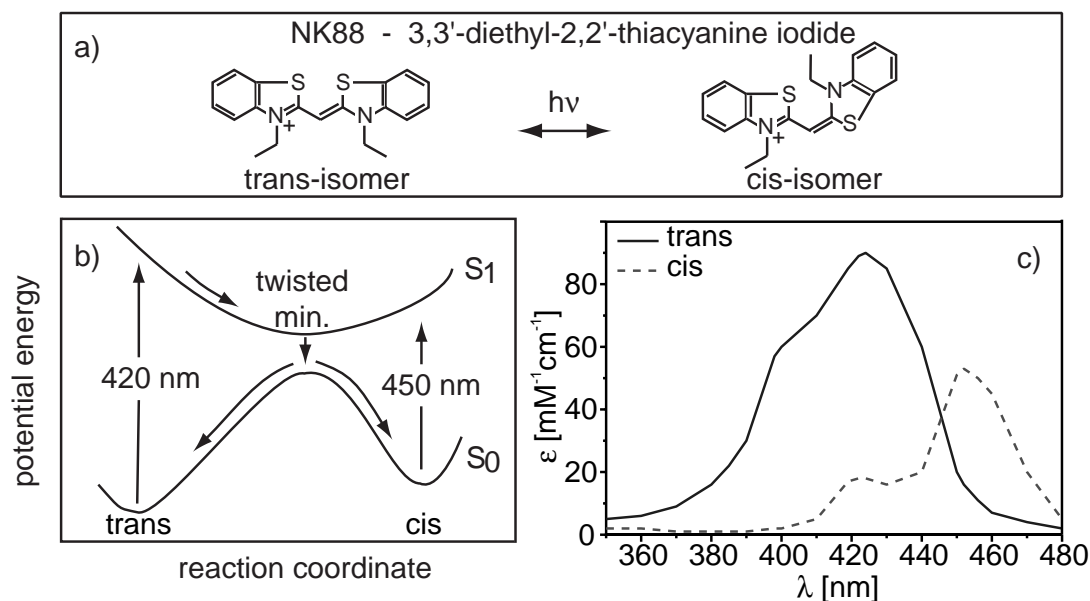


Figure 6.1: (a) Molecular structure of the two isomer configurations of the cyanine dye NK88. Irradiated by light of the proper wavelength, this molecule can undergo *trans-cis* isomerization. (b) Simplified potential energy surface. The reaction coordinate is the twist angle about the $C=C$ double bond. (c) The ground-state absorption spectra of the two isomers. While the *trans*-isomer shows a broad ground-state absorption centered at 420 nm, the absorption band of the *cis*-isomer is redshifted with its maximum around 450 nm.

tion process of this type of cyanines is well investigated and understood [163–165], which makes them an ideal system for studying optimal control of *cis-trans* photoisomerization. And thereby the control of structural changes of molecules can be investigated as well. The cyanine molecule NK88 exists in a *trans*- and in a *cis*-configuration (Fig. 6.1a). Investigations of similar cyanines with NMR-spectroscopy in solution [166, 167] and X-ray analysis of the crystal structure [168, 169] have shown that the thermodynamically stable isomer of these molecules has a *trans*-geometry. Quantum-chemical calculations [170] of the absorption maxima for the two isomers in comparison to the experimentally observed ground-state spectrum show that this also applies to the NK88-isomers. Under room-temperature conditions the concentration of the unstable *cis*-isomer is negligible. This can be seen by comparing the measured ground-state absorption spectrum of the dissolved NK88 to the available literature-spectra for both isomers (see Fig. 6.1c or Ref. [162]). Only the features of the *trans*-spectrum can be seen in the measured spectrum. The observed time constant (≈ 0.6 ns) of thermal backreaction of the unstable *cis*-isomer also agrees with this finding.

The ground-state absorption spectra of the two isomers, which are taken from Ref. [162], are shown in Fig. 6.1c. While the *trans*-isomer has a broad ground-state

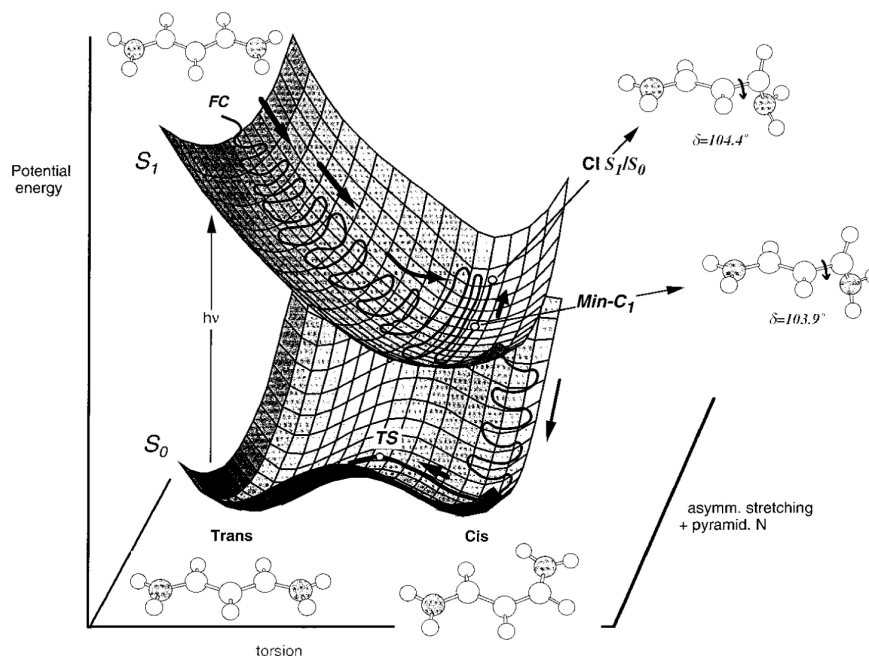


Figure 6.2: Calculated potential energy surfaces for short-chain, symmetrical cyanine. The two reaction coordinates for *trans-cis* isomerization are the twist about the $C = C$ double bond and a asymmetric stretching mode. Figure is taken from [164].

absorption around 420 nm, the absorption band of the *cis*-isomer is redshifted with its maximum at 450 nm. This situation where the absorption spectra of the two photoproducts are clearly separated in the visible wavelength range is a rather unusual situation for *cis-trans* isomers. Very often the absorption spectra show very broad features that overlap to such a degree that the isomers cannot be identified from the spectral information alone. One has to consider the spectral and temporal changes in the transient absorption measurements together in order to identify the signals belonging to the respective isomers. Since in an adaptive control experiment many different pulse shapes need to be tested and the reaction yield of *cis* to *trans* isomers has to be ascertained for every pulse shape, a relatively fast measurement for the reaction yield is essential. Therefore, the separated absorption spectra of the NK88 isomers make this system an ideal candidate for an adaptive control experiment.

As shown in Fig. 6.1b, a simplified scheme for the photoisomerization process of the short-chain, symmetrical cyanines assumes only one reaction coordinate, namely the twist about the $C=C$ double bond. This simple model views the shape of the ground-state energy surface as a double-minimum potential. Calculations and experiments by the Sundström group indicate the first excited state to be barrierless for this type of cyanines [163]. A more detailed model of the potential energy surfaces includes as a second reaction coordinate the skeletal stretching of

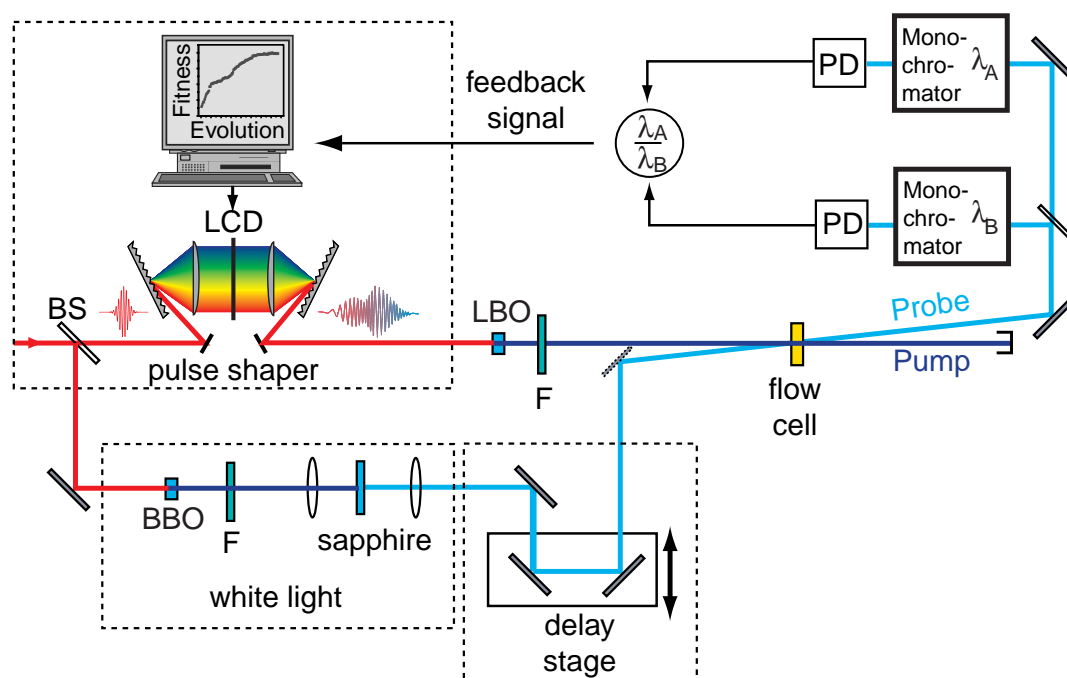


Figure 6.3: Experimental setup for photoisomerization of NK88. For the measurement of the dynamics the pulse shaper is set at zero spectral phase and the delay is varied. For the optimal control experiment, on the other hand, the delay is fixed at 20 ps and the pulse shaper is controlled by the evolutionary algorithm. The abbreviations in the figure are as follows: beam splitter (BS), nonlinear optical crystals Beta Barium Borate (BBO) and Lithium Triborate (LBO), short wave pass BG40 glass filters (F) and photodiodes (PD).

the molecule [164]. The potential energy surfaces calculated for a related short-chain, symmetrical cyanine are shown in Fig. 6.2. The driving motion of the isomerization is the excitation of the bonding π -state into the antibonding π^* -state. Thus, the absorption of a 400 nm photon transfers the stable *trans*-isomer from the ground state to the first excited state S_1 . From this state, it reaches a twisted molecular configuration. Through a conical intersection it can either relax back to the *trans*- or to the *cis*-ground state.

6.2 Photoisomerization Dynamics of NK88

In order to measure and control the isomerization reaction, the regenerative amplifier laser system is employed, which delivers pulses with a duration of 80 fs, a pulse energy of up to 1 mJ at a center wavelength of 800 nm and at a repetition rate of 1 kHz. For the pump pulse 50 μ J are split off and shaped using frequency-domain pulse shaping. The pulse shaper is the one described in Chapter 3.2.1. The whole experimental setup is shown in Fig. 6.3. The phase-shaped 800 nm

femtosecond laser pulse is then frequency-doubled in a 400 μm LBO crystal. The resulting laser pulse at 400 nm is therefore shaped in spectral phase and amplitude (see Chapter 3.2.2). The maximum pulse energy of the second harmonic at 400 nm is 1.5 μJ with a pulse duration of 100 fs for a bandwidth-limited 800 nm fundamental laser pulse. The shaped 400 nm pump pulse is then focused into a 200 μm thick flow cell where the sample (optical density $OD = 0.3$), dissolved in methanol, is constantly exchanged by means of a peristaltic pump (MasterFlex L/S from Cole Parmer). For the probe laser pulse about 50 μJ of the unshaped 800 nm laser pulse are taken and frequency-doubled in a 300 μm BBO crystal. The resulting 400 nm laser pulse is employed to generate a chirped supercontinuum by focusing into a sapphire disk. The generated white-light laser pulse is delayed in a computer-controlled delay stage and focused into the sample under an angle of about 10° with respect to the pump laser beam. The polarization between pump and probe laser beams is set at the magic angle (54.7°). The white-light probe laser beam is split into two light beams after passing through the flow cell and these are sent to separate monochromators. This allows the simultaneous acquisition of transient absorption spectra at two distinct wavelengths. For better signal-to-noise ratio the pump beam is synchronously chopped at half the laser repetition rate with a mechanical chopper (not shown in Fig. 6.3). The signal of the probe beam in the two amplified photodiodes (HUV-1100BQ from Laser Components) is recorded by two boxcar integrators (SR250 from Stanford Research Systems) and after analog-to-digital conversion the computer takes the difference from two subsequent laser shots, i.e. it computes the difference in probe light, when the pump is on, as compared to when it is blocked.

The overall spectrally resolved dynamics are plotted in Fig. 6.4a as a function of the probe wavelength and the time delay between the pump (400 nm, unshaped) and probe pulse. There the z axis ($\Delta T/T$) of the contour plot describes the change in transmitted probe light normalized to the transmission without the pump laser. In this figure red denotes a high transmission through the sample, whereas blue marks the absorption of the probe beam. The region between 400 and 430 nm corresponds to pump-depletion and reflects the decrease of concentration of the *trans*-isomer in its ground state. On the other hand, the pump-probe signal in the region around 460 nm, after a pump-probe delay time of a few picoseconds, originates from the absorption of the *cis*-isomer ground state.

For large delay times the pump-probe transients recorded at 400 nm and 460 nm (shown in Fig. 6.5) are mainly affected by one of the two isomers respectively. The pump-probe signal at 400 nm for larger delay-times is proportional to the amount of *trans*-molecules, which were initially excited, while the curve at 460 nm measures the fraction of molecules that actually undergo *trans-cis* isomerization. The ratio of the probe signals $\Delta T(460\text{nm})/\Delta T(400\text{nm})$ therefore directly reflects the isomerization efficiency (i.e., quantum yield). The more complicated dynamics at early pump-probe delay times originate from stimulated emission and absorption of the probe-laser pulse to higher lying electronic states.

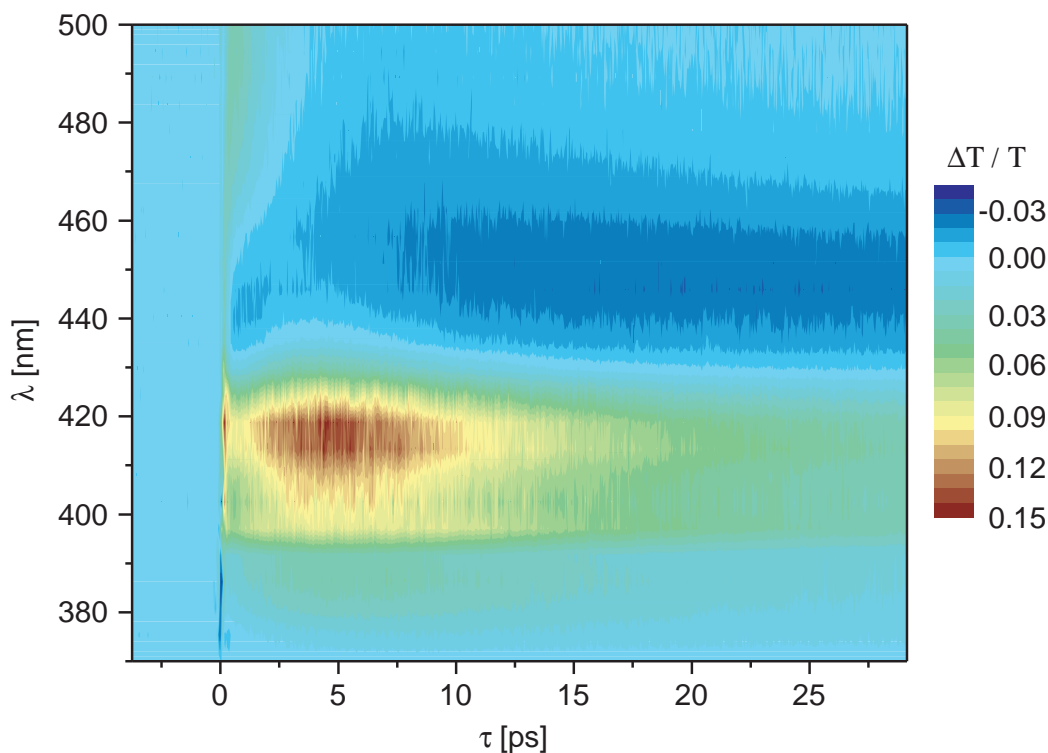


Figure 6.4: Spectrally resolved pump-probe transients. The z-axis ($\Delta T/T$) of the contour plot describes the change in transmitted probe-light normalized to the transmission without the pump-laser. While red denotes a high transmission through the sample, blue marks the absorption of the probe-beam.

The curve at 400 nm at early times consists mainly of two components. One is the pump depletion and therefore reduces the absorption of the probe laser pulse. The other is excited state absorption from the S_1 to the S_n manifold and attenuates the probe laser pulse. The superposition of these two exponentials with their different time constants and different amplitudes (of opposite sign) gives the rather peculiar curve for pump depletion. Ideally, one would expect the pump depletion signal to rise on the timescale of the pump pulse duration, but the fact that the excited state absorption coincides with the ground state absorption in photon energy leads to the observed more complicated curve. The transient absorption at 460 nm contains several processes at early times, inter alia stimulated emission of the excited molecule and the rise of ground state absorption of the built *cis*- isomer. However, the complicated dynamics at early times are not fully understood yet in the spectral region around 460 nm. Further experiments and a cooperation with theory is necessary for further progress in their understanding. Nevertheless, the signals at later times, i.e. after 5 ps, are well understood and can be used to derive a feedback signal for an adaptive control experiment of photoisomerization.

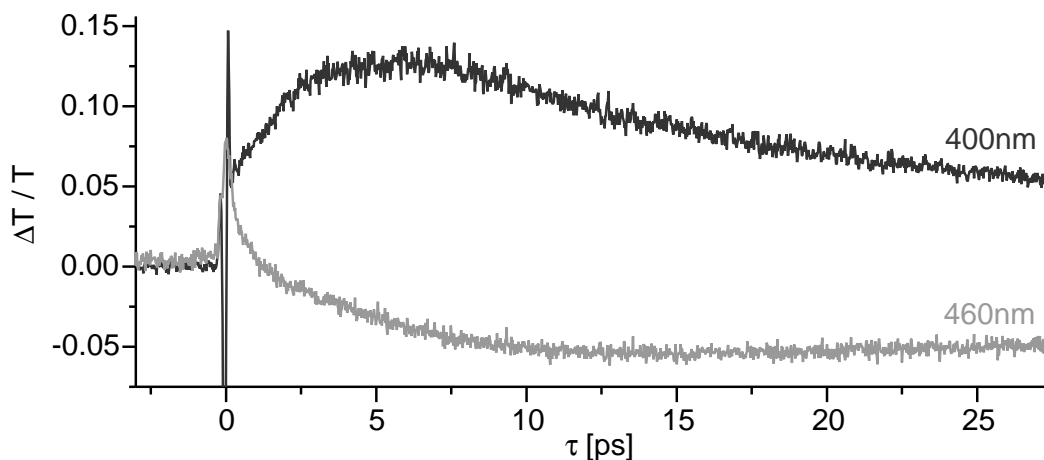


Figure 6.5: Pump-probe absorption transients recorded with 400 nm pump and 460 nm as well as 400 nm probe wavelengths. Both transients are at large delay times of 20 ps mainly affected by one isomer only and show a very small slope at this delay position.

6.3 Quantum Control of NK88

6.3.1 Polarization-Shaping Scheme for NK88

The possible influence of polarization on isomerization dynamics was already emphasized in Chapter 2.2.1. Since large molecular groups move during this process and their electronic orbitals with them, it is expected that the transition dipole moments change their spatial direction as the molecule twists from the *trans* to the *cis* configuration. Polarization-shaped laser pulses would allow to follow these dynamics also in the spatial direction. Polarization-shaping, however, is up to now limited to the transparency range of the liquid crystal molecules. As already mentioned in Chapter 3.2, this reduces the availability of polarization-shaped laser pulses to the visible and near-infrared wavelength region. The molecule under investigation here, on the other hand, absorbs in the near-UV and two-photon absorption is so small that it is below the sensitivity of the current setup and laser system. Also the higher intensities needed for two-photon absorption lead to undesirable, non-resonant effects in the solvent like white light generation. Although this is a $\chi^{(3)}$ process and depends in third order on the electric field amplitude, due to the much higher particle density of solvent as compared to solute molecules it still produces enough light to disturb the measurement of small transient absorption changes.

Therefore, frequency conversion of the polarization-shaped laser pulses is the only option. However, this cannot be achieved by simply replacing the phase-only shaper in the setup (see Fig. 6.3) with the polarization shaper. The reason for this lies in the SHG step, since a nonlinear crystal with type-I phase matching acts

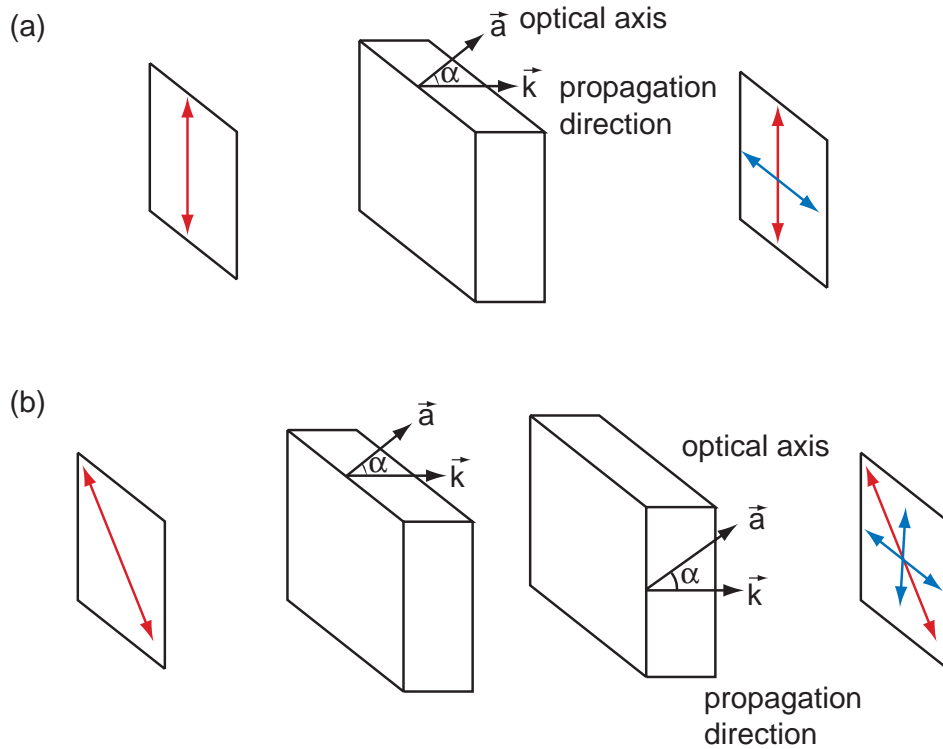


Figure 6.6: Polarization-shaping at 400 nm. In conventional type-I SHG (a) the fundamental is polarized (direction indicated by red arrow) as the ordinary wave (polarized perpendicular to optical axis) and the resulting second harmonic as extraordinary wave. For frequency-doubled polarization shaping (b) one component of the fundamental is doubled in the first crystal whereas the other passes the first crystal undergoing only material dispersion and is then frequency-doubled in the second crystal. The orientation of the crystals is shown on their side faces by the direction of the optical axis \vec{a} , where \vec{a} and \vec{k} lie in the plane of the respective side face.

as a polarizer. Only fundamental light that is polarized as the ordinary wave is phase matched (i.e. $n_o(\omega) = n_{eo}(2\omega)$) to the second harmonic, which is polarized as the extraordinary wave. This scenario is depicted in Fig. 6.6a. Here parts of the fundamental laser pulse which are polarized as extraordinary wave are not phase matched and therefore are not frequency doubled. This part undergoes just linear material dispersion and leaves the crystal otherwise unchanged.

In order to achieve polarization-shaped SHG pulses two nonlinear optical crystals are necessary. Their orientation with respect to each other and the incoming laser polarization is shown in Fig. 6.6b. In principle, the first crystal acts on one component (in the figure here the vertical one) of the fundamental and the second crystal on the other one. If the incoming laser polarization is under 45° with respect to the two ordinary polarization directions of the two crystals, they both see equal components of the fundamental field and a linearly

polarized SHG pulse is produced. But here two perpendicular components of the fundamental contribute to the SHG. Therefore, polarization-shaped laser pulses can be frequency-doubled without losing the polarization modulation. The situation here is somewhat similar to the working principle of the polarization shaper (see Chapter 4.1 and in particular Fig. 4.2), where one LCD layer phase modulates one component and the second layer the perpendicular component.

However, even more than in the case of frequency-doubling laser pulses which are phase-only shaped, characterizing the fundamental pulse shape is not sufficient to know the resulting second harmonic pulse shape. This is due to the fact that small errors in characterization of the fundamental can lead to rather different calculated second harmonic pulse shapes. Therefore, one has to develop a new pulse characterization technique. An idea would be to use a frequency-doubled reference pulse, to characterize it via XFROG and then to perform a spectral interferometry measurement with the shaped laser pulse. Apart from this experimental challenge, there is also the problem that the energy throughput of the polarization shaper is very low as compared to the phase-only shaper. In order to have sufficient pulse energy for the polarization-shaped pump pulse, for the reference pulse used in the characterization and for the probe pulse employed in the transient absorption measurement the optical setup of the polarization shaper would need to be improved, as suggested in Chapter 4.2.2, with VPH gratings. Although the prospects of polarization-shaping for the control of *cis-trans* isomerization are very tempting, the experimental challenges are formidable. Thus in the following, linearly-polarized shaped laser pulses are employed to control the isomerization reaction.

6.3.2 Optimal Control of NK88

The goal of this experiment is to demonstrate that adaptive femtosecond pulse shaping is able to control the *cis-trans* isomerization of a complex molecule in the liquid phase. As already discussed above, the pump pulse is sent through a femtosecond pulse shaper capable of producing complex laser pulse shapes by spectral phase modulation. An automated "learning loop" is then employed, wherein an experimental feedback signal from the physical system under investigation guides the evolutionary algorithm to find laser fields optimized for the control task at hand. In this experiment, the ratio of *cis*-isomers in its ground state after the photoisomerization process to the amount of initially excited *trans*-isomers (i.e. the relative reaction yield) is chosen as feedback signal. To determine these quantities, the transient absorption signal is recorded at the two wavelengths 400 nm and 460 nm at a given specific pump-probe delay time. The pump-probe delay time during the optimization experiment was set to 20 ps, because both transients show only small changes at this large delay time. The ratio between the two signals can only negligibly be changed by the time-shifts achievable with tailored pump pulses. Additionally, an appreciable influence of stimulated emission or

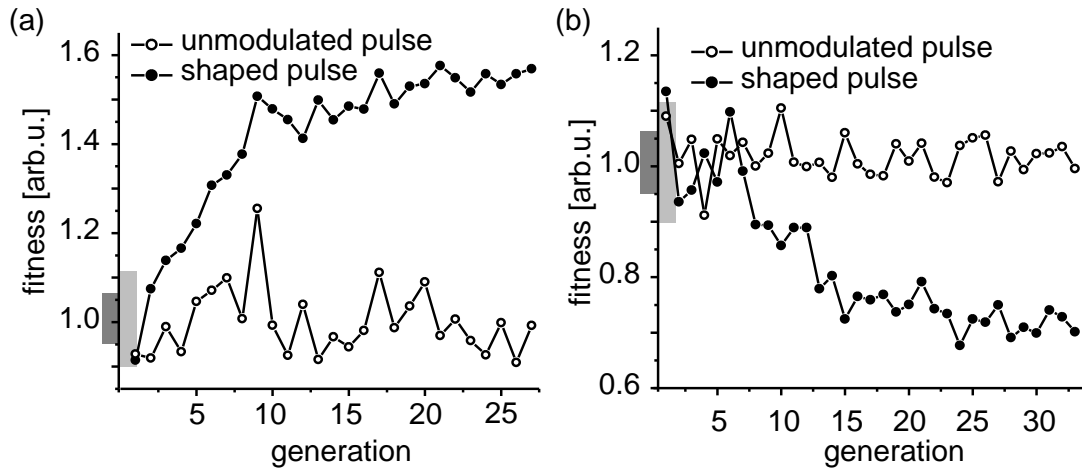


Figure 6.7: (a) Maximization and (b) Minimization of the *cis/trans* ratio as a function of iterations using an evolutionary algorithm. The filled dots represent results obtained with shaped laser pulses and the open dots show the reference signal obtained with an unshaped laser pulse. On the y-axis of both graphs the achievable ratio changes for the single parameter control schemes of intensity (dark gray, ratio for all intensities within 1.009 ± 0.058 (2σ width)) and quadratic spectral phase (light gray, ratio for all quadratic phases within 1.01 ± 0.11) variation are also shown.

absorption to higher lying states is limited to very early pump-probe delay-times and therefore is negligible at a pump-probe delay time of 20 ps.

By employing the automated learning loop, laser pulse shapes are found which enhance or suppress the isomerization reaction. The evolution of the *cis/trans* ratio as a function of generation number is shown in Fig. 6.7 for the two cases of enhancement and suppression of isomerization.

In case of maximization of the *cis/trans* ratio, that means the enhancement of the isomerization reaction, the evolution of the optimization is shown in Fig. 6.7a. In order to monitor the stability of the experimental conditions, an unshaped laser pulse is applied after each generation of the evolutionary algorithm. The *cis/trans* ratio for this is essentially constant over the time of the optimization (open circles). In contrast, the *cis/trans* ratio measured with modulated and optimized laser pulses clearly rises above that level as a function of generation number and finally converges to an optimum (solid circles). This shows the ability to increase the ratio between the amount of *cis*- to *trans*-molecules using adaptively shaped femtosecond laser pulses. On the other hand, the algorithm is also able to minimize that ratio (Fig. 6.7b). In that case, a laser pulse shape is found that reduces the isomerization efficiency. The optimized laser fields were characterized by the XFROG technique described in Chapter 3.3.1. This pulse characterization scheme is based on spectrally resolved crosscorrelation of the modulated 400 nm pulse and an unmodulated 800 nm reference pulse [108]. This

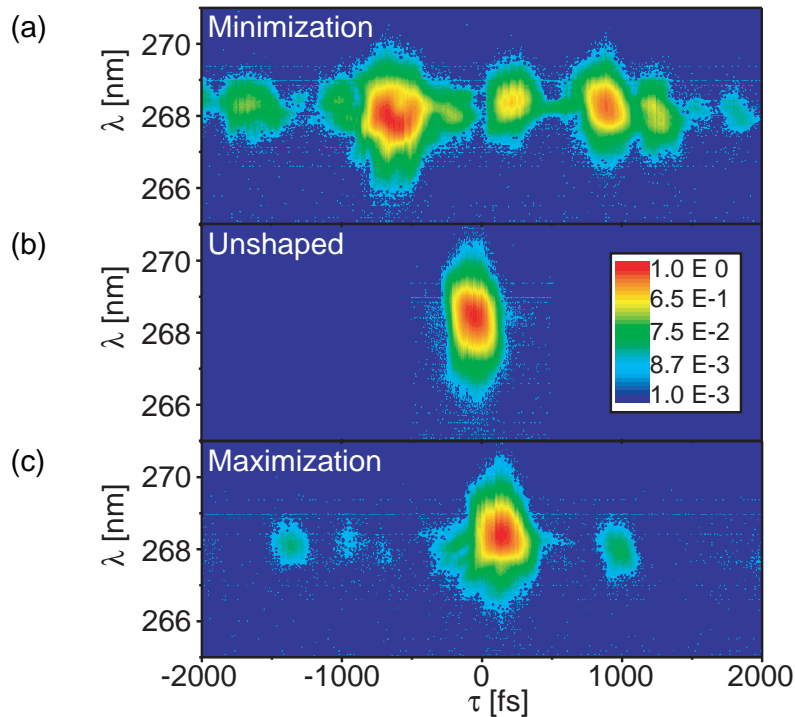


Figure 6.8: X-FROG traces of the optimal pulse shapes for (a) minimizing and (c) maximizing the ratio between the *cis*- and *trans*-isomer. For comparison the XFROG trace of the unmodulated pulse is shown in (b).

allows to characterize the shaped 400 nm laser pulse directly at the position of the experiment, i.e. the position of the flow cell. This is rather important since the dispersion of the used optical elements is more severe at 400 nm than in the visible or at 800 nm. The XFROG-traces of the optimized pulse shapes are shown in Fig. 6.8a for the minimization and in Fig. 6.8c for the maximization respectively. It is known that the potential energy surface of the excited state is barrierless and that the isomerization efficiency is quite high even for unmodulated pulses. In this context, one can see from Fig. 6.8c that in the case of maximization, only very little additional structure as compared to an unshaped laser pulse (see Fig. 6.8b) is needed to increase this efficiency even more. The complex shape in the case of minimization, however, indicates that a reduction of the isomerization efficiency involves a more complicated control scheme. The pulse train structure evident in Fig. 6.8a implies that minimization utilizes not only dynamics on the S_0 surface, but also in the S_n manifold. During the shaped pump pulse the wave packet would then be transferred by the individual pulses of the pulse train between the different potential energy surfaces in order to minimize the isomerization efficiency.

In order to check that these results cannot be obtained by employing “trivial” single-parameter control schemes, the effect of the variation of different pulse

parameters on the isomerization reaction is studied. First, the influence of varying the pulse energies of the pump-pulse is investigated. The ratio between the generated ground-state *cis*-isomers and the excited *trans*-isomers does not change for pump pulse energy variations by a factor of five. Another single-parameter variable frequently used in coherent control schemes is chirp. Under the given experimental conditions no significant change of the ratio between the generated ground-state *cis*-isomers and the excited *trans*-isomers was observed within the statistical uncertainty of 10% for varying the second order spectral phase from -7500 fs^2 to $+7500 \text{ fs}^2$. Both results of the single parameter variations are shown as bars in Figure 6.7a and 6.7b. Furthermore, in order to avoid that a very small *trans* excitation signal with low signal-to-noise ratio enters into the fitness function and thereby causes physically meaningless high values of the *cis/trans* ratio, a suitable discriminator is used as a lower threshold [171]. This discriminator is given by the lowest measurable denominator for the signal-to-noise ratio in this experiment. Hence the experimental results clearly demonstrate that optimally shaped femtosecond laser pulses can control the coherent motion of complex molecular groups.

6.4 Conclusion

To sum up, this experiment has demonstrated that adaptive femtosecond pulse shaping is able to control isomerization reactions of a complex molecular system in the liquid phase. By optimizing the ratio of the two isomers, this multi-parameter optimal-control experiment demonstrates that isomerization reactions can either be enhanced or reduced. As a basis for this optimization the ultrafast isomerization dynamic of NK88 were investigated using transient absorption. A suggestion how to employ adaptive femtosecond polarization control in this system was given using two differently orientated SHG crystals. The obtained optimization results show that adaptive femtosecond pulse shaping can be applied to many challenges in physical, chemical, and biological research where isomerization reactions are of vital importance. Especially, for the prospect of coherent control of chirality this experiment is rather encouraging, since the conversion of one enantiomer into the other also involves complex motion of molecular groups.

7 Summary and Outlook

Adaptive femtosecond quantum control has proven to be a very successful method in many different scientific fields like physics, chemistry or biology. Numerous quantum systems and in particular molecules undergoing chemical reactions have been controlled using shaped femtosecond laser pulses. This method allows to go beyond simple observation and to obtain active control over quantum-mechanical systems. It uses interference phenomena in the time and/or frequency domain to achieve selectivity. The shaped femtosecond laser pulses employed in this scheme have until recently been purely linearly polarized. Therefore, they only address the scalar properties of light-matter interaction and neglect the vectorial character of both the dipole moment $\vec{\mu}$ and the electric field $\vec{E}(t)$.

Especially in the quantum control of chemical reactions the investigated systems—the molecules—are three dimensional and exhibit complex spatio-temporal dynamics. With the help of polarization-shaped laser pulses one is now able to follow these dynamics in both, time and spatial direction, and can therefore reach a new level of control over quantum-mechanical systems.

In this work, the generation of polarization-shaped laser pulses has been implemented in an optical setup. It requires no interferometric stability as a result of the identical beam path for both polarization components. Dual-channel spectral interferometry was employed as experimental pulse characterization and a mathematical description of the time-dependent polarization state of these pulses was given. The polarization modulation of the shaped pulses by subsequent optical elements was investigated and some solutions to minimize these modulations were presented. Jones matrix calculus with experimentally calibrated matrices was implemented to account for all polarization distortions from the LCD to the position of the experiment and for full characterization of the generated pulse shapes.

Adaptive polarization shaping was demonstrated in a purely optical realization of the learning-loop concept. The learning algorithm was able to find the needed linear polarization in order to maximize second harmonic generation in a nonlinear optical crystal. The closed-loop configuration has proven to be capable to clear up more complicated polarization distortion, which was introduced using a multiple order half-wave plate designed for use at a wavelength of 620 nm. The additional deformation of the spectral phase through dispersion in a 10 cm long SF10 glass rod has also been compensated automatically.

After these optical demonstration experiments ultrafast polarization shaping was applied to control a quantum system. Polarization sensitivity was shown in pump–probe measurements of the multiphoton ionization of potassium dimer molecules K_2 . This sensitivity was exploited in a more general way in a learning–loop experiment with polarization–shaped laser pulses. A qualitatively new level of control was demonstrated using the time–dependent polarization state of laser pulses as an active agent. This polarization control was applicable even in randomly aligned molecules, which is a significant simplification of the experimental setup.

In addition to these polarization control experiments, the three dimensional dynamics of molecules were also investigated and controlled. The *cis–trans* photoisomerization of NK88 was studied in the liquid phase by transient absorption spectroscopy. The isomerization reaction efficiency was enhanced as well as reduced using linearly polarized laser pulses at 400 nm shaped in spectral phase and amplitude. This experiment demonstrates the ability to control the large scale motion of complex molecular groups with shaped femtosecond laser pulses.

The modification of the molecular geometry can be regarded as a first step towards control of chirality in photochemistry. Especially with the successful demonstration of polarization quantum control, which is required in the theoretical models for the selective conversion of one enantiomer into the other, the way is paved towards coherent control of chirality. Besides these fascinating applications of polarization shaping it should now also be possible to extend the wavelength range of these pulses. Apart from second harmonic generation in order to reach the ultraviolet region intra-pulse difference frequency generation could be an option to open the mid-infrared spectral range for polarization shaping. With these new wavelength regions numerous new perspectives arise for quantum control using polarization–shaped laser pulses.

Referring once more to the novel of Edwin A. Abbott presented in the introduction one could say that shaped femtosecond pulses really have left Flatland. Or to put it into the words of the sphere, when it teaches the square about the perception of dimensions:

“Look yonder [...] in Flatland thou hast lived; of Lineland thou hast received a vision; thou hast soared with me to the heights of Space-land;”

Edwin A. Abbott [1], 1884

8 Zusammenfassung und Ausblick

Adaptive Femtosekunden-Quantenkontrolle hat sich in den letzten Jahren als eine sehr erfolgreiche Methode in vielen wissenschaftlichen Gebieten wie Physik, Chemie oder Biologie erwiesen. Eine Vielzahl von Quantensystemen und insbesondere Moleküle, die eine chemische Reaktion durchlaufen, sind durch speziell geformte, Femtosekunden-Laserimpulse kontrolliert worden. Diese Methode erlaubt es, nicht nur das Quantensystem zu beobachten, sondern einen Schritt weiterzugehen und aktive Kontrolle über quantenmechanische Dynamik zu erlangen. In diesem Schema werden Interferenzphänomene im Zeit- und Frequenzraum benutzt, um Selektivität zum Beispiel in einer chemischen Reaktion zu erhalten. Die dazu benutzten, speziell geformten Femtosekunden-Laserimpulse waren bislang nur linear polarisiert. Deshalb konnten sie nur die skalaren Eigenschaften der Licht - Materie - Wechselwirkung ausnutzen und haben so den vektoriellen Charakter des elektrischen Dipolmoments $\vec{\mu}$ und des elektrischen Lichtfeldes $\vec{E}(t)$ vernachlässigt.

Im besonderen in der Quantenkontrolle von chemischen Reaktionen ist das untersuchte System, die Moleküle, dreidimensional und zeigt komplexe raumzeitliche Dynamik. Mit der Hilfe von polarisations-geformten Laserimpulsen ist man jetzt in der Lage dieser Dynamik, sowohl in der Zeit als auch in der räumlichen Richtung zu folgen. Deshalb kann nun ein neues Niveau an Kontrolle in quanten-mechanischen Systemen erreicht werden.

In dieser Arbeit konnte die Erzeugung von polarisations-geformten Laserimpulsen in einem optischen Aufbau verwirklicht werden. Dieser Aufbau erfordert keine interferometrische Stabilität, da beide Polarisationskomponenten demgleichen Strahlweg folgen. Zwei-Kanal spektrale Interferometrie wurde eingesetzt, um die Laserimpulse experimentell vollständig zu charakterisieren. Um den zeitabhängigen Polarisationszustand dieser Pulse exakt zu beschreiben, wurde eine mathematische Darstellung entwickelt und angewandt. Die Veränderungen des Polarisationszustandes durch optische Elemente wurde untersucht und einige Lösungen wurden aufgezeigt, um diese Veränderungen zu minimieren. Der Jones Matrix Formalismus wurde dazu benutzt, alle Verzerrungen des Polarisationszustandes zwischen dem Impulsformer und dem Ort des Experiments zu berücksichtigen. Zugleich können die Jones Matrizen zu einer vollständigen Charakterisierung der erzeugten Laserimpulse verwendet werden. Dabei wurden experimentell kalibrierte Matrizen eingesetzt.

Adaptive Polarisations-Impulsformung konnte in einem rein optischen Demonstrationsexperiment gezeigt werden. Dabei wurde die computergesteuerte Polarisationsformung mit einer Lernschleife und einem experimentellen Rückkopplungssignal kombiniert. Durch diesen selbstlernenden Algorithmus konnte der benötigte, linear polarisierte Laserimpuls mit möglichst kleiner Impulsdauer gefunden werden, der für die effektive Erzeugung der zweiten Harmonischen in einem nicht-linearen optischen Kristall am besten geeignet ist. Durch diese Rückkopplungsschleife war es möglich auch noch kompliziertere Polarisationsverzerrungen, die durch eine Wellenplatte für eine falsche Wellenlänge verursacht wurden, rückgängig zu machen. Die zusätzliche Verformung der spektralen Phase durch Materialdispersion in einem 10 cm langen Glasblock konnte ebenfalls automatisch kompensiert werden.

Nach diesen optischen Demonstrationsexperimenten wurde ultraschnelle Polarisationsformung angewandt, um ein Quantensystem zu kontrollieren. Die Polarisationsabhängigkeit der Multi-Photonen Ionisation von Kaliumdimeren konnte in einer Anrege-Abtast Messung nachgewiesen werden. Diese Abhängigkeit wurde dann in einem adaptiven Polarisationsformungsexperiment in einer sehr viel allgemeineren Art ausgenutzt. Statt nur einem Anrege- und Abtastlaserimpuls mit jeweils unterschiedlicher Polarisation zu benutzen, wurde der zeitabhängige Polarisationszustand eines geformten Laserimpulses benutzt, um die Ionisation zu maximieren. Anstelle von einer nur quantitativen Verbesserung konnte eine qualitativ neue Art von Kontrolle über Quantensysteme demonstriert werden. Diese Polarisationskontrolle ist anwendbar selbst bei zufällig ausgerichteten Molekülen. Durch diese Möglichkeit, auf Ausrichtung der Moleküle zu verzichten, konnte mit einem wesentlich vereinfachten experimentellen Aufbau gearbeitet werden.

Über diese Polarisationskontrollexperimente hinaus wurden auch die dreidimensionalen Aspekte der Dynamik von Molekülen erforscht und kontrolliert. Die *cis-trans* Photoisomerisierungsreaktion von 3,3'-Diethyl-2,2'-Thiacyanin Iodid (NK88) wurde in der flüssigen Phase mit transientser Absorptionsspektroskopie untersucht. Die Isomerisierungsausbeute konnte sowohl erhöht als auch erniedrigt werden durch den Einsatz geformter Femtosekunden-Laserimpulse mit einer Zentralwellenlänge von 400 nm, die sowohl in spektraler Phase als auch Amplitude moduliert waren. Dieses Experiment zeigt die Möglichkeit, die kohärente Bewegung großer molekularer Gruppen durch Laserimpulse gezielt zu beeinflussen.

Diese Modifikation der molekularen Geometrie kann als erster Schritt angesehen werden, kontrollierte Stereochemie zu verwirklichen. Insbesondere da im ersten Teil dieser Arbeit die Kontrolle von Molekülen mit Polarisations-geformten Impulsen gezeigt werden konnte, ist der Weg geebnet zu einer Umwandlung von einem chiralen Enantiomer in das andere, da theoretische Modelle dieser Umwandlung polarisations-geformte Laserimpulse benötigen. Außer diesen faszinierenden Anwendungen der Polarisationsformung sollte es nun möglich sein den Wellenlängenbereich der polarisations-geformten Laserimpulse auszuweiten. Sowohl Erzeugung der zweiten Harmonischen um in den ultravioletten Bereich

zu kommen als auch optische Gleichrichtung von äußerst kurzen Femtosekunden-Impulsen um den mittleren infrarot Bereich abzudecken sind Möglichkeiten, den Wellenlängenbereich von polarisations-geformten Laserimpulsen zu erweitern. Mit diesen neuen Wellenlängen tut sich eine Vielzahl an neuen Möglichkeiten auf, Polarisationsformung für die Kontrolle von quantenmechanischen Systemen einzusetzen.

A Control of Bond-Selective Photochemistry in CH₂ClBr

In this section the control of the bond-selective photodissociation/photoionization of CH₂ClBr in the gas phase by adaptive femtosecond pulse shaping is shown. With mass spectrometry as feedback an increase of 100% of the fission of the stronger versus the weaker carbon halogen bond is achieved (Section A.2). Haloalkanes are of particular interest to quantum control since they were one of first systems where bond-selective photochemistry by wavelength tuning was tried. Section A.1 gives a short overview over these experiments, before optimal control is employed in the CH₂ClBr system.

A.1 Bond-Selective Photochemistry in Haloalkanes

The idea that the coherent properties of light might be used as tools for selectively cleaving particular bonds in polyatomic molecules has attracted much attention. An early approach to this problem has involved wavelength tuning of narrow-band UV laser sources to excite electronic transitions to the dissociative continua of selective bonds. In this context, polyhaloalkanes (e.g. CH₂XY) have served as model systems because of electronic transitions in halogen atoms in which a non-bonding electron is promoted to a carbon-halogen antibonding orbital ($n(X) \rightarrow \sigma^*(C-X)$ or $n(Y) \rightarrow \sigma^*(C-Y)$). Successful application of this type of control has been demonstrated in the seminal work of Butler *et al.* on photoproduct distributions of gas-phase CH₂BrI [172]. In that work the excitation of the $n(\text{Br}) \rightarrow \sigma^*(\text{C-Br})$ transition at 210 nm resulted in exclusive fission of the stronger carbon-halogen (C-Br) bond while excitation to the red at 248 nm resulted in photoproduct distributions dominated by cleavage of the weaker C-I bond. While these studies were promising for wavelength control, the highly bond selective photochemistry observed for CH₂BrI makes it an interesting system for theoretical studies of coherent control [173]. Nevertheless, this high selectivity is not a general condition found in all polyhaloalkanes. In studies of CH₂ClBr with nanosecond laser radiation, excitation (248 nm, 234 nm and 268 nm [174–176]) results in exclusive dissociation (as expected) along the weaker carbon-bromine bond. How-

ever, excitation at 193 nm activates the cleavage of the stronger carbon-chlorine bond [174]. In contrast to CH₂BrI, cleavage of the weaker carbon-bromine bond still dominates the photochemistry at 193 nm. Such findings are also observed in studies of CF₂BrCl [177, 178] as well as CBrCl₃ [179–181]. These experimental results can be understood in the context of theoretical work on CH₂XY model systems [182], which shows that the loss of photoproduct specificity following excited state evolution (initiated with higher photon energy excitation) is a result of strong non-adiabatic coupling among competing dissociation channels.

The question that arises is how bond-selective photochemistry can be achieved in systems with highly coupled competing dissociation channels. A novel approach to achieve such selectivity is the use of coherent light sources to actively manipulate the outcome of light/matter interactions by exploiting interference phenomena in both the time and frequency domain [9, 183–186]. Specifically, femtosecond adaptive pulse shaping is applied in this experiment. This technique has been used to study a number of molecular systems in recent years [36, 37, 39, 138, 187]. The experiment reported here, however, is among the first to address bond selective photochemistry. That is to say, the bond broken in one channel is in any event preserved in the competing channel. The experiment reported here attempts to do just that using the model system CH₂ClBr.

A.2 Optimal Control of CH₂ClBr

The Quantronix laser system used in this experiment delivers pulses with a duration of 80 fs, a pulse energy of 1 mJ at a center wavelength of 800 nm and at 1 kHz repetition rate. Modulation of the femtosecond spectral/temporal laser pulse profile is achieved with frequency-domain pulse shaping as described in Chapter 3.2.1. The phase shaped femtosecond laser pulses are focused in an effusive molecular beam of the target molecules. This beam is prepared by expanding a room temperature liquid CH₂ClBr sample through a 60 μm nozzle at approximately 5 cm from the interaction region. CH₂ClBr was purchased from Merck EuroLab and used without further purification. The interaction of the shaped laser pulse with the parent molecules in the molecular beam, leads to different ionization and fragmentation processes. Cation mass spectra of the products are taken with a reflectron time-of-flight mass spectrometer (RETOF). The mass spectrometer is shown in Fig. A.1. The great advantage of RETOF mass spectrometers is the greatly enhanced mass resolution as compared to linear TOF mass spectrometers. The high resolution, even for heavy molecules with $m = 300$ amu, is achieved by imaging the first Wiley–McLaren spatial focus with a set of electrostatic lenses onto second one. In this way the field-free drift region can be significantly enhanced and the additional degrees of freedom introduced by the reflector inclination and additional electrode voltages allow for better compensation of TOF broadening effects [188]. Thus, a mass resolution $m/\Delta m$ of

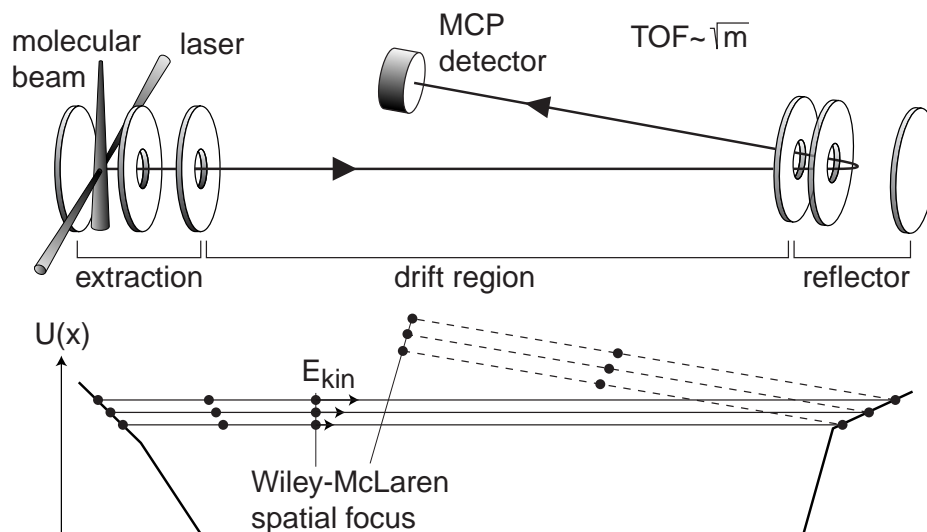


Figure A.1: Time-of-flight mass spectrometer. Laser beam and molecular beam are crossed in the interaction region where photoproducts are generated. Cations are extracted by static electric fields and separated according to their mass in a time-of-flight (TOF) spectrometer in reflectron geometry. Detection is achieved using microchannel plates (MCP). The accelerating voltages as a function of position are shown in the lower graph. Here also the position of the two Wiley–McLaren spatial foci is marked.

2000 at a molecular mass of 300 amu. It is therefore possible to assign single-mass-unit losses and isotope distributions even for the larger molecules used here. Further details of the experimental setup have been described in Ref. [189–191]. The laser pulse energy in the optimization experiments is about $230 \mu\text{J}$. This corresponds to an intensity of approximately $5 \times 10^{13} \text{ W/cm}^2$ in the focus of the laser. Simultaneously, for each laser pulse the SHG yield is recorded with a $100 \mu\text{m}$ thick BBO crystal using a small laser beam pick-off. Optimizations are run either on optimizing (i.e. maximizing) the ratio of the signals of two ionic fragments or on maximizing SHG. It has been shown before that maximizing SHG leads to a bandwidth limited laser pulse [87, 136].

Previous demonstrations of photodissociation control using femtosecond adaptive pulse shaping have relied on ionic mass fragment detection for implementation of feedback [138, 192]. The mass spectrum obtained for CH₂ClBr following multi-photon excitation using intense (ca. $230 \mu\text{J/pulse}$), bandwidth-limited 800 nm laser pulses is shown in Figure A.2a. It is normalized to the height of the CH₂³⁵Cl⁺ fragment. The mass spectra (Fig. A.2a, A.2b) show two major fragment ions corresponding to the loss of bromine in the dominant feature (CH₂Cl⁺) and loss of chlorine in the next prominent feature (CH₂Br⁺). In both cases the expected isotope pattern due to presence of the halogen is observed. In Fig. A.2b

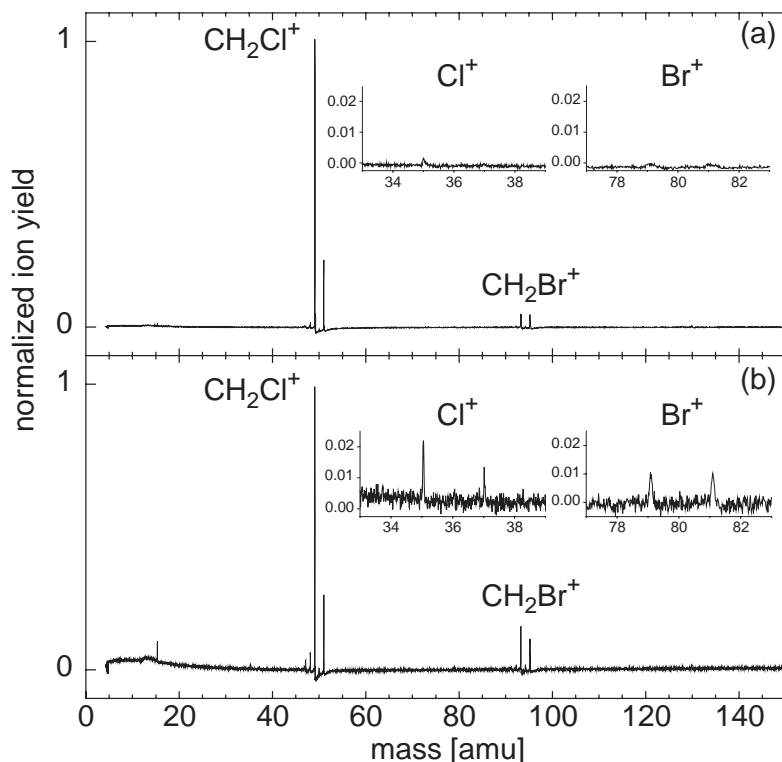


Figure A.2: Time-of-flight mass spectrum obtained for CH_2ClBr following multi-photon excitation with (a) a 80 fs bandwidth-limited 800 nm laser pulse ($\sim 230 \mu\text{J}/\text{pulse}$); (b) a phase shaped laser pulse found as the fittest individual of the last generation following maximization of the $\text{CH}_2\text{Br}^+:\text{CH}_2\text{Cl}^+$ ion ratio. The absolute yields are such that the CH_2Cl^+ fragment yield in (b) is about 6 times smaller than in (a). The insets in the plots show the signal of $^{35/37}\text{Cl}^+$, and $^{79/81}\text{Br}^+$, respectively, magnified by a factor of 40.

the mass spectrometer resolves in the vicinity of these ions small peaks one and two mass units lighter corresponding to CHX^+ and CX^+ , respectively ($\text{X}=\text{Cl},\text{Br}$). Moreover, in a blown up spectrum (not shown) minor contributions from CH_2^+ , CH^+ , and the parent molecular ion CH_2ClBr^+ are seen. A closer look at the baseline reveals Cl^+ and Br^+ peaks, approximately 20% of the parent ion signal (shown in the insets).

Focusing on the fragments CH_2Cl^+ and CH_2Br^+ , resulting from carbon-halogen cleavage, one may ask whether phase shaped laser pulses can be used to optimize the relative yield of these two reaction channels, i.e. maximizing the ratio of the two fragments. Thus, adaptive femtosecond control is implemented using the signals arising from the single isotopic fragments $\text{CH}_2^{35}\text{Cl}^+$ and $\text{CH}_2^{79}\text{Br}^+$ as a feedback for the evolutionary algorithm. Optimizations were run with the goal of maximizing as well as minimizing the ratio $\text{CH}_2\text{Br}^+/\text{CH}_2\text{Cl}^+$. A threshold value was applied to the denominator to avoid unreasonably large and physically

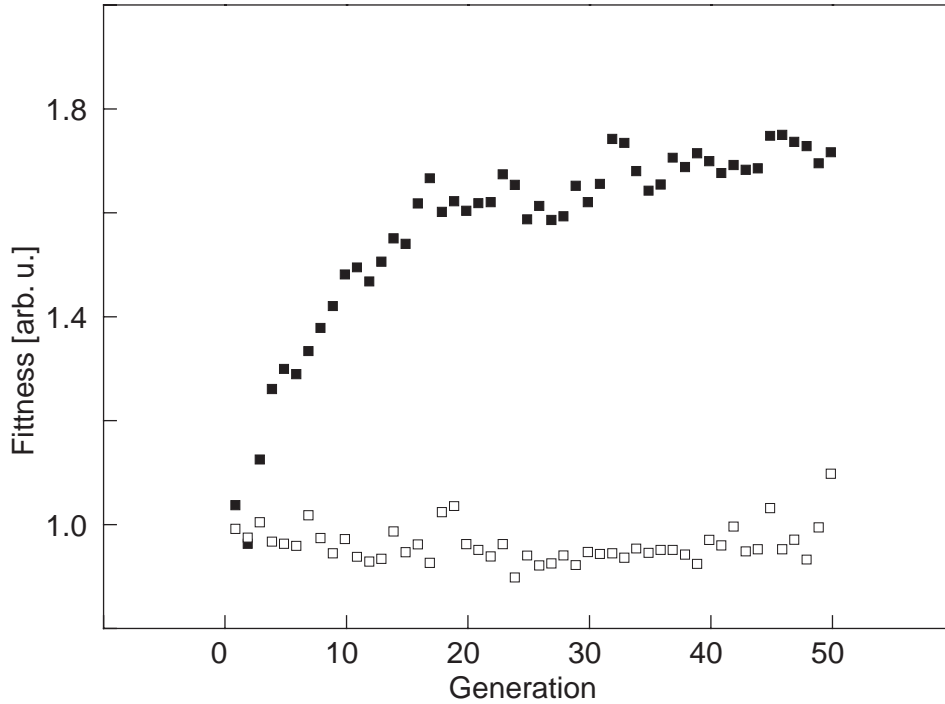


Figure A.3: Evolution curve measured for the optimization goal of maximization (filled squares) of the ion ratio $\text{CH}_2\text{Br}^+/\text{CH}_2\text{Cl}^+$. The values of the fittest individual per generation are plotted. Also shown (open squares) is the value of the ratio measured with an unmodulated (intense) laser pulse throughout the optimization process.

meaningless results if the denominator reaches values near the noise level. Although only data from one set of optimizations is shown here, the experiments were repeated on three separate occasions and similar results were obtained each time. The evolution curve for the maximization of $\text{CH}_2\text{Br}^+/\text{CH}_2\text{Cl}^+$ is shown in Figure A.3 along with the value of the ratio measured with an unmodulated laser pulse throughout the optimization procedure. For the goal of maximization, a strong increase of the ratio is seen compared to the value obtained with an unmodulated laser pulse. For the minimization case, results are less convincing mainly because the algorithm explored areas in the parameter space that have an ion yield close to the noise level. Finally, the algorithm found a less intense laser pulse and the ratio obtained from this is close to that found by energy attenuation of an unmodulated laser pulse (see below in the text). In the following, the discussion therefore concentrates on the maximization optimization.

Figure A.2b shows the mass spectrum obtained with the best laser pulse of the last generation of the maximization experiment. The value of the ion ratio $\text{CH}_2\text{Br}^+/\text{CH}_2\text{Cl}^+$ was determined by integrating over the peak areas of the $\text{CH}_2^{79}\text{Br}^+$ and $\text{CH}_2^{35}\text{Cl}^+$ fragment signals. Following maximization, a value of 1:6 ($\text{CH}_2\text{Br}^+/\text{CH}_2\text{Cl}^+$) is achieved while a bandwidth-limited reference pulse yields a ratio of 1:12. These data show the ability to manipulate the ratio

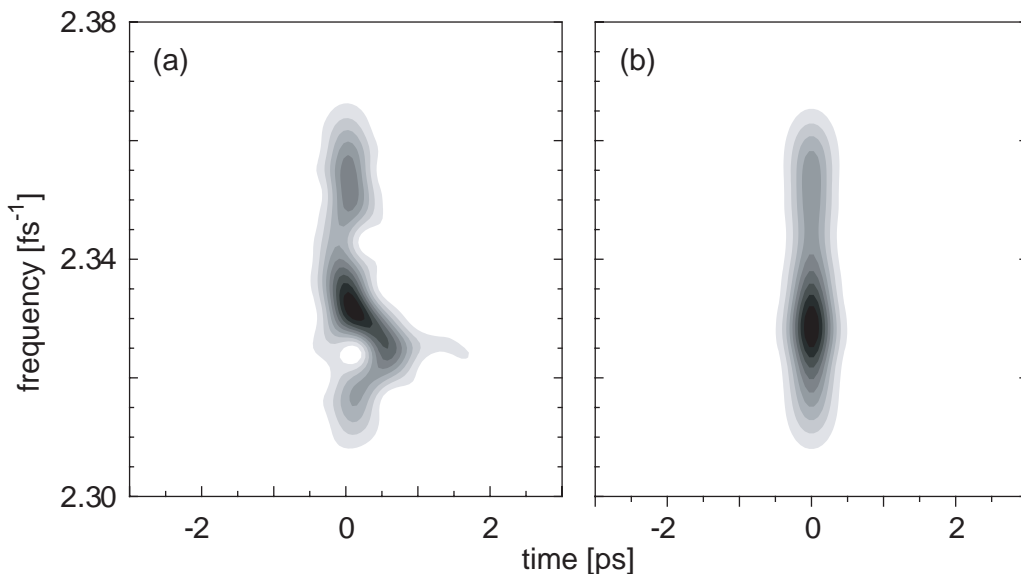


Figure A.4: Electric field shapes in Husimi representation for optimized pulses: (a) maximization of CH₂Br⁺/CH₂Cl⁺ ion ratio; (b) maximization of second harmonic generation. Black indicates regions of highest intensity and white of lowest intensity.

CH₂Br⁺/CH₂Cl⁺ by a significant amount using the optimization procedure. However, CH₂Cl⁺ which results from the cleavage of the weaker bond still remains the major feature in all spectra for all the optimization goals chosen. The best pulse of the optimization produces a much larger amount of the corresponding smaller fragments Br⁺ respectively Cl⁺ than a bandwidth limited laser pulse. But the signal arising from the cleavage of the stronger bond, Cl⁺, is larger than the one from the cleavage of the weaker bond, Br⁺.

In order to identify the control mechanism and to distinguish the adaptive phase shaping from simple pulse energy or pulse duration effects, one needs to take a closer look at the additional data taken during the optimizations. First, the electric fields found for each optimization goal are analyzed. Figure A.4 shows the electric fields for the best laser pulses found in the last generation of each optimization in the Husimi representation. For the calculations, the phase $\Phi(\omega)$ determined following maximization of SHG is used as a measure of the input phase of the pulses entering the pulse shaper. This is then subtracted from the phase measured at the pulse shaper (determined by the pixel voltages) for the result of the ratio maximization. These pulse shapes are in agreement with directly measured laser pulses using spectral interferometry. The Husimi plots clearly indicate a complex phase structure of the best laser pulse for the goal of maximizing (a) the ion ratio CH₂Br⁺/CH₂Cl⁺ in contrast to the flat phase laser pulse maximizing SHG (b).

The complex phase structure observed for the maximization of the ratio is

a good indication that the particular phase shape of the pulses — and not just simple laser intensity reduction due to an increase in the pulse duration — is responsible for the obtained selectivity. To verify this further, the unknown quantum control problem is mapped onto the well-known problem of maximizing SHG [192]. Figure A.5 shows the value of the ratio CH₂Br⁺/CH₂Cl⁺ versus the measured SHG efficiency for each laser pulse explored during both optimizations: maximization of CH₂Br⁺/CH₂Cl⁺ (Figure A.5a) and maximization of SHG (Figure A.5b). When maximization of SHG is the goal, a set of randomly phase shaped laser pulses is the starting point for the evolutionary algorithm. The signal evolves during the optimization to higher intensities resulting in the shortest possible pulse. This evolution, thus, samples a wide variation in laser pulse intensity at constant laser pulse energy. It can be seen that the ratio CH₂Br⁺/CH₂Cl⁺ changes only slightly during this intensity variation (ratio values below SHG = 0.1 are ignored since they are subject to a high degree of noise because there is no appreciable ion signal). The optimization of the CH₂Br⁺/CH₂Cl⁺ ratio shows a completely different behaviour. Although the algorithm samples mainly laser pulses within a narrow range of intensity, it obtains a wide range in product ratios. Thus, the quantum control problem of maximizing the ratio of CH₂Br⁺/CH₂Cl⁺ cannot be solved by simple intensity variation like SHG maximization.

Besides increasing the pulse duration, the laser intensity can also be varied by attenuating the pulse energy while laser pulses remain temporally short. Therefore, a series of mass spectra is collected at different laser pulse energies. The product ratio of CH₂Br⁺/CH₂Cl⁺ obtained varies from 1:12 at 230 μJ to 1:13 at lower pulse energies. However, the determination of the ratio is problematic at low pulse energies due to the low ion count rates. The same problem is encountered in the minimization optimization, which yields a similar ratio. The low product ion count rates close to the noise level do not allow to draw any further conclusions about differences between energy attenuation and the minimization case. Nevertheless, it is clear from these data that the ratio of 1:6 obtained in the maximization of CH₂Br⁺/CH₂Cl⁺ cannot be obtained with intensity variation by energy attenuation alone. These two experiments show that simple one-parameter control schemes involving only intensity variations are not sufficient to achieve control in the CH₂ClBr molecule.

In addition to the discussion above several other interesting features can be observed in the mass spectra. First, the fragmentation dynamics in the cases of SHG maximization and attenuation series do not appear to be significantly altered by the different laser pulse intensities. The mass spectrum collected following maximization of CH₂Br⁺/CH₂Cl⁺ in Figure A.2b, on the other hand, shows substantial qualitative differences. Aside from a clear increase in the ratio of interest, the optimized pulse enhances not only the formation of smaller fragments such as CH₂⁺, Cl⁺, and Br⁺, but at the same time formation of the parent ion. These features are a good indication that the laser pulse optimized for this task is in fact manipulating the fragmentation dynamics taking place. It is worth noting

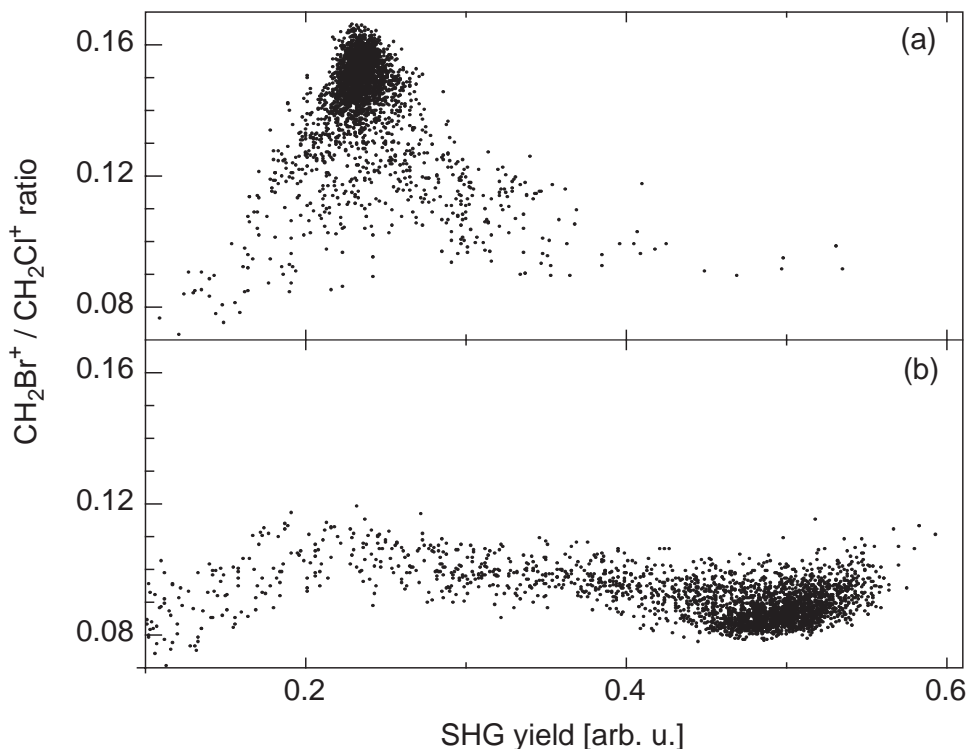


Figure A.5: Correlation diagram of $\text{CH}_2\text{Br}^+:\text{CH}_2\text{Cl}^+$ ion ratio versus measured SHG for all laser pulses explored in the two optimizations: $\text{CH}_2\text{Br}^+:\text{CH}_2\text{Cl}^+$ maximization (a), SHG maximization (b).

one additional feature observed in the spectrum of Figure A.2b. The $\text{CH}_2^{79}\text{Br}^+$ peak used in the optimization goal is significantly enhanced with respect to its isotopic counterpart $\text{CH}_2^{81}\text{Br}^+$, which was not included in the optimization goal. These data suggest that complex phase shaped laser pulses are able to manipulate dissociation dynamics in extremely subtle ways. At this point it should be noted that Averbukh *et al.* [193] achieved isotope selectivity in a pump–probe experiment in $^{79,79}\text{Br}_2/^{81,81}\text{Br}_2$ and that Leibscher *et al.* [194] developed a theoretical model for the optimal control of wave-packet isotope separation. Recently Wöste and coworkers employed adaptive femtosecond quantum control experimentally to the potassium dimer system and reported a discrimination ratio between two isotopomers of 140 [195].

The optimization results presented here have shown that phase-shaped laser pulses found by the adaptive algorithm are able to maximize the ion ratio CH_2Br^+ over CH_2Cl^+ compared with the ratio obtained using a bandwidth-limited 800 nm laser pulse. The question arises: what is the nature of the dynamics that are subjected to control in this system? Unfortunately, there is no simple answer to this question as there are multiple mechanisms by which CH_2Br^+ and CH_2Cl^+ photoproducts can be formed following multi-photon excitation of CH_2ClBr . For ex-

ample, fragments can be created on neutral potential surfaces (and subsequently ionized for detection), via ion-pair surfaces, or via dissociative ionic surfaces. In order to address possible control pathways, first the formation of photofragments is reconsidered when bandwidth-limited laser pulses are used. As could be seen in Figure A.2a, the shortest possible laser pulse (≈ 80 fs; $230 \mu\text{J}$) gave rise to the two primary photoproducts CH₂Cl⁺ and CH₂Br⁺. In Figure A.6a, two spectra are shown, which were taken using nearly bandwidth-limited pulses of the different energies ($360 \mu\text{J}/\text{pulse}$ and $80 \mu\text{J}/\text{pulse}$). It is seen that over the more than four-fold change in pulse intensity (resulting in a strong decrease of total ion signal), the spectra remain qualitatively similar without any significant intensity of the parent ion. It is emphasized that at all pulse energies explored the parent ion does not appear in the spectrum with significant relative intensity. Spectra collected using 400 nm excitation, on the other hand, show a remarkable qualitative difference. In Figure A.6b, mass spectra are presented again obtained at different laser pulse energies ($40 \mu\text{J}/\text{pulse}$ and $5 \mu\text{J}/\text{pulse}$) at 400 nm excitation wavelength. It is visible that the relative heights of the CH₂Cl⁺ and CH₂Br⁺ signals appear comparable to those collected using 800 nm excitation. However, when 400 nm excitation is used, the parent ion CH₂ClBr⁺ is a major photoproduct in the mass spectrum and this is true for all pulse intensities explored.

As already mentioned, there are multiple mechanisms by which CH₂Br⁺ and CH₂Cl⁺ photofragments can be formed following multi-photon 800 nm excitation of CH₂BrCl. Based on the observations shown in Figure 5, it is unlikely that the products form on dissociative ionic surfaces. First, if the 400 nm spectra are considered, the observation of the CH₂BrCl⁺ parent ion peak shows that at least one bound ionic state is involved. Those states lie above the ionization threshold at 10.77 eV but below the dissociative ionic states. If the fragments CH₂Br⁺ and CH₂Cl⁺ arise from dissociative ionic surfaces, a strong laser intensity dependence in the relative yield of the parent ion to the fragment ions would be observed. In the mass spectra collected, however, the relative yield of parent ion to CH₂Cl⁺ remains approximately constant as the laser intensity is increased considerably from $5 \mu\text{J}/\text{pulse}$ to $40 \mu\text{J}/\text{pulse}$. Second, if the mass spectra collected with 800 nm excitation are taken into consideration, there is no significant contribution from the parent ion signal during the more than four-fold pulse intensity reduction. Since photoproduct formation via dissociative ionic surfaces of CH₂BrCl requires that more than eleven 800 nm photons ($> 17 \text{ eV}$) be absorbed in about 100 fs it is unreasonable to expect that the relative ion yields would not change during this intensity reduction. This is especially true in light of the observation that the parent ion is so prominent in the 400 nm spectra at all intensities explored.

Following the above discussion, dissociative ionization can be ruled out as a major origin of CH₂Br⁺ and CH₂Cl⁺ ion formation. Therefore, the dynamics on neutral surfaces are mainly responsible for the molecular fragmentation. Of the possible mechanisms available to the CH₂ClBr system, the most promising candidate is the one in which an electron from a non-bonding lone pair of a

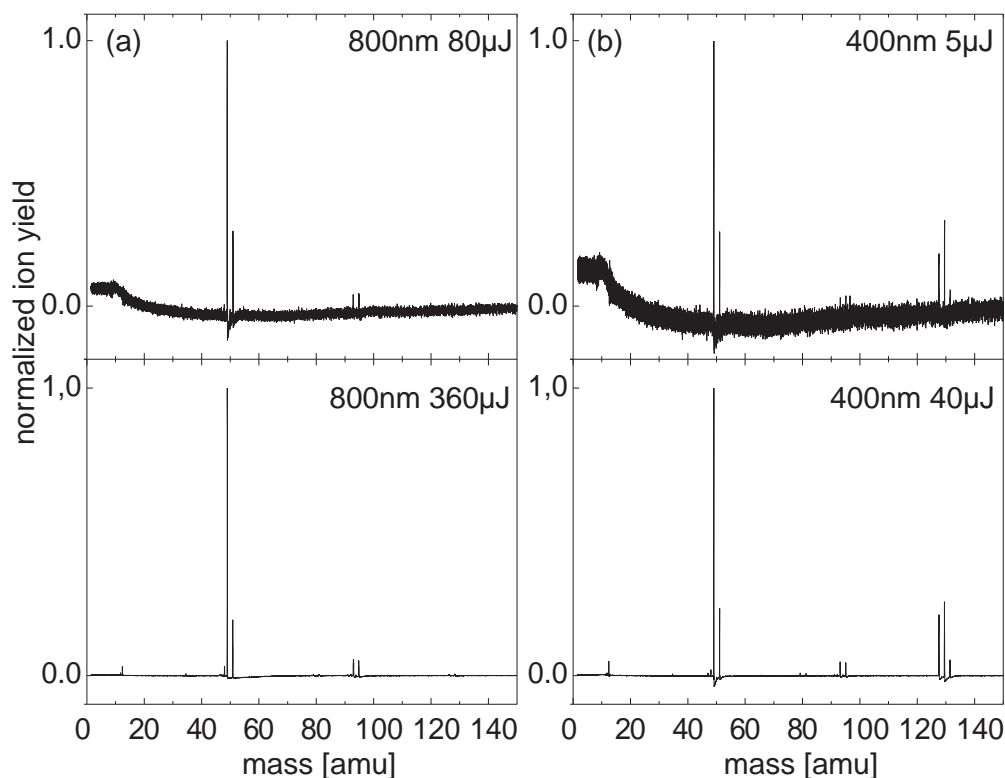


Figure A.6: Mass spectra obtained with 800 nm (a) and 400 nm (b) excitation. The laser pulse energy was 80 $\mu\text{J}/\text{pulse}$ and 360 $\mu\text{J}/\text{pulse}$ for the 800 nm excitation (a) 5 $\mu\text{J}/\text{pulse}$ and 40 $\mu\text{J}/\text{pulse}$ for the 400 nm excitation (b).

halogen atom is initially excited to Rydberg states by the bandwidth-limited 800 nm laser pulse [196]. Such states can then be pre-dissociated by ion-pair states wherein a bonding electron is transferred from the alkyl-halide to the halogen atom that has undergone the Rydberg transition. This has been observed for related molecules such as CH₃Cl and CH₃Br [197, 198]. It is emphasized that within this mechanism, one of the carbon-halogen bonds in CH₂ClBr is broken in a way which leads directly to the formation of an alkyl-halide cation (CH₂Cl⁺ or CH₂Br⁺) and the corresponding halogen anion (Br⁻ or Cl⁻, respectively). Because only cations are detected in the TOF spectrometer, the CH₂Cl⁺ and CH₂Br⁺ fragments would dominate the mass spectrum. This is entirely consistent with the spectroscopic results using 800 nm excitation. It explains especially the low relative yield of Cl⁺ and Br⁺ fragments when bandwidth-limited laser pulses are used. The increase of the Cl⁺ respectively Br⁺ signal following optimization indicates that the control mechanism is less favorably using the ion-pair surfaces.

According to the arguments presented above, a bandwidth-limited 800 nm laser pulse produces CH₂Br⁺ and CH₂Cl⁺ fragments preferentially via dynamics involving Rydberg states that are then predissociated by ion-pair states. This is an interesting situation because the phase-shaped pulses optimized for maximiz-

ing the $\text{CH}_2\text{Br}^+/\text{CH}_2\text{Cl}^+$ ratio have a complex temporal shape and are therefore significantly less intense. This implies that the surfaces on which control is taking place are likely to be lower in energy. As a result of this, it is entirely reasonable to assume that control takes place because the shaped laser field is able to manipulate wave packet motion on the neutral $\sigma^*(\text{C-X})(\text{X}=\text{Cl}, \text{Br})$ repulsive surfaces discussed in the introduction. It should be noted here that transitions to the $\sigma^*(\text{C-Br})$ and $\sigma^*(\text{C-Cl})$ surfaces take place at 6.04 eV and 7.55 eV respectively, which can be easily accessed by absorption of four 800 nm photons (6.20 eV) or five 800 nm photons (7.75 eV). As spectroscopic evidence in support of a control mechanism using such surfaces, the first indication is the enhancement of the smaller mass fragments Br^+ and Cl^+ following the $\text{CH}_2\text{Br}^+/\text{CH}_2\text{Cl}^+$ maximization pulse (Figure A.2b). This is consistent with a mechanism wherein the neutral fragments formed on the repulsive surfaces are subsequently ionized by the temporally elongated phase-shaped pulse. In addition, a larger relative size of the Cl^+ signal is observed with respect to the Br^+ signal. This suggests that the shaped excitation pulse uses the dissociative neutral surfaces, but does so in a way that enhances the breakage of the stronger C-Cl bond over breakage of the weaker C-Br bond leading to the maximization result. The continued prominence of CH_2Cl^+ over CH_2Br^+ (despite the reversed intensity of Br^+ and Cl^+ signals) would simply suggest that even with this optimized pulse, a substantial amount of the fragment ions continue to be formed via ion-pair states.

A.3 Conclusion

The results presented above show that femtosecond adaptive pulse shaping is a powerful tool for manipulating photoproduct distributions. It has been shown that shaped laser pulses can be found which both minimize and maximize the ion ratio $\text{CH}_2\text{Br}^+/\text{CH}_2\text{Cl}^+$ with respect to the one achieved with a bandwidth-limited laser pulse. This is done automatically and without prior knowledge of the molecular potential energy surfaces involved. Concentrating on the maximization case, a complex optimal laser pulse is discovered which more than doubles the ion ratio. This corresponds to a significant relative change in the breaking of the stronger carbon-halogen bond. Intensity dependence measurements show that this effect is not simply a result of intensity changes in the laser pulse. It appears rather that the shaped laser pulse changes the fragmentation dynamics and the control mechanism may involve manipulation of wave packet motion on neutral dissociative surfaces, which are not involved in photoproduct formation when bandwidth-limited 800 nm pulses are used. These results are an encouraging indication that even in systems such as CH_2ClBr (where excited states are highly coupled), complex laser fields may be useful for achieving bond-selective photochemistry.

Bibliography

- [1] E. A. Abbott.
Flatland.
Seeley, London (1884).
- [2] R. S. Judson and H. Rabitz.
Teaching lasers to control molecules.
Phys. Rev. Lett. **68**, 1500–1503 (1992).
- [3] R. V. Ambartsumian and V. S. Letokhov.
In C. B. Moore (Ed.), *Chemical and biochemical applications of lasers*, volume 3.
Academic Press, New York (1977).
- [4] J. Jortner, R. D. Levine, and S. A. Rice (Eds.).
Photoselective Chemistry, volume 47 of *Advances in Chemical Physics*.
Wiley, New York (1981).
- [5] N. Bloembergen and A. H. Zewail.
Energy redistribution in isolated molecules and the question of mode-selective laser chemistry revisited.
J. Phys. Chem. **88**, 5459–5465 (1984).
- [6] T. Elsaesser and W. Kaiser.
Vibrational and vibronic relaxation of large polyatomic molecules in liquids.
Annu. Rev. Phys. Chem. **42**, 83–107 (1991).
- [7] M. Gruebele and R. Bigwood.
Molecular vibrational energy flow: Beyond the golden rule.
Int. Rev. Phys. Chem. **17**, 91–145 (1998).
- [8] M. Shapiro and P. Brumer.
Principles of the quantum control of molecular processes.
Wiley-Interscience, Hoboken, NJ (2003).
- [9] M. Shapiro and P. Brumer.
Coherent control of molecular dynamics.
Rep. Prog. Phys. **66**, 859–942 (2003).
- [10] P. Brumer and M. Shapiro.
Control of unimolecular reactions using coherent light.
Chem. Phys. Lett. **126**, 541–546 (1986).

- [11] M. Shapiro, J. W. Hepburn, and P. Brumer.
Simplified laser control of unimolecular reactions: Simultaneous (ω_1, ω_3) excitation.
Chem. Phys. Lett. **149**, 451–454 (1988).
- [12] C. Chen, Y. Yin, and D. S. Elliott.
Interference between optical transitions.
Phys. Rev. Lett. **64**, 507–510 (1990).
- [13] S. M. Park, S. P. Lu, and R. J. Gordon.
Coherent laser control of the resonance-enhanced multiphoton ionization of HCl.
J. Chem. Phys. **94**, 8622–8624 (1991).
- [14] L. C. Zhu, V. D. Kleiman, X. N. Li, S. P. Lu, K. Trentelman, and R. J. Gordon.
Coherent laser control of the product distribution obtained in the photoexcitation of HI.
Science **270**, 77–80 (1995).
- [15] D. J. Tannor and S. A. Rice.
Control of selectivity of chemical reaction via control of wavepacket evolution.
J. Chem. Phys. **83**, 5013–5018 (1985).
- [16] D. J. Tannor, R. Kosloff, and S. A. Rice.
Coherent pulse sequence induced control of selectivity of reactions: Exact quantum mechanical calculations.
J. Chem. Phys. **85**, 5805–8520 (1986).
- [17] T. Baumert, M. Grosser, R. Thalweiser, and G. Gerber.
Femtosecond time-resolved molecular multiphoton ionization: The Na_2 system.
Phys. Rev. Lett. **67**, 3753–3756 (1991).
- [18] E. D. Potter, J. L. Herek, S. Pedersen, O. Liu, and A. H. Zewail.
Femtosecond laser control of a chemical reaction.
Nature **355**, 66–68 (1992).
- [19] T. Baumert and G. Gerber.
Fundamental interactions of molecules (Na_2, Na_3) with intense femtosecond laser pulses.
Isr. J. Chem. **34**, 103–114 (1994).
- [20] U. Gaubatz, P. Rudecki, M. Becker, S. Schiemann, M. Kulz, and K. Bergmann.
Population switching between vibrational levels in molecular beams.
Chem. Phys. Lett. **149**, 463–468 (1988).
- [21] U. Gaubatz, P. Rudecki, S. Schiemann, and K. Bergmann.
Population transfer between molecular vibrational levels by stimulated Raman scattering with partially overlapping laser fields: A new concept and experimental results.
J. Chem. Phys. **92**, 5363–5376 (1990).

-
- [22] K. Bergmann, H. Theuer, and B. W. Shore.
Coherent population transfer among quantum states of atoms and molecules.
Rev. Mod. Phys. **70**, 1003–1025 (1998).
- [23] M. Shapiro and P. Brumer.
On the origin of pulse shaping control of molecular dynamics.
J. Phys. Chem. A **105**, 2897–2902 (2001).
- [24] D. Meshulach and Y. Silberberg.
Coherent quantum control of two-photon transitions by a femtosecond laser pulse.
Nature **396**, 239–242 (1998).
- [25] A. Shi, A. Woody, and H. Rabitz.
Optimal control of selective vibrational excitation in harmonic linear chain molecules.
J. Chem. Phys. **88**, 6870–6883 (1988).
- [26] A. P. Peirce, M. Dahleh, and H. Rabitz.
Optimal control of quantum-mechanical systems: Existence, numerical approximation, and applications.
Phys. Rev. A **37**, 4950–4964 (1988).
- [27] R. Kosloff, S. A. Rice, P. Gaspard, S. Tersigni, and D. J. Tannor.
Wavepacket dancing: Achieving chemical selectivity by shaping light pulses.
Chem. Phys. **139**, 201–220 (1989).
- [28] W. Jakubetz and B. L. Lan.
Resonance-leaking to specific background states: A loss mechanism in molecular multiphoton transitions.
J. Chem. Phys. **117**, 7968–7979 (2002).
- [29] S. Kirkpatrick, C. D. Gelatt, and M. P. Vecchi.
Optimization by simulated annealing.
Science **220**, 671–680 (1983).
- [30] D. E. Goldberg.
Genetic Algorithms in Search, Optimization, and Machine Learning.
Addison-Wesley, Reading (1993).
- [31] H.-P. Schwefel.
Evolution and Optimum Seeking.
Wiley, New York (1995).
- [32] V. Seyfried.
Beobachtung und Kontrolle molekularer Dynamik durch Femtosekundenlaserpulse.
Dissertation, Universität Würzburg (1998).

- [33] T. Brixner.
Adaptive Femtosecond Quantum Control.
Dissertation, Universität Würzburg (2001).
- [34] O. Rubner, T. Baumert, M. Bergt, B. Kiefer, G. Gerber, and V. Engel.
Theoretical analysis of femtosecond excitation and fragmentation dynamics of $Fe(CO)_5$.
Chem. Phys. Lett. **316**, 585–592 (2000).
- [35] C. Daniel, J. Full, L. González, C. Lupulescu, J. Manz, A. Merli, S. Vajda, and L. Wöste.
Deciphering the reaction dynamics underlying optimal control laser fields.
Science **299**, 536–539 (2003).
- [36] C. J. Bardeen, V. V. Yakovlev, K. R. Wilson, S. D. Carpenter, P. M. Weber, and W. S. Warren.
Feedback quantum control of molecular electronic population transfer.
Chem. Phys. Lett. **280**, 151–158 (1997).
- [37] J. L. Herek, W. Wohlleben, R. J. Cogdell, D. Zeidler, and M. Motzkus.
Quantum control of energy flow in light harvesting.
Nature **417**, 533–535 (2002).
- [38] G. Vogt, G. Krampert, P. Niklaus, and G. Gerber.
Optimal Control of Photoisomerisation.
Nature p. submitted (2004).
- [39] N. Dudovich, D. Oron, and Y. Silberberg.
Single-pulse coherently controlled nonlinear Raman spectroscopy and microscopy.
Nature **418**, 512–514 (2002).
- [40] T. Brixner, N. H. Damrauer, P. Niklaus, and G. Gerber.
Photoselective adaptive femtosecond quantum control in the liquid phase.
Nature **414**, 57–60 (2001).
- [41] J. L. Bada.
Biomolecules - Origins of Homochirality.
Nature **374**, 594–595 (1995).
- [42] J. Bailey, A. Chrysostomou, J. H. Hough, T. M. Gledhill, A. McCall, S. Clark, F. Menard, and M. Tamura.
Circular polarization in star-formation regions: Implications for biomolecular homochirality.
Science **281**, 672–674 (1998).
- [43] H. Rau.
Asymmetric Photochemistry in Solution.
Chem. Rev. **83**, 535–547 (1983).

-
- [44] Y. Inoue.
Asymmetric Photochemical-Reactions in Solution.
Chem. Rev. **92**, 741–770 (1992).
- [45] G. L. J. A. Rikken and E. Raupach.
Enantioselective magnetochiral photochemistry.
Nature **405**, 932–935 (2000).
- [46] M. Shapiro, E. Frishman, and P. Brumer.
Coherently controlled asymmetric synthesis with achiral light.
Phys. Rev. Lett. **84**, 1669–1672 (2000).
- [47] D. Gerbasi, M. Shapiro, and P. Brumer.
Theory of enantiomeric control in dimethylallene using achiral light.
J. Chem. Phys. **115**, 5349–5352 (2001).
- [48] E. Frishman, M. Shapiro, D. Gerbasi, and P. Brumer.
Enantiomeric purification of nonpolarized racemic mixtures using coherent light.
J. Chem. Phys. **119**, 7237–7246 (2003).
- [49] L. González, K. Hoki, D. Kroner, A. S. Leal, J. Manz, and Y. Ohtsuki.
Selective preparation of enantiomers by laser pulses: From optimal control to specific pump and dump transitions.
J. Chem. Phys. **113**, 11134–11142 (2000).
- [50] Y. Fujimura, L. González, K. Hoki, D. Kroner, J. Manz, and Y. Ohtsuki.
From a racemate to a pure enantiomer by laser pulses: Quantum model simulations for H₂POSH.
Angewandte Chemie-International Edition **39**, 4586–+ (2000).
- [51] K. Hoki, L. González, and Y. Fujimura.
Quantum control of molecular handedness in a randomly oriented racemic mixture using three polarization components of electric fields.
J. Chem. Phys. **116**, 8799–8802 (2002).
- [52] D. Gerbasi, P. Brumer, I. Thanopoulos, P. Kral, and M. Shapiro.
Theory of the two step enantiomeric purification of 1,3 dimethylallene.
J. Chem. Phys. **120**, 11557–11563 (2004).
- [53] A. Baltuška, T. Fuji, and T. Kobayashi.
Controlling the carrier–envelope phase of ultrashort light pulses with optical parametric amplifiers.
Phys. Rev. Lett. **88**, art–133901 (2002).
- [54] A. Baltuška, T. Udem, M. Uiberacker, M. Hentschel, E. Goulielmakis, C. Gohle, R. Holzwarth, V. S. Yakovlev, A. Scrinzi, T. W. Hansch, and F. Krausz.
Attosecond control of electronic processes by intense light fields.
Nature **421**, 611–615 (2003).

- [55] A. Ulman.
Formation and structure of self-assembled monolayers.
Chem. Rev. **96**, 1533–1554 (1996).
- [56] M. A. Belkin, T. A. Kulakov, K. H. Ernst, L. Yan, and Y. R. Shen.
Sum-frequency vibrational spectroscopy on chiral liquids: A novel technique to probe molecular chirality.
Phys. Rev. Lett. **85**, 4474–4477 (2000).
- [57] M. A. Belkin and Y. R. Shen.
Doubly resonant IR-UV sum-frequency vibrational spectroscopy on molecular chirality.
Phys. Rev. Lett. **91**, art-213907 (2003).
- [58] H. Stapelfeldt and T. Seideman.
Colloquium: Aligning molecules with strong laser pulses.
Rev. Mod. Phys. **75**, 543–557 (2003).
- [59] J. J. Larsen, K. Hald, N. Bjerre, and H. Stapelfeldt.
Three dimensional alignment of molecules using elliptically polarized laser fields.
Phys. Rev. Lett. **85**, 2470–2473 (2000).
- [60] M. D. Poulsen, E. Peronne, H. Stapelfeldt, C. Z. Bisgaard, S. S. Viftrup, E. Hamilton, and T. Seideman.
Nonadiabatic alignment of asymmetric top molecules: Rotational revivals.
J. Chem. Phys. **121**, 783–791 (2004).
- [61] A. Flettner, J. König, M. B. Mason, T. Pfeifer, U. Weichmann, and G. Gerber.
Atomic and molecular high-harmonic generation: a comparison of ellipticity dependence based on the three-step model.
Journal of Modern Optics **50**, 529–537 (2003).
- [62] M. Protopapas, C. H. Keitel, and P. L. Knight.
Atomic physics with super-high intensity lasers.
Rep. Prog. Phys. **60**, 389–486 (1997).
- [63] T. Brabec and F. Krausz.
Intense few-cycle laser fields: Frontiers of nonlinear optics.
Rev. Mod. Phys. **72**, 545–591 (2000).
- [64] P. B. Corkum, N. H. Burnett, and M. Y. Ivanov.
Subfemtosecond pulses.
Opt. Lett. **19**, 1870–1872 (1994).
- [65] M. Y. Ivanov, P. B. Corkum, T. Zuo, and A. D. Bandrauk.
Routes to control of intense-field atomic polarizability.
Phys. Rev. Lett. **74**, 2933–2936 (1995).

-
- [66] E. Constant, V. D. Taranukhin, A. Stolow, and P. B. Corkum.
Methods for the measurement of the duration of high-harmonic pulses.
Phys. Rev. A **56**, 3870–3878 (1997).
- [67] B. H. Bransden and C. J. Joachain.
Physics of Atoms and Molecules.
Longman Scientific & Technical, Harlow (1983).
- [68] H. Kuhn and H. D. Försterling.
Principles of Physical Chemistry.
John Wiley & Sons Ltd, New York (2000).
- [69] G. Herzberg.
Molecular Spectra and Molecular Structure I. Spectra of Diatomic Molecules.
Litton Educational Publishing, INC., New York (1950).
- [70] A. L. Schawlow and C. H. Townes.
Infrared and Optical Masers.
Phys. Rev. **112**, 1940–1949 (1958).
- [71] A. J. Demaria, D. A. Stetser, and H. Heynau.
Self Mode-Locking of Lasers with Saturable Absorbers - (Regenerative Pulse Oscillator Bleachable Dyes E).
Appl. Phys. Lett. **8**, 174 (1966).
- [72] R. L. Fork, B. I. Greene, and C. V. Shank.
Generation of Optical Pulses Shorter Than 0.1 Psec by Colliding Pulse Mode-Locking.
Appl. Phys. Lett. **38**, 671–672 (1981).
- [73] J. M. Hopkins and W. Sibbett.
Ultrashort-pulse lasers: Big payoffs in a flash.
Scientific American **283**, 72–79 (2000).
- [74] U. Keller.
Recent developments in compact ultrafast lasers.
Nature **424**, 831–838 (2003).
- [75] P. F. Moulton.
Spectroscopic and Laser Characteristics of $Ti:Al_2O_3$.
J. Opt. Soc. Am. B **3**, 125–133 (1986).
- [76] D. E. Spence, P. N. Kean, and W. Sibbett.
60 fs pulse generation from a self-mode-locked ti-sapphire laser.
Opt. Lett. **16**, 42–44 (1991).
- [77] R. Szipócs, K. Ferencz, C. Spielmann, and F. Krausz.
Chirped Multilayer Coatings for Broad-Band Dispersion Control in Femtosecond Lasers.
Opt. Lett. **19**, 201–203 (1994).

- [78] D. Strickland and G. Mourou.
Compression of Amplified Chirped Optical Pulses.
Opt. Commun. **56**, 219–221 (1985).
- [79] C. LeBlanc, P. Curley, and F. Salin.
Gain-narrowing and gain-shifting of ultra-short pulses in Ti:sapphire amplifiers.
Opt. Commun. **131**, 391–398 (1996).
- [80] J.-C. Diels and W. Rudolph.
Ultrashort Laser Pulse Phenomena.
Academic Press, London (1996).
- [81] A. M. Weiner, D. E. Leaird, J. S. Patel, and J. R. Wullert II.
Programmable femtosecond pulse shaping by use of a multielement liquid-crystal phase modulator.
Opt. Lett. **15**, 326–328 (1990).
- [82] A. M. Weiner, D. E. Leaird, A. Patel, and J. R. Wullert II.
Programmable shaping of femtosecond optical pulses by use of 128-element liquid-crystal phase modulator.
IEEE J. Quantum Electron. **28**, 908–920 (1992).
- [83] M. M. Wefers and K. A. Nelson.
Generation of high-fidelity programmable ultrafast optical wave-forms.
Opt. Lett. **20**, 1047–1049 (1995).
- [84] M. M. Wefers and K. A. Nelson.
Analysis of programmable ultrashort waveform generation using liquid-crystal spatial light modulators.
J. Opt. Soc. Am. B **12**, 1343–1362 (1995).
- [85] A. M. Weiner.
Femtosecond pulse shaping using spatial light modulators.
Rev. Sci. Instrum. **71**, 1929–1960 (2000).
- [86] T. Brixner.
Kohärente Kontrolle von Photodissoziationsreaktionen mit optimal geformten ultrakurzen Laserpulsen.
Diplomarbeit, Universität Würzburg (1998).
- [87] T. Baumert, T. Brixner, V. Seyfried, M. Strehle, and G. Gerber.
Femtosecond pulse shaping by an evolutionary algorithm with feedback.
Appl. Phys. B **65**, 779–782 (1997).
- [88] T. Brixner, M. Strehle, and G. Gerber.
Feedback-controlled optimization of amplified femtosecond laser pulses.
Appl. Phys. B **68**, 281–284 (1999).

-
- [89] O. E. Martínez.
Matrix formalism for pulse compressors.
IEEE J. Quantum Electron. **24**, 2530–2536 (1988).
- [90] G. Stobrawa, M. Hacker, T. Feurer, D. Zeidler, M. Motzkus, and F. Reichel.
A new high-resolution femtosecond pulse shaper.
Appl. Phys. B **72**, 627–630 (2001).
- [91] J. Paye and A. Migus.
Space-time Wigner functions and their application to the analysis of a pulse shaper.
J. Opt. Soc. Am. B **12**, 1480–1490 (1995).
- [92] M. M. Wefers and K. A. Nelson.
Space-time profiles of shaped ultrafast optical waveforms.
IEEE J. Quantum Electron. **32**, 161–172 (1996).
- [93] H. Kuck, W. Doleschal, A. Gehner, W. Grundke, R. Melcher, J. Paufler, R. Seltmann, and G. Zimmer.
Deformable micromirror devices as phase-modulating high-resolution light valves.
Sensors and Actuators A-Physical **54**, 536–541 (1996).
- [94] M. Hacker, G. Stobrawa, R. Sauerbrey, T. Buckup, M. Motzkus, M. Wildenhain, and A. Gehner.
Micromirror SLM for femtosecond pulse shaping in the ultraviolet.
Appl. Phys. B **76**, 711–714 (2003).
- [95] G. Vdovin and P. M. Sarro.
Flexible Mirror Micromachined in Silicon.
Appl. Opt. **34**, 2968–2972 (1995).
- [96] A. Suda, Y. Oishi, K. Nagasaka, P. Q. Wang, and K. Midorikawa.
A spatial light modulator based on fused-silica plates for adaptive feedback control of intense femtosecond laser pulses.
Opt. Express **9**, 2–6 (2001).
- [97] E. Sidick, A. Knoesen, and A. Dienes.
Ultrashort-Pulse Second-Harmonic Generation. 1. Transform-Limited Fundamental Pulses.
J. Opt. Soc. Am. B **12**, 1704–1712 (1995).
- [98] E. Sidick, A. Dienes, and A. Knoesen.
Ultrashort-Pulse Second-Harmonic Generation. 2. Non-Transform-Limited Fundamental Pulses.
J. Opt. Soc. Am. B **12**, 1713–1722 (1995).
- [99] M. Hacker, R. Netz, M. Roth, G. Stobrawa, T. Feurer, and R. Sauerbrey.
Frequency doubling of phase-modulated, ultrashort laser pulses.
Appl. Phys. B **73**, 273–277 (2001).

- [100] R. Trebino.
Frequency-Resolved Optical Gating: The Measurement of Ultrashort Laser Pulses.
Kluwer Academic Publishers, Norwell (2000).
- [101] B. Schmidt, M. Hacker, G. Stobrawa, and T. Feurer.
LAB2-A virtual femtosecond laser lab.
<http://www.lab2.de> (2001).
- [102] K. Naganuma, K. Mogi, and H. Yamada.
General method for ultrashort light pulse chirp measurement.
IEEE J. Quantum Electron. **25**, 1225–1233 (1989).
- [103] A. Baltuška, Z. Wei, M. S. Pshenichnikov, D. A. Wiersma, and R. Szipőcs.
All-solid-state cavity-dumped sub-5-fs laser.
Appl. Phys. B **65**, 175–188 (1997).
- [104] J. Peatross and A. Rundquist.
Temporal decorrelation of short laser pulses.
J. Opt. Soc. Am. B **15**, 216–222 (1998).
- [105] D. J. Kane and R. Trebino.
Single-shot measurement of the intensity and phase of an arbitrary ultrashort pulse by using frequency-resolved optical gating.
Opt. Lett. **18**, 823–825 (1993).
- [106] R. Trebino and D. J. Kane.
Using phase retrieval to measure the intensity and phase of ultrashort pulses: Frequency-resolved optical gating.
J. Opt. Soc. Am. A **10**, 1101–1111 (1993).
- [107] R. Trebino, K. W. DeLong, D. N. Fittinghoff, J. N. Sweetser, M. A. Krumbügel, B. A. Richman, and D. J. Kane.
Measuring ultrashort laser pulses in the time-frequency domain using frequency-resolved optical gating.
Rev. Sci. Instrum. **68**, 3277–3295 (1997).
- [108] S. Linden, H. Giessen, and J. Kuhl.
XFROG - A new method for amplitude and phase characterization of weak ultrashort pulses.
Phys. Stat. Sol. (B) **206**, 119–124 (1998).
- [109] S. Linden, J. Kuhl, and H. Giessen.
Amplitude and phase characterization of weak blue ultrashort pulses by downconversion.
Opt. Lett. **24**, 569–571 (1999).

-
- [110] J. Y. Zhang, A. P. Shreenath, M. Kimmel, E. Zeek, R. Trebino, and S. Link.
Measurement of the intensity and phase of attojoule femtosecond light pulses using optical-parametric-amplification cross-correlation frequency-resolved optical gating.
Opt. Express **11**, 601–609 (2003).
- [111] K. W. DeLong, D. N. Fittinghoff, R. Trebino, B. Kohler, and K. R. Wilson.
Pulse retrieval in frequency-resolved optical gating based method of generalized projections.
Opt. Lett. **19**, 2152–2154 (1994).
- [112] K. W. DeLong and R. Trebino.
Improved ultrashort pulse-retrieval algorithm for frequency-resolved optical gating.
J. Opt. Soc. Am. A **11**, 2429–2437 (1994).
- [113] C. Froehly, A. Lacourt, and J. C. Vienot.
Notions de réponse impulsionnelle et de fonction de transfert temporelles des pupilles optiques, justifications expérimentales et applications.
J. Opt. (Paris) **4**, 183 (1973).
- [114] J. Piasecki, B. Colombeau, M. Vampouille, C. Froehly, and J. A. Arnaud.
Nouvelle méthode de mesure de la réponse impulsionnelle des fibres optiques.
Appl. Opt. **19**, 3749 (1980).
- [115] L. Lepetit, G. Chériaux, and M. Joffre.
Linear techniques of phase measurement by femtosecond spectral interferometry for applications in spectroscopy.
J. Opt. Soc. Am. B **12**, 2467–2474 (1995).
- [116] D. N. Fittinghoff, J. L. Bowie, J. N. Sweetsers, R. T. Jennings, M. A. Krumbugel, K. W. DeLong, R. Trebino, and I. A. Walmsley.
Measurement of the intensity and phase of ultraweak, ultrashort laser pulses.
Opt. Lett. **21**, 884–886 (1996).
- [117] W. J. Walecki, D. N. Fittinghoff, A. L. Smirl, and R. Trebino.
Characterization of the polarization state of weak ultrashort coherent signals by dual-channel spectral interferometry.
Opt. Lett. **22**, 81–83 (1997).
- [118] C. Dorrer.
Influence of the calibration of the detector on spectral interferometry.
J. Opt. Soc. Am. B **16**, 1160–1168 (1999).
- [119] L. Cohen.
Time Frequency-Distributions - A Review.
Proc. IEEE **77**, 941–981 (1989).

- [120] E. Wigner.
On the quantum correction for thermodynamic equilibrium.
Phys. Rev. **40**, 749–759 (1932).
- [121] W. P. Schleich.
Quantum Optics in Phase Space.
Wiley–VCH, Weinheim (2001).
- [122] J. Paye.
The chronocyclic representation of ultrashort light pulses.
IEEE J. Quantum Electron. **28**, 2262–2273 (1992).
- [123] C. Altucci, C. Delfin, L. Roos, M. B. Gaarde, A. L’Huillier, I. Mercer, T. Starczewski, and C.-G. Wahlström.
Frequency-resolved time-gated high-order harmonics.
Phys. Rev. A **58**, 3934–3941 (1998).
- [124] M. Kakehata, R. Ueda, H. Takada, K. Torizuka, and M. Obara.
Combination of high-intensity femtosecond laser pulses for generation of time-dependent polarization pulses and ionization of atomic gas.
Appl. Phys. B **70**, S207–S213 (2000).
- [125] D. N. Villeneuve, S. A. Aseyev, P. Dietrich, M. Spanner, M. Y. Ivanov, and P. B. Corkum.
Forced molecular rotation in an optical centrifuge.
Phys. Rev. Lett. **85**, 542–545 (2000).
- [126] Z. Z. Zhuang, S. W. Suh, and J. S. Patel.
Polarization controller using nematic liquid crystals.
Opt. Lett. **24**, 694–696 (1999).
- [127] R. L. Eriksen, P. C. Mogensen, and J. Glückstad.
Elliptical polarisation encoding in two dimensions using phase-only spatial light modulators.
Opt. Commun. **187**, 325–336 (2001).
- [128] T. Brixner and G. Gerber.
Femtosecond polarization pulse shaping.
Opt. Lett. **26**, 557–559 (2001).
- [129] T. Brixner, G. Krampert, P. Niklaus, and G. Gerber.
Generation and characterization of polarization-shaped femtosecond laser pulses.
Appl. Phys. B **74**, S133–S144 (2002).
- [130] O. Buccafusca, X. Chen, W. J. Walecki, and A. L. Smirl.
Measurement of the ultrafast polarization dynamics of weak four-wave mixing signals by dual-channel femtosecond spectral interferometry.
J. Opt. Soc. Am. B **15**, 1218–1223 (1998).

-
- [131] C. Dorrer, N. Belabas, J.-P. Likforman, and M. Joffre.
Spectral resolution and sampling issues in Fourier-transform spectral interferometry.
J. Opt. Soc. Am. B **17**, 1795–1802 (2000).
- [132] C. Dorrer, N. Belabas, J.-P. Likforman, and M. Joffre.
Experimental implementation of Fourier-transform spectral interferometry and its application to the study of spectrometers.
Appl. Phys. B **70**, S99–S107 (2000).
- [133] M. V. Klein and T. E. Furtak.
Optics.
Second edition. Wiley, New York (1986).
- [134] *Polarization and Polarization Control*, pp. 1–8.
New Focus (2003).
- [135] A. Gerrard and J. M. Burch.
Introduction to Matrix Methods in Optics.
Wiley, New York (1975).
- [136] D. Yelin, D. Meshulach, and Y. Silberberg.
Adaptive femtosecond pulse compression.
Opt. Lett. **22**, 1793–1795 (1997).
- [137] A. Efimov, M. D. Moores, N. M. Beach, J. L. Krause, and D. H. Reitze.
Adaptive control of pulse phase in a chirped-pulse amplifier.
Opt. Lett. **23**, 1915–1917 (1998).
- [138] A. Assion, T. Baumert, M. Bergt, T. Brixner, B. Kiefer, V. Seyfried, M. Strehle, and G. Gerber.
Control of chemical reactions by feedback-optimized phase-shaped femtosecond laser pulses.
Science **282**, 919–922 (1998).
- [139] M. Shapiro and P. Brumer.
Controlled photon induced symmetry breaking: Chiral molecular products from achiral precursors.
J. Chem. Phys. **95**, 8658–8661 (1991).
- [140] Y. Fujimura, L. González, K. Hoki, J. Manz, and Y. Ohtsuki.
Selective preparation of enantiomers by laser pulses: Quantum model simulation for H₂POSH.
Chem. Phys. Lett. **306**, 1–8 (1999).
- [141] T. Brixner and G. Gerber.
Quantum control of gas-phase and liquid-phase femtochemistry.
ChemPhysChem **4**, 418–438 (2003).

- [142] M. M. Wefers, H. Kawashima, and K. A. Nelson.
Optical control over two-dimensional lattice vibrational trajectories in crystalline quartz.
J. Chem. Phys. **108**, 10248–10255 (1998).
- [143] D. Oron, N. Dudovich, and Y. Silberberg.
Femtosecond phase-and-polarization control for background-free coherent anti-Stokes Raman spectroscopy.
Phys. Rev. Lett. **90**, art-213902 (2003).
- [144] R. deVivieRiedle, B. Reischl, S. Rutz, and E. Schreiber.
Femtosecond Study of Multiphoton Ionization Processes in K_2 at Moderate Laser Intensities.
J. Phys. Chem. **99**, 16829–16834 (1995).
- [145] R. deVivieRiedle, K. Kobe, J. Manz, W. Meyer, B. Reischl, S. Rutz, E. Schreiber, and L. Wöste.
Femtosecond study of multiphoton ionization processes in K_2 : From pump-probe to control.
J. Phys. Chem. **100**, 7789–7796 (1996).
- [146] S. Rutz, R. deVivieRiedle, and E. Schreiber.
Femtosecond wave-packet propagation in spin-orbit-coupled electronic states of $^{39,39}K_2$ and $^{39,41}K_2$.
Phys. Rev. A **54**, 306–313 (1996).
- [147] H. Schwoerer, R. Pausch, M. Heid, V. Engel, and W. Kiefer.
Femtosecond time-resolved two-photon ionization spectroscopy of K_2 .
J. Chem. Phys. **107**, 9749–9754 (1997).
- [148] H. Schwoerer, R. Pausch, M. Heid, and W. Kiefer.
Femtosecond vibrational wavepacket spectroscopy in the electronic ground state of K_2 .
Chem. Phys. Lett. **285**, 240–245 (1998).
- [149] R. Pausch, M. Heid, T. Chen, W. Kiefer, and H. Schwoerer.
Selective generation and control of excited vibrational wave packets in the electronic ground state of K_2 .
J. Chem. Phys. **110**, 9560–9567 (1999).
- [150] C. Nicole, M. A. Bouchene, C. Meier, S. Magnier, E. Schreiber, and B. Girard.
Competition of different ionization pathways in K_2 studied by ultrafast pump-probe spectroscopy: A comparison between theory and experiment.
J. Chem. Phys. **111**, 7857–7864 (1999).
- [151] U. Hefter, G. Ziegler, A. Mattheus, A. Fischer, and K. Bergmann.
Preparation And Detection Of Alignment With High (M) Selectivity By Saturated Laser Optical-Pumping In Molecular-Beams.
J. Chem. Phys. **85**, 286–302 (1986).

-
- [152] H. Hulsman and J. Korving.
Evolution of the Orientational and Internal-State Distribution of Molecules in An Expanding Jet.
J. Chem. Phys. **95**, 5719–5731 (1991).
- [153] V. Aquilanti, D. Ascenzi, M. D. Vitores, F. Pirani, and D. Cappelletti.
A quantum mechanical view of molecular alignment and cooling in seeded supersonic expansions.
J. Chem. Phys. **111**, 2620–2632 (1999).
- [154] T. Baumert, B. Buhler, R. Thalweiser, and G. Gerber.
Femtosecond spectroscopy of molecular autoionization and fragmentation.
Phys. Rev. Lett. **64**, 733–736 (1990).
- [155] T. Feurer, J. C. Vaughan, and K. A. Nelson.
Spatiotemporal coherent control of lattice vibrational waves.
Science **299**, 374–377 (2003).
- [156] S. P. Shah and S. A. Rice.
Controlling quantum wavepacket motion in reduced-dimensional spaces: reaction path analysis in optimal control of HCN isomerization.
Faraday Discussions pp. 319–331 (1999).
- [157] Y. Ohtsuki, K. Ohara, M. Abe, K. Nakagami, and Y. Fujimura.
New quantum control pathway for a coupled-potential system.
Chem. Phys. Lett. **369**, 525–533 (2003).
- [158] F. Grossmann, L. Feng, G. Schmidt, T. Kunert, and R. Schmidt.
Optimal control of a molecular cis-trans isomerization model.
Europhysics Letters **60**, 201–206 (2002).
- [159] H. Umeda, M. Takagi, S. Yamada, S. Koseki, and Y. Fujimura.
Quantum control of molecular chirality: Optical isomerization of difluorobenzo[c]phenanthrene.
J. Am. Chem. Soc. **124**, 9265–9271 (2002).
- [160] R. W. Schoenlein, L. A. Peteanu, R. A. Mathies, and C. V. Shank.
The 1st Step in Vision - Femtosecond Isomerization of Rhodopsin.
Science **254**, 412–415 (1991).
- [161] Q. Wang, R. W. Schoenlein, L. A. Peteanu, R. A. Mathies, and C. V. Shank.
Vibrationally Coherent Photochemistry in the Femtosecond Primary Event of Vision.
Science **266**, 422–424 (1994).
- [162] Y. H. Meyer, M. Pittman, and P. Plaza.
Transient absorption of symmetrical carbocyanines.
J. Photochem. Photobiol. A **114**, 1–21 (1998).

- [163] U. Åberg, E. Åkesson, J. L. Alvarez, I. Fedchenia, and V. Sundström.
Femtosecond Spectral Evolution Monitoring The Bond-Twisting Event In Barrierless Isomerization In Solution.
Chem. Phys. **183**, 269–288 (1994).
- [164] A. Sanchez-Galvez, P. Hunt, M. A. Robb, M. Olivucci, T. Vreven, and H. B. Schlegel.
Ultrafast radiationless deactivation of organic dyes: Evidence for a two-state two-mode pathway in polymethine cyanines.
J. Am. Chem. Soc. **122**, 2911–2924 (2000).
- [165] G. Vogt.
Kohärente Kontrolle chemischer Reaktionen in der flüssigen Phase.
Diplomarbeit, Universität Würzburg (2003).
- [166] N. Katayama, Y. Ozaki, S. Yasui, and K. Iriyama.
Spectroscopic studies of thiatrimethine, pentamethine and heptamethine cyanine dyes. 1. Structure of thiatrimethine, pentamethine and heptamethine cyanine dyes in solutions studied by NMR.
J. Mol. Struct. **274**, 171–181 (1992).
- [167] S. Ghelli and G. Ponterini.
Identification of the photoisomers of 2 carbocyanines by H-1 NMR spectroscopy.
J. Mol. Struct. **355**, 193–200 (1995).
- [168] K. Nakatsu, H. Yoshioka, and T. Aoki.
Crystal-Structure of 3,3'-Diethyl-Thiacyanine Bromide.
Chemistry Letters **5**, 339–& (1972).
- [169] V. Sundström and T. Gillbro.
Viscosity-dependent isomerization yields of some cyanine dyes - a picosecond laser spectroscopy study.
J. Phys. Chem. **86**, 1788–1794 (1982).
- [170] G. Krampert, G. Vogt, P. Niklaus, F. Santoro, and G. Gerber.
Photoisomerisation of NK88: Dynamics and Control.
in Preparation, (2004).
- [171] M. Bergt, T. Brixner, B. Kiefer, M. Strehle, and G. Gerber.
Controlling the femtochemistry of Fe(CO)₅.
J. Phys. Chem. A **103**, 10381–10387 (1999).
- [172] L. J. Butler, E. J. Hintsä, S. F. Shane, and Y. T. Lee.
The electronic state-selective photodissociation of CH₂BrI at 248, 210, and 193 nm.
J. Chem. Phys. **86**, 2051–2074 (1987).

-
- [173] D. G. Abrashkevich, M. Shapiro, and P. Brumer.
Coherent control of the $CH_2Br+I \leftarrow CH_2BrI \rightarrow CH_2I+Br$ branching photodissociation reaction.
J. Chem. Phys. **116**, 5584–5592 (2002).
- [174] W. B. Tzeng, Y. R. Lee, and S. M. Lin.
Photodissociation of CH_2BrCl at 248 and 193 nm Investigated by Translational Spectroscopy.
Chem. Phys. Lett. **227**, 467–471 (1994).
- [175] W. S. McGivern, R. J. Li, P. Zou, and S. W. North.
Photodissociation dynamics of CH_2BrCl studied using resonance enhanced multiphoton ionization (REMPI) with time-of-flight mass spectrometry.
J. Chem. Phys. **111**, 5771–5779 (1999).
- [176] S. H. Lee, Y. J. Jung, and K. H. Jung.
Photodissociation dynamics of CH_2BrCl at 234 nm.
Chem. Phys. **260**, 143–150 (2000).
- [177] G. Baum and J. R. Huber.
Photodissociation of CF_2BrCl at 193 nm Investigated by Photofragment Translational Spectroscopy.
Chem. Phys. Lett. **213**, 427–432 (1993).
- [178] A. Yokoyama, K. Yokoyama, and T. Takayanagi.
Photodissociation dynamics of $CBrClF_2$ at 157.6 nm. I. Experimental study using photofragment translational spectroscopy.
J. Chem. Phys. **114**, 1617–1623 (2001).
- [179] Y. J. Jung, M. S. Park, Y. S. Kim, K. H. Jung, and H. R. Volpp.
Photodissociation of $CBrCl_3$ at 234 and 265 nm: Evidence of the curve crossing.
J. Chem. Phys. **111**, 4005–4012 (1999).
- [180] Y. R. Lee, W. B. Tzeng, Y. J. Yang, Y. Y. Lin, and S. M. Lin.
Photodissociation of $CBrCl_3$ at 248 nm by Translational Spectroscopy.
Chem. Phys. Lett. **222**, 141–145 (1994).
- [181] Y. R. Lee, Y. J. Yang, Y. Y. Lin, and S. M. Lin.
Photodissociation of $CBrCl_3$ at 193 nm by Translational Spectroscopy.
J. Chem. Phys. **103**, 6966–6972 (1995).
- [182] T. Takayanagi and A. Yokoyama.
The Role of Nonadiabatic Coupling in Bond-Selective Dissociations - 2-Dimensional Model-Calculations.
Bulletin of the Chemical Society of Japan **68**, 2225–2232 (1995).
- [183] S. A. Rice and M. Zhao.
Optical Control of Molecular Dynamics, volume 403.
Wiley, New York (2000).

- [184] R. J. Gordon and S. A. Rice.
Active control of the dynamics of atoms and molecules.
Annu. Rev. Phys. Chem. **48**, 601–641 (1997).
- [185] H. Rabitz and W. S. Zhu.
Optimal control of molecular motion: Design, implementation, and inversion.
Acc. Chem. Res. **33**, 572–578 (2000).
- [186] M. Shapiro and P. Brumer.
Coherent control of atomic molecular, and electronic processes.
Advances in Atomic Molecular, and Optical Physics, Vol. 42 **42**, 287–345 (2000).
- [187] T. C. Weinacht, J. L. White, and P. H. Bucksbaum.
Toward strong field mode-selective chemistry.
J. Phys. Chem. A **103**, 10166–10168 (1999).
- [188] B. A. Mamyrin.
Laser assisted reflectron time-of-flight mass spectrometry.
Int. J. Mass Spectrom. Ion Processes **131**, 1–19 (1993).
- [189] B. Kiefer.
Femtosekunden-Experimente an $Fe(CO)_5$ in der Gasphase.
Diplomarbeit, Universität Würzburg (1997).
- [190] L. Bañares, T. Baumert, M. Bergt, B. Kiefer, and G. Gerber.
Femtosecond photodissociation dynamics of $Fe(CO)_5$ in the gas phase.
Chem. Phys. Lett. **267**, 141–148 (1997).
- [191] B. Kiefer.
Femtochemie: Beobachtung und Steuerung molekularer Dynamik.
Dissertation, Universität Würzburg (2000).
- [192] T. Brixner, B. Kiefer, and G. Gerber.
Problem complexity in femtosecond quantum control.
Chem. Phys. **267**, 241–246 (2001).
- [193] I. S. Averbukh, M. J. J. Vrakking, D. M. Villeneuve, and A. Stolow.
Wave packet isotope separation.
Phys. Rev. Lett. **77**, 3518–3521 (1996).
- [194] M. Leibscher and I. S. Averbukh.
Optimal control of wave-packet isotope separation.
Phys. Rev. A **6304**, art–043407 (2001).
- [195] A. Lindinger, C. Lupulescu, M. Plewicki, F. Vetter, A. Merli, S. M. Weber, and L. Woste.
Isotope selective ionization by optimal control using shaped femtosecond laser pulses.
Phys. Rev. Lett. **93**, art–033001 (2004).

-
- [196] T. Ibuki, A. Hiraya, and K. Shobatake.
Vacuum ultraviolet absorption spectra and photodissociative excitation of CHBr_2Cl and CHBrCl_2 .
J. Chem. Phys. **96**, 8793–8798 (1992).
- [197] S. Suzuki, K. Mitsuke, T. Imamura, and I. Koyano.
Negative-Ion Mass-Spectrometric Study of Ion-Pair Formation in the Vacuum Ultraviolet. IV. $\text{CH}_3\text{X} \rightarrow \text{X}^- + \text{CH}_3^+$ ($\text{X}=\text{F}, \text{Cl}, \text{Br}$).
J. Chem. Phys. **96**, 7500–7505 (1992).
- [198] K. Suto, Y. Sato, C. L. Reed, V. Skorokhodov, Y. Matsumi, and M. Kawasaki.
Ion fragment imaging of the ion-pair photodissociation of CH_3Cl , CH_3Br , $\text{C}_2\text{H}_5\text{Cl}$, and $\text{C}_2\text{H}_5\text{Br}$ at 118 nm.
J. Phys. Chem. A **101**, 1222–1226 (1997).

Acknowledgements

Last but not least, I would like to thank all those people, who have contributed to the successful finish of this work. Many of the results presented in this thesis have only been possible due to excellent team work. I would like to thank all members of “Experimentelle Physik I” for the very friendly atmosphere. It has been a pleasure working here, even at times when the laser system was acting up and the experiments seemed to go nowhere. Without the cooperation and support of many people this work would not have been possible. In particular I would like to thank the following people:

- Prof. Dr. Gustav Gerber for giving me the opportunity to work in this exciting research field, for the freedom to pursue own ideas and experiments, for the financial support that made all these experiments possible and for being always excited about new experimental results
- Prof. Dr. Thomas Baumert and Dr. Matthias Wollenhaupt for the opportunity to work on the potassium dimer experiment at the Universität Kassel and for their patience, when the experimental progress was slow
- Gerhard Vogt for his endurance and never ceasing motivation in the NK88 experiment
- Dr. Tobias Brixner for his competence in all questions of pulse shaping, especially polarization pulse shaping and for discussions on light polarization and many other topics in physics
- Reimer Selle for his imperturbability in “völlig unkritischen” situations at 3 in the morning during the potassium dimer experiment and for his input concerning the polarization–shaping at 400 nm
- Patrick Niklaus for his expertise with the laser system and the TOPAS optical parametrical amplifier in the here not shown MIR transient absorption experiment; and Patrick Niklaus again and Patrick Nürnberger for their support in the NK88 experiment
- Christian Horn, Dirk Liese, Oksana Graefe and the rest of the Kassel crew for their essential contributions to the success of the potassium dimer ex-

periment; and Christian Horn again for his illustrations of K_2 dynamics model

- Thomas Pfeifer, Frank Dimler and Alexander Paulus for their willingness to embark on mind-twisting discussions about physics, life, the universe and all the rest
- Christian Dietl and Vangelis Papastathopoulos from Labor B and the crew from Labor A for the unique working atmosphere.
- Dr. Niels Damrauer and Dr. Ullrich Weichmann for providing the standard solution to the problems of many long working days during the CH_2ClBr experiment
- All computer system administrators for their sisyphus like work against the forces of entropy and chaos in common Windows clients and servers. Special thanks go to Dominik Walter for his patience to listen to my complaints about not-working Windows installations and other nuisances in the life of a computer user.
- The reviewers of the earlier versions of this manuscript Patrick Nürnberger, Reimer Selle and Gerhard Vogt for their valuable suggestions how to improve it.
- All the rest of the members of “Experimentelle Physik I” and in particular the technical and administrative staff

Special thanks go to my family and to my friends. Without their support in all these years this work and my studying physics would not have been possible.

Curriculum Vitae

Persönliche Daten

Name: Gerhard Michael Krampert
Wohnort: Zwinger 16, 97070 Würzburg
geboren am: 05. Oktober 1976 in Erlangen
Staatsangehörigkeit: deutsch
Familienstand: ledig

Schulausbildung

09/1983 – 07/1987 Grundschole Bamberg
09/1987 – 06/1996 Clavius-Gymnasium Bamberg
28. Juni 1996 Allgemeine Hochschulreife

Studium der Physik

10/1996 – 08/1999 Bayerische Julius-Maximilians-Universität Würzburg
08/1999 – 08/2000 University of Texas at Austin (USA)
Master Thesis bei Prof. Dr. R.E. Martinez:
Nanoscale multi-photon spectroscopy using an apertureless NSOM
21. August 2000 Abschluss: Master of Arts
seit 12/2000 Bayerische Julius-Maximilians-Universität Würzburg
Promotion bei Prof. Dr. G. Gerber

Berufsweg

seit 02/2001 wissenschaftlicher Mitarbeiter der Universität Würzburg

Würzburg, den 16. August 2004

Gerhard Krampert